Spring 2014

Electro-deformation of a moving boundary: a drop interface and a lipid bilayer membrane

Herve Nganguia
New Jersey Institute of Technology

ABSTRACT

ELECTRO-DEFORMATION OF A MOVING BOUNDARY: A DROP INTERFACE AND A LIPID BILAYER MEMBRANE

by
Herve Nganguia

This dissertation focuses on the deformation of a viscous drop and a vesicle immersed in a (leaky) dielectric fluid under an electric field. A number of mathematical tools, both analytical and numerical, are developed for these investigations. The dissertation is divided into three parts. First, a large-deformation model is developed to capture the equilibrium deformation of a viscous spheroidal drop covered with non-diffusing insoluble surfactant under a uniform direct current (DC) electric field. The large-deformation model predicts the dependence of equilibrium spheroidal drop shape on the permittivity ratio, conductivity ratio, surfactant coverage, and the elasticity number. Results from the model are carefully compared against the small-deformation (quasispherical) analysis, experimental data and numerical simulation results in the literature. Moreover, surfactant effects, such as tip stretching and surface dilution effects, are greatly amplified at large surfactant coverage and high electric capillary number. These effects are well captured by the spheroidal model, but cannot be described in the second-order small-deformation theory.

The large-deformation spheroidal model is then extended to study the equilibrium deformation of a giant unilamellar vesicle (GUV) under an alternating current (AC) electric field. The vesicle membrane is modeled as a thin capacitive spheroidal shell and the equilibrium vesicle shape is computed from balancing the mechanical forces between the fluid, the membrane and the imposed electric field. Detailed comparison against both experiments and small-deformation theory shows that the spheroidal model gives better agreement with experiments in terms of the dependence on fluid conductivity ratio, electric field strength and frequency, and vesicle size. Asymptotic

analysis is conducted to compute the crossover frequency where a prolate vesicle crosses over to an oblate shape, and comparisons show the spheroidal model gives better agreement with experimental observations.

Finally, a numerical scheme based on immersed interface method for two-phase fluids is developed to simulate the time-dependent dynamics of an axisymmetric drop in an electric field. The second-order immersed interface method is applied to solving both the fluid velocity field and the electric field. To date this has not been done before in the literature. Detailed numerical studies on this new numerical scheme shows numerical convergence and good agreement with the large-deformation model. Dynamics of an axisymmetric viscous drop under an electric field is being simulated using this novel numerical code.

ELECTRO-DEFORMATION OF A MOVING BOUNDARY: A DROP INTERFACE AND A LIPID BILAYER MEMBRANE

by
Herve Nganguia

A Dissertation
Submitted to the Faculty of
New Jersey Institute of Technology and
Rutgers, The State University of New Jersey – Newark
in Partial Fulfillment of the Requirements for the Degree of
Doctor of Philosophy in Mathematical Sciences

Department of Mathematical Sciences
Department of Mathematics and Computer Science, Rutgers-Newark

May 2014

APPROVAL PAGE

ELECTRO-DEFORMATION OF A MOVING BOUNDARY: A DROP INTERFACE AND A LIPID BILAYER MEMBRANE

Herve Nganguia

Dr. Yuan-Nan Young, Dissertation Advisor — Date
Associate Professor of Mathematics, NJIT

Dr. Michael Booty, Committee Member — Date
Professor of Mathematics, NJIT

Dr. Amitabha Bose, Committee Member — Date
Professor of Mathematics, NJIT

Dr. Shidong Jiang, Committee Member — Date
Associate Professor of Mathematics, NJIT

Dr. Shravan Veerapaneni, Committee Member — Date
Assistant Professor of Mathematics, University of Michigan

BIOGRAPHICAL SKETCH

Author: Herve Nganguia

Degree: Doctor of Philosophy

Date: May 2014

Undergraduate and Graduate Education:

- Doctor of Philosophy in Mathematical Sciences,
  New Jersey Institute of Technology, Newark, NJ, 2014
- Master of Science in Applied Mathematics,
  San Diego State University, San Diego, CA, 2008
- Master of Science in Biomedical Engineering,
  Columbia University, New York, NY, 2005
- Bachelor of Science in Engineering Sciences,
  CUNY College of Staten Island, Staten Island, NY, 2003

Major: Mathematical Sciences

Presentations and Publications:

H. Nganguia and Y.-N. Young. Equilibrium electrodeformation of a spheroidal vesicle in an AC electric field. *Phys. Rev. E*, 88:052718, 2013.

H. Nganguia, Y.-N. Young, P. M. Vlahovska, J. Blawzdziewcz, J. Zhang and H. Lin. Equilibrium electro-deformation of a surfactant-laden viscous drop. *Phys. Fluids*, 25:092106, 2013.

B. Sundaram, A. C. Poje, R. R. Veit and H. Nganguia. Acoustical dead zones and the spatial aggregation of whale strandings. *J. Theor. Biol.*, 238:764-770, 2006.

I came to accept that I have no right whatsoever to judge others in terms of my own customs.

Nelson Mandela

ACKNOWLEDGMENT

It is my utmost pleasure to take this time, and thank those people without whom this Dissertation would not have been possible.

First and foremost, I would like to express my most sincere gratitude to my advisor, Dr. Yuan-Nan Young, for his patience, his guidance, and his honesty through this journey. I thank him for his time, and for being a true inspiration.

Throughout my time at NJIT, I have been privileged to take courses taught by professors whose words of encouragement and advices have served me well. To Dr. John Bechtold, Dr. Michael Booty, Dr. Linda Cummings, Dr. Shidong Jiang, Dr. Horacio Rotstein, Dr. Robert Miura and Dr. Michael Siegel, I express my deepest appreciation.

A great deal of the content of this work has been enriched thanks to discussions and collaborations with faculties outside of the NJIT community. I especially would like to thank Dr. Anita Layton of Duke Univeristy, Dr. Shravan Veerapaneni of the Univeristy of Michigan, and Dr. Petia Vlahovska of Brown University.

I want to thank my colleagues, Sonia Bandha, Lenka Kovalcinova, Manman Ma, and Jeffrey Pohlmeyer, for engaging and substantial conversations on just about everything; your awareness and openness were refreshing, and a much-needed break from our demanding studies.

Last, but far from least, I want to recognize the ever constant support of my parents, my siblings, my family, and my friends. To them I dedicate this work as a small token of gratitude for the joy they continue to bring me.

TABLE OF CONTENTS

TABLE OF CONTENTS
(Continued)

Chapter **Page**

TABLE OF CONTENTS
(Continued)

Chapter **Page**

LIST OF TABLES

Table **Page**

LIST OF FIGURES

Figure **Page**

LIST OF FIGURES
(Continued)

Figure **Page**

LIST OF FIGURES
(Continued)

Figure **Page**

LIST OF FIGURES
(Continued)

Figure **Page**

CHAPTER 1

INTRODUCTION

The motivation for this work was to develop a better understanding of the process by which pores form on lipid bilayer membrane. Membrane pores are openings on vesicles membrane caused by subjecting vesicles to an external force. This external force can be the result of various stimuli such as osmosis [111, 145], surfactants and lipids [69, 129], illumination [131], sound field [93].

Ohno *et al.* [111] conducted experiments in which pores were formed on liposomes obtained from water-in-oil phospholipid-coated micro droplets (W/O droplets). The solutions inside and outside the liposomes have different osmolarities. The difference in concentration creates an osmotic flow of small particles across the membrane and into the liposomes. As a result, the volume inside the liposomes expands, stretching the lipid membrane, and ultimately leading to membrane ruptures. Once the pore is opened, it was observed the liposomes responded in one of three different ways: They broke completely and finally disappeared, they transformed and/or shrunk, or the hole resealed and they returned to their initial spherical shape (Figure 1.1).

Figure 1.2 shows results of an experiment conducted by Sadik *et al.* [127]. In Figure 1.2(a), a 70μL solution containing a 28.8μm vesicle (closed lipid bilayer membrane) is placed in a chamber consisting of two electrodes. An electric field of strength $E = 1.5$ kV/cm is then applied, bringing the vesicle to deform into a prolate spheroid. Note that the vesicle membrane may have local irregularities causing deviations from ellipsoidal shapes, so the fitted prolate spheroid in Figure 1.2(b) is an estimate. When the vesicle transmembrane potential exceeds a certain threshold (of the order of 1 V), the membrane ruptures and pores are formed at the polar caps, as shown in Figure 1.2(b). When the electric field is turned off, the vesicle relaxes back to its original, spherical shape. Note the appreciable reduction in vesicle size

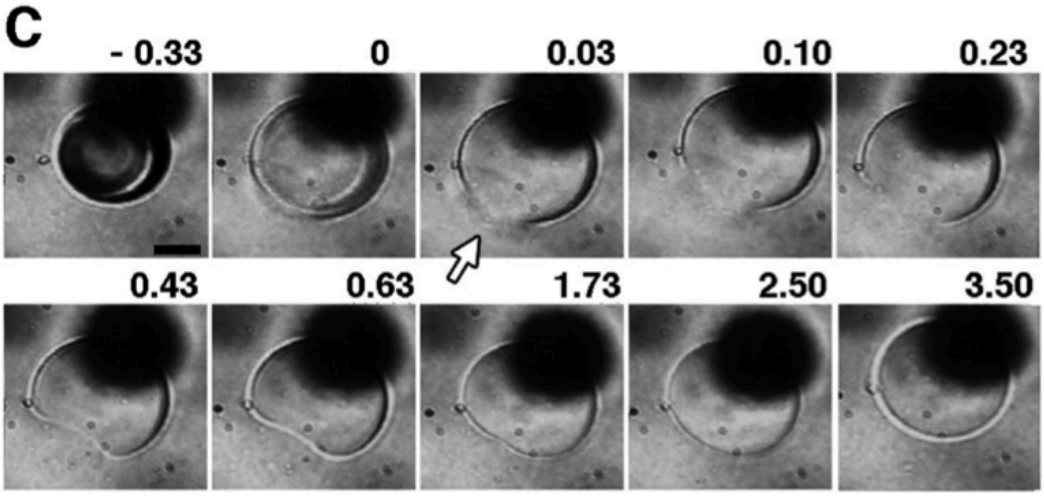

Figure 1.1 Time-lapse images of liposomes showing large membrane ruptures (shown by arrows) in response to different osmolarities. The vesicle shows a resealing of the membrane after opening a hole.

in Figure 1.2(c): The vesicle shrank, pointing to an efflux of interior fluids. This is further evidence that pores did in fact form as described earlier.

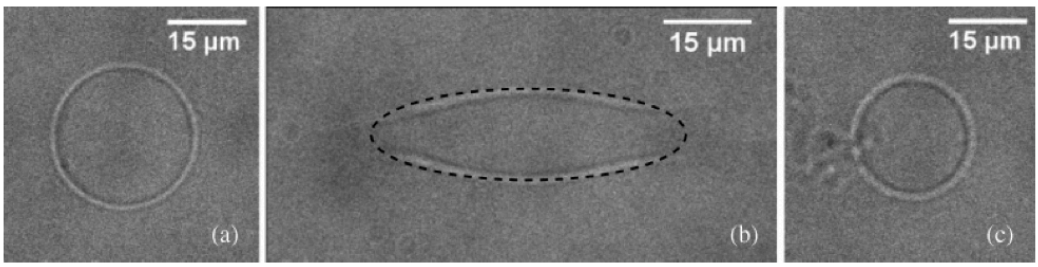

Figure 1.2 Images of a vesicle (a) before, (b) during, and (c) after the application of an electric pulse. The vesicle was originally $r_0 = 28.8\mu$m in diameter. The applied field was $E = 1.5$ kV/cm and pointing from right to left. The shape of the vesicle during application of the electric field is fitted with an ellipse (black dashed line) (b). The vesicle demonstrates a large prolate deformation with an aspect ratio $\frac{a}{b} = 3.57$. The postpulsation image (c) shows an appreciable reduction in vesicle size.

While the dynamics of a membrane pore has been investigated extensively [19, 71, 72, 131], the process leading to pore formation is poorly understood. This work aims to improve scientific knowledge by introducing tools that could help better understand the underlying dynamics leading to electrically-induced pore formation.

This in turn has the potential to significantly improve the effective use of vesicles in a wide range of biomedical and biotechnological applications such as cancer treatment, wound healing, and gene therapy [46, 47, 48, 57], just to name a few. Moreover, the application of an electric field to a deformable interface immersed in a fluid has great relevance in many other industrial [7, 53, 70, 90, 100, 166, 167] and biological processes [18, 63, 84, 105, 160, 161, 173].

In electrohydrodynamics (EHD), a flow is induced due to the electrostatic force resulting from variations between the electric properties of the bulk (or exterior) fluid and the fluid enclosed by the interface (or interior fluid). The interplay between viscous force form the induced flow and the electric force leads to changes in the shape of the interface.

Electrokinetic effects on the deformation of an interface become important when electrolytes are present in the bulk fluid. In this dissertation, the interior and exterior fluids are considered to be leaky dielectrics: Weakly conducting substances that support electrostatic fields. Here, the theory is based on the *leaky dielectric* model of Taylor [101, 132, 147]. In this model, the bulk is assumed to be electroneutral, while a surface charge density develops at the interface where there is a jump in material electric properties. The electrostatic and flow fields can be solved independently of each other because the coupling between these two fields only occurs at the fluid interface, through the Maxwell stress. Moreover, theoretical results focus on equilibrium deformations, and the transient dynamics are ignored. Two types of moving boundary are investigated: (1) The deformation of a surfactant-covered viscous drop in a DC electric field, and (2) the deformation of a vesicle in an AC electric field.

1.1 Surfactant-covered Viscous Drop in a DC Electric Field

Upon application of an electric field to a weakly conducting (leaky dielectric) drop suspended in another leaky dielectric fluid, free charges accumulate at the interface between the two fluids while the bulk remains electrically neutral [101, 147]. Studies show that a viscous drop can deform into a prolate (oblate) ellipsoid with the long axis aligned parallel (perpendicular) to the direction of the imposed electric field [2, 101, 132]. The flow circulation around the prolate drop is often opposite to that around the oblate drop, depending on the mismatch in electric conductivity, permittivity, and viscosity between the interior and exterior fluids. A brief and clear review of the droplet electrohydrodynamics can be found in Ref. [77].

Taylor's spherical model [147] explains how different combinations of viscosity, permittivity, and conductivity lead to either prolate or oblate shapes. For small to moderate electric field strengths, the balance between the surface tension, electric, and hydrodynamic stresses results in an equilibrium drop shape [54, 142, 171]. Small-deformation analysis provides good agreement with experiments for a slightly deformed viscous drop under a weak DC electric field [1, 147]. When applied to large drop deformations under a strong electric field, however, small-deformation theories give no quantitative agreement with experiments.

Recently, Bentenitis and Krause [10] extended the leaky dielectric model for large electro-deformation of a non-charged viscous drop in a leaky dielectric fluid. Their large deformation analysis assumes spheroidal shapes and gives good agreement with most experiments for the prolate drops. Zhang *et al.* [169] refined the spheroidal model by projecting the stress balances onto the corresponding (unsteady) velocity components, which is also done in the variational analysis [22] and reduced model analyses [37, 137]. They obtained good agreement with experiments on prolate drops, but provided no comparison for the oblate drops in Ref. [169].

Under an even stronger electric field (beyond the critical strength), no steady equilibrium drop shape can be found and the drop keeps elongating until the eventual break-up into smaller droplets [24, 25, 55]. Conical points may form at the end of the viscous drop at high capillary number [77], and small droplets may detach from the tip as a result of the tip-streaming instability [146]. The drop may also undergo undulation and break into several droplets of comparable sizes. The large deformation models in [10, 169] are inadequate to capture such extreme deformation, and numerical simulations have been conducted to investigate large electro-deformation using the leaky dielectric model [8, 16, 17, 77, 102, 142, 143, 172].

Tip-streaming has also been observed for a surfactant-covered drop in extensional flow [4, 15, 30]. Surfactants (surface-active agents) are often used to facilitate breakup and deformation of fluid interface in many engineering applications [4, 26, 67, 110], and they are known to affect the stability of a viscous drop through a combination of reduced surface tension and the immobilizing (surface stiffening) effect of the Marangoni stress [3, 50, 67, 103, 140, 144, 162].

The electro-deformation of a surfactant-laden viscous drop has been investigated by Ha and Yang [51, 52] (experiments and small-deformation analysis) and later by Teigen and Munkejord [148] (axisymmetric numerical simulations). While Ha and Yang [51, 52] concluded that surfactant enhances deformation for a prolate drop, Teigen and Munkejord [148] found that smaller deformation may be caused by diffusing surfactant for a prolate drop with a circulation from the pole to the equator (prolate B as categorized by Lac and Homsy [77]).

1.2 Vesicle in an AC Electric Field

The electro-deformation and electro-dynamics of vesicles (closed pure lipid bilayer membranes) have been a paradigm for understanding how a biological cell behaves under an electric field. Vesicles are known to change their shape depending on the

frequency of the imposed alternating current (AC) electric fields and the mismatch in fluid conductivities [6, 36, 123, 124]. Changes in vesicle orientation, dielectrophoresis and electrorotation have also been observed. Under DC electric fields, both vesicles and biological cells tend to undergo large deformations with aspect ratios reaching ten. The permeabilization of vesicles membranes using electric fields has also generated a lot of practical and modeling interest, especially in the biotechnology industry. Electroporation, the process of perforating the membrane by applying an (often DC) electric field, has been proposed as a method for delivering molecules into living organisms [23, 75, 106, 107, 138, 141, 149, 120, 174]. Most recently, electroporation has been used for measurements of various properties of the cell membranes [120, 130].

The earliest theories of vesicle electro-deformation were based on minimizing the total energy consisting of the membrane energy (tension and bending) and electrical energy (Maxwell stresses) [56, 163]. These models focus on conductivity ratio ≈ 1, and as a result the models were only able to predict prolate shape. Extension of these models allow for large conductivity mismatch [116, 164] and are thus able to predict the various shapes observed experimentally [6], even though poor quantitative agreement with the experiments is found. Hyuga *et al.*[64, 65] proposed the first theory (to the author's knowledge) beyond the minimum energy approach. Sadik *et al.* [128] modified this approach to model the deformation of spheroidal vesicles under strong electric fields.

Vlahovska *et al.* [157] proposed a perturbative method to study the dynamics and deformation of a nearly-spherical vesicle subject to weak AC electric fields. Assuming small asphericity, they used the transmembrane potential for a dielectric spherical shell in AC fields in the analyses. The small-deformation results are in qualitative agreement with experiments in terms of shape elongation and the transition frequency between prolate and oblate vesicle. Yet the small-deformation theory does not apply to vesicles subjected to moderate and strong electric fields, where

deformations are well beyond the nearly spherical shape [123]. Zhang *et al.* [170] proposed a spheroidal model to study the transient dynamics of highly deformed vesicles under strong DC electric fields. Assuming that vesicles remain spheroidal under a slowly varying DC electric field, which is well supported by experimental findings in [76, 123, 128], their spheroidal results are in quantitative agreement with experimental data [170] in terms of the vesicle aspect ratio and its response to an electric pulse.

1.3 The Immersed Interface Method (IIM) for Electrodeformation of a Viscous Drop

A numerical code based on the immersed interface method (IIM) is developed to simulate the time-dependent dynamics of a viscous drop. The IIM is a fixed Cartesian grid method for solving equations whose solutions are discontinuous across an interface. The discontinuity can be due to a singular force on the interface or discontinuous coefficients. The main idea is to incorporate the jumps in the solution or its derivatives into the finite difference scheme, leading to a modified finite difference scheme that is second-order accurate at all points on the grid. The method was first developed by Leveque and Li [82], and applied to elliptic equations. It has since been extended to a wide-range of applications. For a somewhat comprehensive review, see the book by Li and Ito [89]. Note that the original motivation in developing the IIM was to obtain a second-order accurate version of Peskin's immersed boundary method (IBM) [114].

The IBM is a very robust algorithm for solving the incompressible Navier-Stokes equations with moving boundaries. Originally developed for the problem of blood flow in a beating heart [114, 115], it has since been extended to several other problems [12, 40, 151], including for the simulation of a viscous drop under a DC electric field and in shear flow [61]. In the IBM, the singular forcing term at the boundary is approximated by a set of discrete delta functions that spread the force from the boundary to the

Cartesian grid points. However, this approach appears to limit the accuracy of the IBM to first-order in solving the Navier-Stokes equations.

For a two-phase fluid problem with a moving boundary under an electric field, two separate sets of equations need to be solved: One for the electric potential, and the other for the fluid velocity. In most previous numerical studies hybrid methods were developed: The IIM only applied to solving the electric potential, and the fluid velocity is computed using methods that are generally first-order accurate [61, 112]. To the author's knowledge, the present numerical code is the first using the IIM to solve for both the electric potential and the fluid velocity in three-dimensional axial symmetric cylindrical coordinates.

This dissertation is organized as follows. In Chapter 2, the electrohdrodynamic equations are introduced in the leaky dielectric framework, and the general approach to obtaining analytical solutions of the equations is presented. The effects of different types of electric field are then investigated: Chapter 3 presents results of a surfactant-covered viscous drop under a DC electric field, while the morphological changes of a vesicle membrane under an AC electric field are presented in Chapter 4. In Chapter 5, a novel numerical code is presented to simulate the deformation of a surfactant-free viscous drop under DC electric field. All the results are summarized in Chapter 6, while extensions and future direction are discussed in Chapter 7.

CHAPTER 2

MATHEMATICAL FORMULATION

Electrohydrodynamics is concerned with the interaction between electric and flow fields, both of which are coupled at a fluid interface through the Maxwell stress tensor. In this chapter, the general equations of electrohydrodynamics are presented for an interface in an electric field (see Figure 2.1).

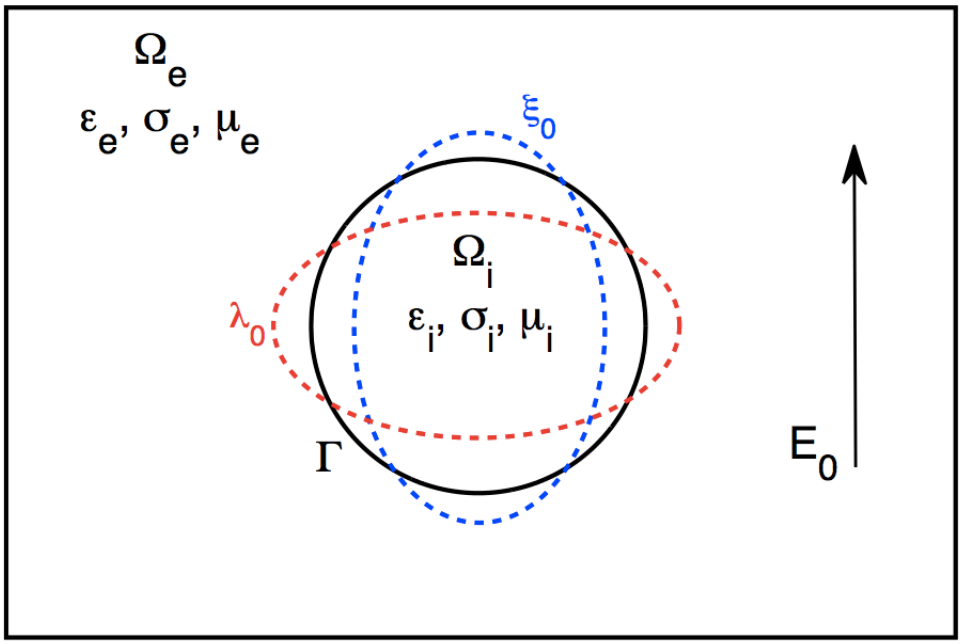

Figure 2.1 Sketch of the physical problem. The interface (Γ) separates the domain into two regions: The interior (i) and exterior (e). The regions have distinct material properties: Permittivity (ε), conductivity (σ), and viscosity (μ). In the presence of an electric field E_0, oriented along the axis of symmetry, the interface deforms into a prolate (ξ_0) or an oblate (λ_0) shape.

The fluid properties are piecewise constant on either side of the interface. Moreover, the leaky dielectric model [101, 132] is used, in which bulk charges neutralize instantly and the electromechanical coupling occurs only at the interface where induced charge, resulting form the sharp change in material properties, produces electric stresses. These considerations make the problem more amenable to analytical studies.

2.1 Governing Equations

Noting that the electrostatic field is solenoidal,

$$\nabla \times \boldsymbol{E} = 0, \tag{2.1}$$

the electric field can be expressed in terms of the electric potential, $\boldsymbol{E} = -\nabla\phi$. Moreover, the electric field $\boldsymbol{E}$ obeys Gauss's law

$$\nabla \cdot (\varepsilon \boldsymbol{E}) = \rho_e. \tag{2.2}$$

where ε and ρ_e are the permittivity and free charge density, respectively. Boundary conditions at the interface are obtained by integrating (2.2) across the interface, using the divergence theorem. The result shows that the normal component of $\boldsymbol{E}$ has a jump equal to the surface charge density q_s,

$$q_s = [\![\varepsilon \boldsymbol{E}]\!] \cdot \boldsymbol{n}, \tag{2.3}$$

$[\![f]\!] \equiv f_e - f_i$ denotes the difference between exterior and interior, $\boldsymbol{b}$ is the outward normal vector.

In the absence of a diffusive current (see [21, 121] and references therein), ρ_e is further related to the current, $\mathbf{i}$, by the charge conservation equation,

$$\frac{\partial \rho_e}{\partial t} + \nabla \cdot \mathbf{i} = \frac{\partial \rho_e}{\partial t} + \nabla \cdot (\rho_e \boldsymbol{u} + \sigma \mathbf{E}) = 0, \tag{2.4}$$

where σ is conductivity and $\boldsymbol{u}$ is the fluid velocity. Integrating (2.4) across the interface gives the boundary condition,

$$\frac{\partial q_s}{\partial t} + \nabla_s \cdot (q_s \boldsymbol{u}) = -\boldsymbol{n} \cdot [\![\sigma \boldsymbol{E}]\!] \tag{2.5}$$

In general, variations in the conductivity σ can be important when electrolytes are present in the bulk fluid. Here σ is assumed piecewise constant on either side of

the interface, and the bulk has no net charge density so that $\rho_e = 0$. In the leaky dielectric framework the electric potential problem satisfies

$$\nabla \cdot (\varepsilon \nabla \phi) = 0. \tag{2.6}$$

The flow is governed by the Navier-Stokes equations, which are non-linear. However, considering the size of the immersed boundary and the high viscosity nature of the leaky dielectric fluids, inertial terms can be ignored and the flow field reduces to the incompressible Stokes equation: The governing equations for the leaky dielectric model are

$$-\nabla p + \mu \nabla^2 \boldsymbol{u} + \boldsymbol{F} = 0, \tag{2.7}$$

$$\nabla \cdot \boldsymbol{u} = 0, \tag{2.8}$$

where p, ρ and μ are the the pressure, the density and the viscosity of the fluid, respectively. The sharp change in material electric properties at the interface generates a singular force

$$\boldsymbol{F}(\boldsymbol{x}, t) = \int_\Gamma \boldsymbol{f}(s, t) \delta(\boldsymbol{x} - \boldsymbol{X}(s, t)) ds, \tag{2.9}$$

where $\boldsymbol{X}(s, t)$ is the location of the interface, s is the arc-length, $\boldsymbol{x}$ is spatial position, $\boldsymbol{f}(s, t)$ is the force strength, and $\delta(\boldsymbol{x})$ is the Dirac delta function. With the exception of the empirical no-slip boundary condition, jump conditions for the fluid velocity can be obtained as was done for the electric problem, by integrating the governing

equations across the interface [132]. The boundary conditions at the interface become

$$[\![\phi]\!] = 0, \tag{2.10}$$

$$\boldsymbol{n} \cdot [\![\varepsilon \boldsymbol{E}]\!] = q_s, \tag{2.11}$$

$$\frac{\partial q_s}{\partial t} + \nabla_s \cdot (q_s \boldsymbol{u}) = -\boldsymbol{n} \cdot [\![\sigma \boldsymbol{E}]\!], \tag{2.12}$$

$$[\![\boldsymbol{u}]\!] = 0, \tag{2.13}$$

$$\frac{d\boldsymbol{X}}{dt} = (\boldsymbol{u} \cdot \boldsymbol{n})\boldsymbol{n}, \tag{2.14}$$

$$[\![(\mathbf{T} + \mathbf{S}) \cdot \boldsymbol{n}]\!] = \boldsymbol{f} \cdot \boldsymbol{n}, \tag{2.15}$$

where s denotes surface quantities, q_s is the surface charge density, and $\nabla_s = (\mathbf{I} - \boldsymbol{nn}) \cdot \nabla$ is the surface gradient operator, with $\mathbf{I}$ the identity tensor. The viscous (hydrodynamic) and Maxwell (electric) stress tensors are

$$\mathbf{T} = -p\mathbf{I} + \mu \left((\nabla \boldsymbol{u})^T + \nabla \boldsymbol{u} \right),$$

and

$$\mathbf{S} = \varepsilon \boldsymbol{E}\boldsymbol{E} - \frac{\varepsilon}{2} (\boldsymbol{E} \cdot \boldsymbol{E}) \mathbf{I},$$

respectively.

2.2 General Solutions in Spheroidal Coordinates

Assuming that the problem is three-dimensional axisymmetric, analytical solutions are derived using the spheroidal coordinates (χ, η) that are related to the cylindrical coordinates (r, z) as

$$z = c\chi\eta, \qquad r = \sqrt{(\chi^2 \pm 1)(1 - \eta^2)}, \tag{2.16}$$

where $\chi = \xi$ for prolate spheroids and $\chi = \lambda$ for oblate spheroids, and $c = \sqrt{a^2 - b^2}$ is the semi-focal length. Spheroids are obtained from surfaces of constant χ, while

hyperboloids are given by surfaces of constant $\eta \in [-1, 1]$. For prolate spheroids, $\xi \in [1, \infty)$, while $\lambda \in [0, \infty)$ for oblate spheroids.

Note that the oblate spheroidal coordinates can be obtained from the the prolate spheroidal coordinates by substituting $\xi \to \mathbf{i}\lambda,\ c \to -\mathbf{i}\bar{c}$, with $\mathbf{i} = \sqrt{-1}$. In the following derivations, the prolate spheroidal coordinates are used to outline the steps leading to the analytical solutions. Detailed derivations for the case of an oblate-deforming viscous drop in DC electric field are presented in Appendix C.

The electrostatic force generated by the electric field is computed from the electrostatic problem with piecewise homogeneous electric properties. Because no net charges exist in the bulk, the electric potential in each subdomain satisfies Laplace's equation,

$$\nabla \cdot (\varepsilon_j \nabla \phi) = 0, \tag{2.17}$$

with appropriate boundary conditions. ε_j is the permittivity of the fluid j, and $j = i,\ e$ denotes the fluid inside and outside the interface, respectively. Since the conductivity is constant on either side of the interface, (2.17) reduces to $\nabla^2 \phi = 0$ in each subdomain. In the spheroidal coordinates, the Laplacian operator

$$\Delta = \frac{1}{c^2(\xi^2 - \eta^2)} \left\{ \frac{\partial}{\partial \xi} \left[(\xi^2 - 1) \frac{\partial}{\partial \xi} \right] + \frac{\partial}{\partial \eta} \left[(1 - \eta^2) \frac{\partial}{\partial \eta} \right] \right\}. \tag{2.18}$$

Equation (2.17) is separable, and the general solution of the potential, ϕ is given by the truncated form

$$\phi_j = (\alpha_j \xi + \beta_j Q_1(\xi))\, \eta, \quad j = i, e, \tag{2.19}$$

where $Q_1(\xi)$ is the Legendre polynomial of the second kind. The coefficients $\alpha_j,\ \beta_j$ are obtained from boundary and interface conditions. Boundary conditions in the far-field and inside the interface immediately yield $\alpha_e = -c$ and $\beta_i = 0$. The electric

potential inside and outside are

$$\phi_e = (-cE_0\xi + \alpha Q_1(\xi))\eta, \tag{2.20}$$

$$\phi_i = \beta\xi\eta. \tag{2.21}$$

The remaining coefficients, $\alpha,\ \beta$ are determined from interface conditions, and depend on the model for the surface and on the type of electric field (DC or AC). More generally,

$$[\![-\nabla\phi\cdot\boldsymbol{t}]\!] = w, \qquad [\![\sigma\nabla\phi\cdot\boldsymbol{n}]\!] = v, \tag{2.22}$$

where $w = 0$ for a drop interface (Chapter 3), and w is equal to the transmembrane potential for a lipid bilayer membrane (Chapter 4). The surface function $v = \frac{dq_s}{dt}$.

The incompressible Stokes equations governing the flow,

$$\nabla p_j = \mu\nabla^2\boldsymbol{u}_j, \tag{2.23}$$

$$\nabla\cdot\boldsymbol{u}_j = 0, \tag{2.24}$$

where the singular force $\boldsymbol{F}(s,t)$ in (2.7) is absorbed into the stress balance at the interface. Because the problem is axisymmetric, one can solve for the stream function, ψ instead

$$(\mathbf{E}^2)^2\psi = 0, \tag{2.25}$$

where

$$\mathbf{E}^2 = \frac{1}{c^2(\xi^2-\eta^2)}\left[(\xi^2-1)\frac{\partial^2}{\partial\xi^2} + (1-\eta^2)\frac{\partial^2}{\partial\eta^2}\right]. \tag{2.26}$$

In terms of the stream function, the velocity field is given by: $u_j = -\frac{1}{h_\xi h_\zeta}\frac{\partial\psi_j}{\partial\xi}$ and $v_j = \frac{1}{h_\eta h_\zeta}\frac{\partial\psi_j}{\partial\eta}$, where u and v are the components of velocity in the tangential (η) and normal (ξ) directions, respectively. $h_\xi = c\sqrt{\frac{\xi^2-\eta^2}{\xi^2-1}}$, $h_\xi = c\sqrt{\frac{\xi^2-\eta^2}{1-\eta^2}}$, and $h_\zeta = c\sqrt{(\xi^2-1)(1-\eta^2)}$, are scale factors in the prolate spheroidal coordinates.

The general solution of (2.25) can be calculated by the semi decomposition method [28], in which the stream function is expressed as an infinite sum of products of Gegenbauer functions. The products are constructed from the eigenfunctions and generalized eigenfunctions of the operator $\mathbf{E}^2$. Omitting the detailed derivations, the eigenfunctions, $\Theta_n^{(i)}$,

$$\Theta^{(1)} = G_n(\xi)G_n(\eta), \tag{2.27}$$

$$\Theta^{(2)} = G_n(\xi)H_n(\eta), \tag{2.28}$$

$$\Theta^{(3)} = H_n(\xi)G_n(\eta), \tag{2.29}$$

$$\Theta^{(4)} = H_n(\xi)H_n(\eta), \tag{2.30}$$

$$\tag{2.31}$$

where G_n are the Gegenbauer functions of the first kind, and H_n are the Gegenbauer functions of the second kind. The generalized eigenfunctions, $\Omega_n^{(i)}$ are given in [28] or Appendix A. Then, the stream function ψ can be represented as

$$\psi(\xi,\eta) = \sum_{n=0}^{\infty}\sum_{i=1}^{4}\left[A_n^i\Theta_n^{(i)}(\xi,\eta) + B_n^i\Omega_n^{(i)}(\xi,\eta)\right], \tag{2.32}$$

where A_n^i and B_n^i are coefficients to be determined from boundary conditions. With the expressions for $\Theta_n^{(i)}(\xi,\eta)$ and $\Omega_n^{(i)}(\xi,\eta)$, and rearranging the terms in (2.32), ψ can be written in the semi-separable form

$$\psi(\xi,\eta) = g_0(\xi)G_0(\eta) + g_1(\xi)G_1(\eta) + \sum_{n=2}^{\infty}\left[g_n(\xi)G_n(\eta) + h_n(\xi)H_n(\eta)\right], \tag{2.33}$$

where g_n and h_n are linear combinations of the Gegenbauer functions. For more details on the method, interested readers are referred to [27, 28]. Note however that on the axis of symmetry, $G_n(\eta)$ are regular, while $H_n(\eta)$ are singular. Furthermore, $G_n(\xi)$ are regular in the interior of the spheroid, and $H_n(\xi)$ are regular every where else, except on the segment $\xi = 1$.

Applying the far-field boundary condition, $\boldsymbol{u} = 0$ as $\xi \to \infty$, and considering that the flow remains finite at the center line $\xi = 1$, the stream function simplifies to

$$\psi_e = \sum_{n=1}^{\infty} \left[A_{2n+1}^{2n-1} H_{2n-1}(\xi) + A_{2n+1}^{2n+1} H_{2n+1}(\xi) + A_{2n+1}^{2n+3} H_{2n+3}(\xi) \right] G_{2n+1}(\eta), \tag{2.34}$$

$$\psi_i = \sum_{n=1}^{\infty} \left[B_{2n+1}^{2n-1} G_{2n-1}(\xi) + B_{2n+1}^{2n+1} G_{2n+1}(\xi) + B_{2n+1}^{2n+3} G_{2n+3}(\xi) \right] G_{2n+1}(\eta). \tag{2.35}$$

In general, the full solution is obtained from the entire infinite series. Here, the stream functions are truncated at $n = 1$, and

$$\psi_e = \left[A_3^1 H_1(\xi) + A_3^3 H_3(\xi) \right] G_3(\eta), \tag{2.36}$$

$$\psi_i = \left[B_3^3 G_3(\xi) + B_3^5 G_5(\xi) \right] G_3(\eta). \tag{2.37}$$

The choice of truncating the solution at the first mode $n = 1$ is based on the assumption that boundary shapes are spheroid. Moreover, the speed of a point (ξ, η, c) on the boundary is given by

$$v(\xi_0) = \frac{d\boldsymbol{x}}{dt} \cdot \boldsymbol{e}_\xi = \frac{r_0 (1 - \xi^{-2})^{-5/6} (1 - 3\eta^2)}{3\xi^2 \sqrt{\xi^2 - \eta^2}} \frac{d\xi}{dt}, \tag{2.38}$$

where r_0 is the initial radius of the interface. Because $G_3(\eta) = \frac{1}{2}(\eta - \eta^3)$ and $G_3'(\eta) = \frac{1}{2}(1 - 3\eta^2)$, it becomes clear that $v(\xi_0) \propto G_3'(\eta)/\sqrt{\xi^2 - \eta^2}$. This further suggests that truncating the solution at the first mode provides a good approximation for the stream function.

The coefficients A_3^1, A_3^3, B_3^3 and B_3^5 are obtained using the continuity of velocities, the kinematic condition, and stress balances at the interface. In addition to these coefficients, the rate of change of the interface shape, $d\xi_0(t)/dt$ is also obtained as part of the solution. The exact form of $d\xi_0(t)/dt$ depends on the structure of the interface (drop or vesicle), and the type of electric field (DC or AC).

CHAPTER 3

ELECTRO-DEFORMATION OF A SURFACTANT-LADEN DROP

3.1 Introduction

Two different modes of drop breakup are observed in Ha and Yang's experiments [52] depending on the surfactant coverage. When the interface is clean or contaminated by a very small amount of surfactant, the drop bursts into several small droplets after forming bulbous ends. For a range of small surfactant concentration, tip-streaming is a prevalent drop breakup mode. If the surfactant concentration exceeds this range, the breakup mode goes back to fragmentation with bulbous end formation. This indicates that, although not pronounced in the small-deformation limit, non- uniformity of the surfactant concentration is a decisive factor for the breakup mechanism of a prolate viscous drop in a DC field.

It is not clear how the two drop breakup modes are related to surfactant effects. To investigate the origin of the two modes of breakup, the work in this chapter attempts to capture the large deformation of the surfactant-laden drop prior to breakup. In addition, a quantitative description of surfactant transport/ redistribution is essential to accurately elucidate surfactant effects. For example, how does surfactant alter the stability of an equilibrium drop shape? How does surfactant coverage affect the equilibrium drop deformation? How important is the Marangoni stress at different values of the electric capillary number?

To answer these questions, the electro-deformation of a surfactant-laden viscous drop is studied in the leaky dielectric EHD framework. The approaches in [170] are extended to include the surfactant effects, and the focus is put on how insoluble surfactant affects the existence of a spheroidal drop and its deformation at equilibrium. Furthermore, quantification of surfactant effects on a viscous drop in a DC electric field is sought.

This chapter is organized as follows. The problem is formulated in the leaky dielectric framework, and the governing equations are derived in Section 3.2. In Section 3.3 the validation of the spheroidal model without surfactant is presented. The results are summarized in Section 3.4: First the dependence of the existence of an equilibrium spheroidal drop on various parameters is examined in Section 3.4.1. Comparison against experiments and numerical simulations of surfactant-covered drops are presented in Section 3.4.2, where the similarity and difference between prolate and oblate surfactant-covered drops in a DC electric field are discussed further. In Section 3.4.3 the surfactant effects in terms of surface dilution and tip stretching are examined using the average surface tension. Finally, findings are summarized in Section 3.5.

3.2 Problem Formulation

Consider a viscous leaky dielectric drop immersed in another leaky dielectric fluid as shown in Figure 3.1. Each fluid is characterized by its viscosity μ, permittivity ε, and conductivity σ with the subscript denoting interior (i) or exterior (e). In this work, the subscript r denotes the ratio between exterior to interior quantities. Typical leaky dielectric fluids are very viscous, and drops are of millimeter size. Thus the fluid flow in this system is governed by the Stokes equation (2.23) with boundary conditions $\boldsymbol{u} = 0$ in the far-field.

The balance of stresses at the fluid interface gives

$$[\![\tau \cdot \boldsymbol{n}]\!] = \gamma(\nabla \cdot \boldsymbol{n})\boldsymbol{n} - \nabla_s \gamma, \tag{3.1}$$

where $\nabla_s \equiv (\mathbf{I} - \boldsymbol{n}\boldsymbol{n}) \cdot \nabla$ is the surface gradient projected on the drop surface, and

$$\tau = -p\mathbf{I} + \mu\left((\nabla \boldsymbol{u})^T + \nabla \boldsymbol{u}\right) + \varepsilon \boldsymbol{E}\boldsymbol{E} - \frac{\varepsilon}{2}(\boldsymbol{E} \cdot \boldsymbol{E})\,\mathbf{I},$$

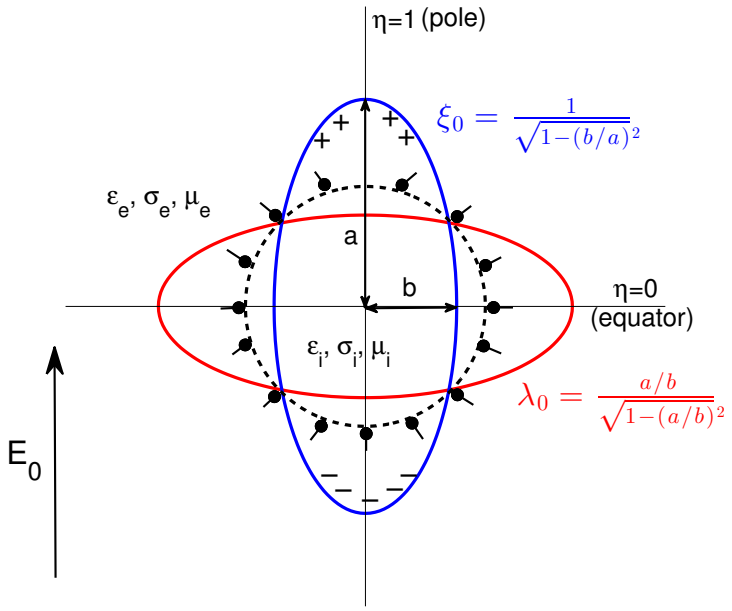

Figure 3.1 Deformation of a viscous drop covered with insoluble surfactant (bead-rod particles) in a DC electric field $E_0\hat{\mathbf{z}}$. Starting from an initially spherical shape (dashed line), the drop can deform to either a prolate (labeled as ξ_0) or an oblate (labeled as λ_0) spheroid at equilibrium. The distances a and b from the center to the pole and equator, respectively.

where $\mathbf{T} = -p\mathbf{I} + \mu\left((\nabla \boldsymbol{u})^T + \nabla \boldsymbol{u}\right)$is the hydrodynamic stress with $\mathbf{I}$ the identity tensor, and $\mathbf{S} = \varepsilon \boldsymbol{E}\boldsymbol{E} - \frac{\varepsilon}{2}(\boldsymbol{E}\cdot\boldsymbol{E})\mathbf{I}$ is the Maxwell stress. The surface tension is γ, which depends on the surface concentration of surfactant Γ, and is described by the Langmuir equation of state

$$\gamma = \gamma_0\left(1 + E\ln\left(1 - \frac{\Gamma}{\Gamma_\infty}\right)\right). \tag{3.2}$$

Here γ_0 is the surface tension of a surfactant-free or "clean" drop, Γ_∞ is the maximum packing concentration, and $E = RT\Gamma_\infty/\gamma_0$ is the elasticity number which quantifies the sensitivity of surface tension to changes in the surfactant concentration on the drop surface.

The surfactant transport on the deforming drop surface is described by

$$\frac{\partial \Gamma}{\partial t} + \nabla_s \cdot (\boldsymbol{u}_s \Gamma) + \kappa \boldsymbol{u}\cdot\boldsymbol{n}\Gamma = D_s \nabla_s^2 \Gamma, \tag{3.3}$$

where κ is the mean curvature, and D_s is the surfactant diffusivity. Here the focus is on non-diffusing surfactant, hence $D_s \approx 0$.

The electric field is irrotational so that $\boldsymbol{E} = -\nabla\phi$, where the exterior and interior electric potentials are given by (2.20)-(2.21). At the fluid interface the tangential electric field is continuous, while there is a jump in the normal electric field due to the balance of currents between the ohmic current and the rate of change of the surface charge density $q_s \equiv [\![-\varepsilon\nabla\phi\cdot\boldsymbol{n}]\!]$:

$$[\![-\nabla\phi\cdot\boldsymbol{t}]\!] = 0, \quad [\![\sigma\nabla\phi\cdot\boldsymbol{n}]\!] = \frac{dq_s}{dt}, \tag{3.4}$$

where $\boldsymbol{u}_s \equiv (\mathbf{I} - \boldsymbol{n}\boldsymbol{n})\cdot\boldsymbol{u}$ is the tangential velocity on the surface. For the fluids considered here, typical material properties are $\mu \sim 10^{-3}$Pa.s, $\sigma \sim 1\mu$S/m, $\varepsilon \sim 10^{-12}$F/m. Using these estimates, one can show that the charge relaxation time-scale τ_C is much faster than that (τ_{EHD}) of the EHD flow: $\tau_C \ll \tau_{EHD}$. Thus $dq_s/dt \approx 0$,

and (3.4) is reduced to

$$[\![-\nabla\phi\cdot\boldsymbol{t}]\!]=0,\quad [\![\sigma\nabla\phi\cdot\boldsymbol{n}]\!]=0. \tag{3.5}$$

The tangential and normal stress balances are given by

$$[\![\mathbf{T}_{\xi\eta}]\!]+[\![\mathbf{S}_{\xi\eta}]\!]+\nabla_s\gamma=[\![\mathbf{T}_{\xi\eta}]\!]+[\![\mathbf{S}_{\xi\eta}]\!]+\frac{1}{h_\eta}\frac{\partial\gamma}{\partial\eta}=0, \tag{3.6}$$

$$[\![\mathbf{T}_{\xi\xi}]\!]+[\![\mathbf{S}_{\xi\xi}]\!]-\gamma(\nabla\cdot\boldsymbol{n})=0, \tag{3.7}$$

where

$$\mathbf{T}_{\xi\xi}=-p+2\mu\left(\frac{\partial v}{h_\xi\partial\xi}+\frac{u}{h_\xi h_\eta}\frac{\partial h_\xi}{\partial\eta}\right),\quad \mathbf{T}_{\xi\eta}=\mu\left(\frac{\partial(u/h_\eta)}{\partial\xi}\frac{h_\eta}{h_\xi}+\frac{\partial(v/h_\xi)}{\partial\eta}\frac{h_\xi}{h_\eta}\right), \tag{3.8}$$

$$\mathbf{S}_{\xi\xi}=\frac{\varepsilon}{2}\left(E_\xi^2-E_\eta^2\right),\quad \mathbf{S}_{\xi\eta}=\varepsilon E_\xi E_\eta, \tag{3.9}$$

where h_ξ and h_η are the scale factors in the spheroidal coordinates, $E_\xi=-\frac{\partial\phi}{\partial\xi}$ and $E_\eta=-\frac{\partial\phi}{\partial\eta}$ are the normal and tangential electric field.

The pressure is computed using

$$\frac{\partial p}{\partial\eta}=-\mu\frac{\partial\left(\Xi^2\psi\right)}{\partial\xi}\frac{h_\eta}{h_\xi h_\zeta}, \tag{3.10a}$$

$$\frac{\partial p}{\partial\xi}=\mu\frac{\partial\left(\Xi^2\psi\right)}{\partial\eta}\frac{h_\xi}{h_\eta h_\zeta}, \tag{3.10b}$$

where the operator

$$\Xi^2\equiv\frac{1}{c^2(\xi^2-\eta^2)}\left[(\xi^2-1)\frac{\partial^2\psi}{\partial\xi^2}+(1-\eta^2)\frac{\partial^2\psi}{\partial\eta^2}\right].$$

The jump in pressure, $[\![-p]\!]$ can be expressed in terms of the coefficients, A's and B's of the stream function, and the rate of change of the shape parameter, ξ_0'.

The coefficients of the stream function in (2.36)-(2.37) are computed using the continuity of velocities, the kinematic condition $\frac{d\boldsymbol{x}}{dt}=(\boldsymbol{u}\cdot\boldsymbol{n})\boldsymbol{n}$, and the stress balances

projected onto the corresponding velocities [37, 137]:

$$\int_{\xi=\xi_0(t)} u\left[[\![\mathbf{T}_{\xi\eta}]\!]+[\![\mathbf{S}_{\xi\eta}]\!]+\frac{1}{h_\eta}\frac{\partial\gamma}{\partial\eta}\right]ds=0, \tag{3.11}$$

$$\int_{\xi=\xi_0(t)} v\left[[\![\mathbf{T}_{\xi\xi}]\!]+[\![\mathbf{S}_{\xi\xi}]\!]-\gamma(\nabla\cdot\boldsymbol{n})\right]ds=0, \tag{3.12}$$

where $ds = h_\eta h_\zeta d\eta$ is the surface element in prolate spheroidal coordinates. The reason for projecting the stress balances onto the velocity field lies in the fact that the total force on the drop interface cannot be balanced at every point in the spheroidal framework.

For a clean drop γ is constant, and the transient dynamics toward equilibrium is well captured by the spheroidal model. To derive an equation for equilibrium shape of a surfactant-covered drop, a different approach is taken based on the fact that fluid flow vanishes at equilibrium in the presence of diffusion-free, insoluble surfactant. Consequently, A's, B's $\to 0$, $\xi_0' \approx 0$, and the tangential electric stress is balanced solely by the Marangoni stress,

$$[\![\mathbf{S}_{\xi\eta}]\!]+\frac{1}{h_\eta}\frac{\partial\gamma}{\partial\eta}=0. \tag{3.13}$$

The system is well-posed with the projected normal stress balance

$$\int_{\xi=\xi_o(t)} v\left[[\![\mathbf{S}_{\xi\xi}]\!]-\gamma(\nabla\cdot\boldsymbol{n})\right]ds=0. \tag{3.14}$$

Integrating (3.13) and scaling the electric potential by $E_0 r_0$, distance by r_0, and surface tension by $\gamma_{eq} = \gamma_0(1 + E\ln(1-\chi))$ (where $\chi = \Gamma_{eq}/\Gamma_\infty$ is the surfactant coverage), we obtain the equilibrium (dimensionless) tension profile

$$\gamma = Ca_E f(\xi_0)\sqrt{\xi_0^2-\eta^2}+A, \tag{3.15}$$

$$f(\xi_0) = \frac{\sqrt{\xi_0^2-1}}{c}\left[(-c+\alpha Q_1')(-c\xi_0+\alpha Q_1)-\frac{\beta^2\xi_0}{\varepsilon_r}\right], \tag{3.16}$$

where $Q_1 \equiv Q_1(\xi_0)$ and $Q_1' \equiv Q_1'(\xi_0)$. The integration constant A is determined from conservation of the total amount of surfactant, $\int_{-1}^{1} \Gamma ds = \chi \int_{-1}^{1} ds$. Using the (dimensionless) Langmuir equation of state

$$\gamma = \gamma_0 \left(1 + E \ln\left(1 - \chi\Gamma\right)\right),$$

the constant of integration reads

$$A = \frac{\gamma_0}{\gamma_{eq}} \left[1 - E - \ln\left(\frac{\int_{-1}^{1} \sqrt{\xi_0^2 - \eta^2} d\eta - \frac{2\chi}{c\sqrt{\xi_0^2 - 1}}}{\int_{-1}^{1} \sqrt{\xi_0^2 - \eta^2} e^{\frac{\gamma_{eq}}{\gamma_0} Ca_E f(\xi_o) \sqrt{\xi_0^2 - \eta^2}} d\eta} \right) \right]. \tag{3.17}$$

Substituting the equilibrium surface tension, v, $\mathbf{S}_{\xi\xi}$ and the curvature $\nabla \cdot \boldsymbol{n}$ into (3.14), the corresponding drop shape ξ is obtained by solving the non-linear equation

$$\frac{Ca_E}{c\xi_0} \left[(-c + \alpha Q_1')^2 + \left(-c + \alpha \frac{Q_1}{\xi_0} \right)^2 - 2\beta^2 \right] g(\xi_0) = \int_{-1}^{1} \frac{(1 - 3\eta^2)(2\xi_0^2 - 1 - \eta^2)\gamma}{\sqrt{\xi_0^2 - 1}(\xi_0^2 - \eta^2)^{3/2}} d\eta, \tag{3.18}$$

$$g(\xi_0) = \frac{\xi_0^2}{2} \int_{-1}^{1} \frac{(1 - 3\eta^2)(\eta^2 - 1)}{\xi_0^2 - \eta^2} d\eta. \tag{3.19}$$

For a given Ca_E and $(\sigma_r, \varepsilon_r)$, a solution ξ_0 of (3.18) is admissible if the tension and surfactant profiles are physical, i.e., tension is positive everywhere and surfactant concentration never drops below zero. For an oblate drop, the derivation follows the above formulation with some modifications: The oblate spheroidal coordinates (λ, η) are similarly expressed in the cylindrical coordinates (r, z) as $z = \bar{c}\lambda\eta$, $r = \bar{c}\sqrt{(\lambda^2 + 1)(1 - \eta^2)}$, with $\bar{c} = \sqrt{b^2 - a^2}$ for the oblate drop. Surfaces of constant $\lambda \in [0, \infty)$ are spheroids while surfaces of constant $\eta \in [-1, 1]$ are hyperboloids. The oblate spheroidal coordinates can be transformed from the prolate spheroidal coordinates by substituting $\xi \to \mathbf{i}\lambda$ with $\mathbf{i} = \sqrt{-1}$.

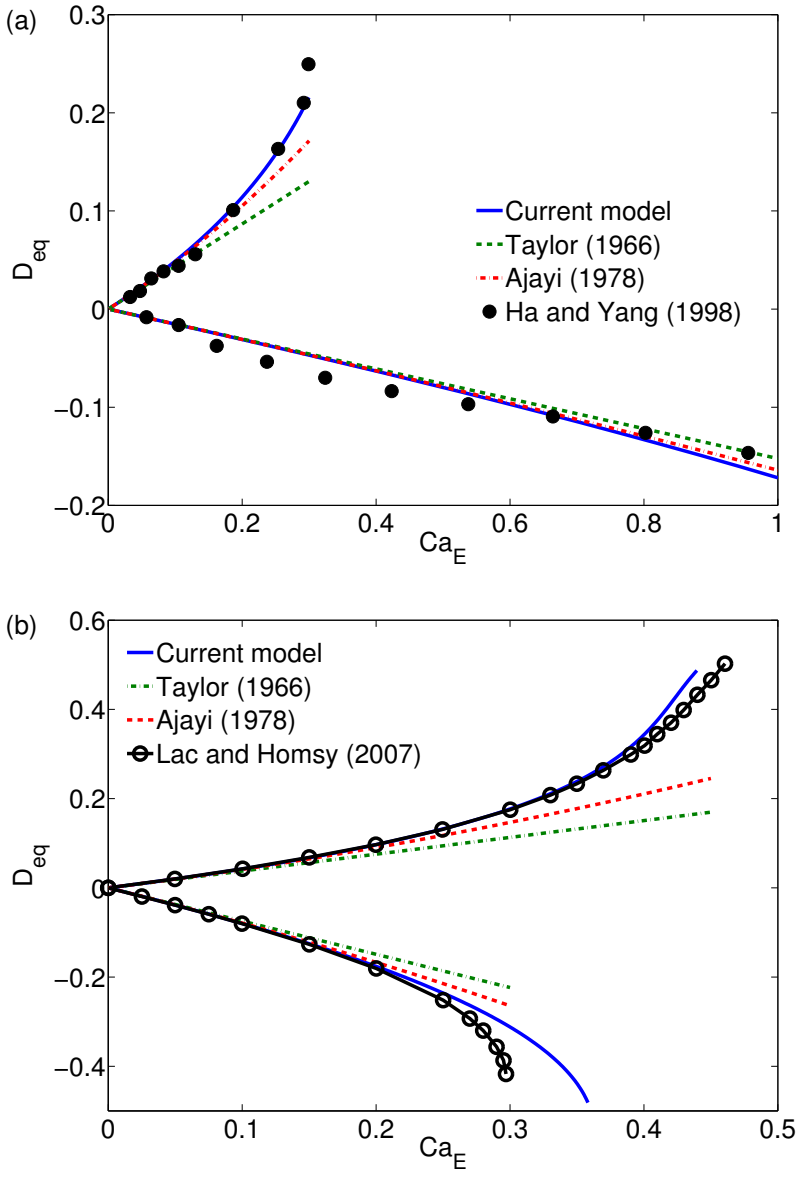

Figure 3.2 Equilibrium deformation for a clean drop in a DC electric field: Spheroidal model (solid line), Taylor's spherical model [147] (dashed line), and Ajayi's second-order model [1] (dashed-dotted line). (a) Symbols are experiments from [54]; $(\varepsilon_r, \sigma_r, \mu_r) = (0.73, 0.1, 1.14)$ for the prolate drop ($D_{eq} > 0$), $(\varepsilon_r, \sigma_r, \mu_r) = (1.39, 6.67, 1.28)$ for the oblate drop ($D_{eq} < 0$). (b) Symbols are numerical results from [77]; $(\varepsilon_r, \sigma_r, \mu_r) = (0.02, 0.04, 1)$ for the prolate drop, and $(\varepsilon_r, \sigma_r, \mu_r) = (0.5, 10, 1)$ for the oblate drop.

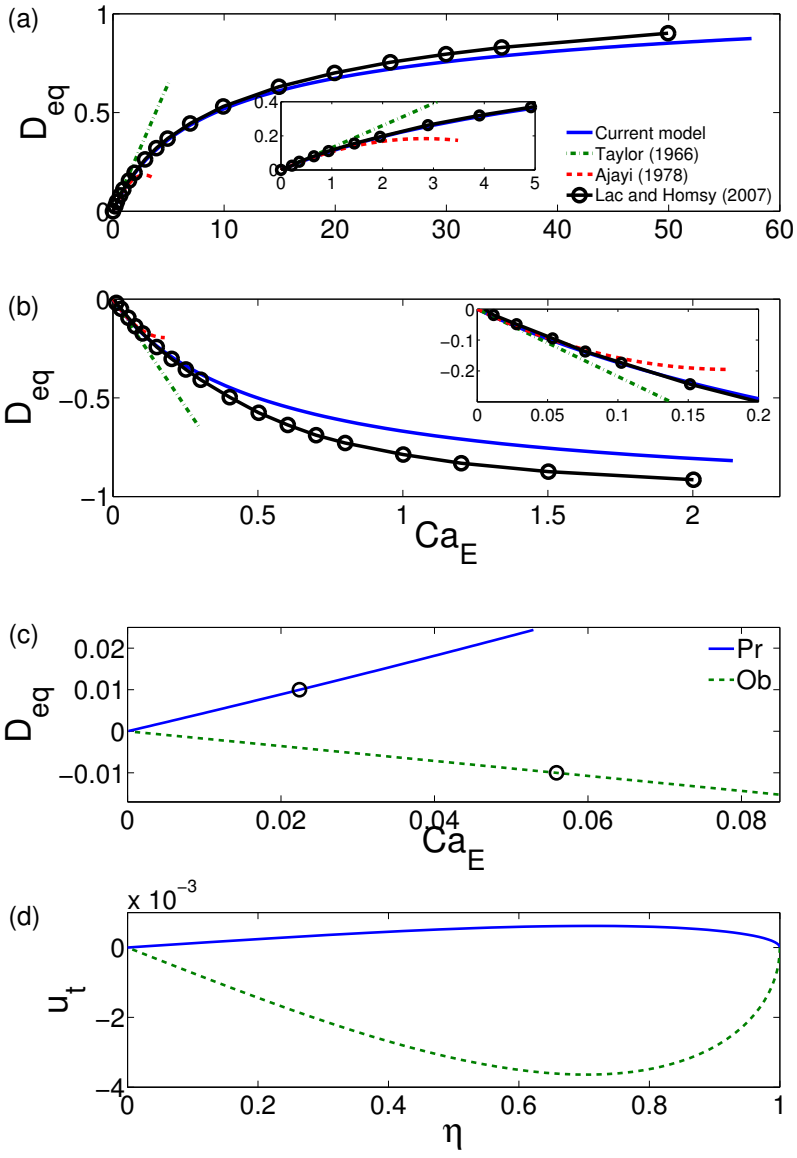

Figure 3.3 ((a) and (b)) Comparison of the current model (solid line), Taylor's model [147] (dashed line), and Ajayi's second order approximation [1] (dashed-dotted line). Symbols are numerical results from [77]. Here $(\varepsilon_r, \sigma_r, \mu_r) = (25, 10, 1)$ for panel (a) and $(\varepsilon_r, \sigma_r, \mu_r) = (0.05, 0.5, 1)$ for panel (b). ((c) and (d)) Tangential flow between an oblate $(\varepsilon_r, \sigma_r, \mu_r) = (1.37, 10, 1)$ and a prolate $(\varepsilon_r, \sigma_r, \mu_r) = (0.73, 0.1, 1)$ drop at $|D_{eq}| = 0.01$.

3.3 Model Validation: Clean Spheroidal Drop

The electro-deformation of a clean viscous drop in a DC electric field has been investigated analytically [1, 10, 147, 169], numerically [43, 77, 102] and experimentally [54, 55, 147, 154]. In particular, large electro-deformation has been modeled by Bentenitis and Krause [10] and Zhang *et al.* [169]. The theoretical results in [10] compare reasonably well with experimental data, though better agreement is obtained for the prolate cases than for the oblate cases; there are no comparisons for the oblate cases in [169]. As a validation, this work presents a spheroidal model for both prolate and oblate spheroidal shapes (derived in Appendix C), and compares the spheroidal results against the second-order small-deformation theory (see Appendix B). The spheroidal model is also compared with experimental and numerical data for a clean viscous drop.

Figure 3.2 shows the dependence of equilibrium drop deformation on the electric capillary number Ca_E predicted by three models. The theories are compared to experimental data (Figure 3.2(a)) and numerical simulation data (Figure 3.2(b)). Results from the present spheroidal model (solid curve) agree with both experimental data and the numerical simulations for a wide range of electric capillary number. In addition, one notes that the spheroidal model is almost exactly the same as the numerical simulation results for deformation $|D_{eq}|$ up to 0.2. Taylor's [147] prediction gives reasonable agreement for Ca_E up to 0.1 for most cases, while Ajayi's [1] second-order approximation is consistently between Taylor's results and the spheroidal results for all four cases in Figure 3.2.

Figure 3.3(a) shows two more examples of comparison of equilibrium drop deformation between models and results from the boundary integral simulations of Lac and Homsy [77] with parameters that allow an equilibrium spheroidal drop for all values of the capillary number for both prolate (panel (a)) and oblate (panel (b)) drops. For the prolate case we see that the spheroidal model is far superior

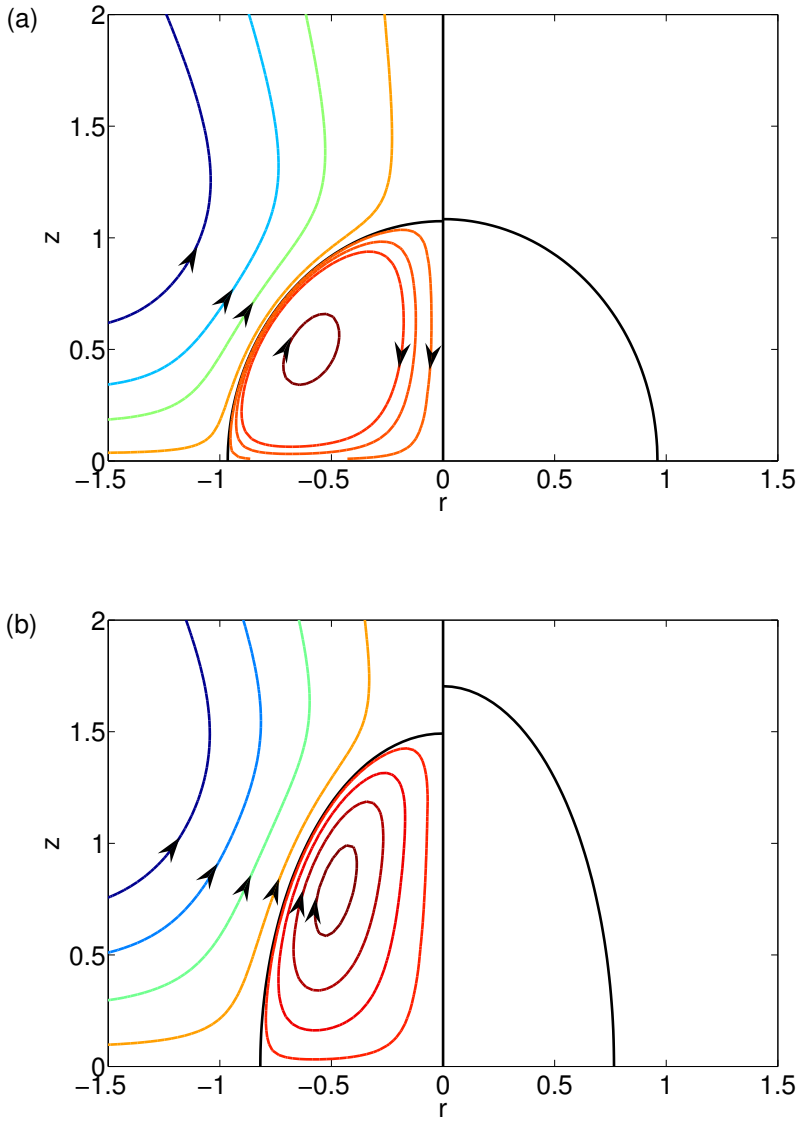

Figure 3.4 Comparison of equilibrium drop shape and circulation for Case A in Ref. [148] where $(\varepsilon_r, \sigma_r, \mu_r) = (1, 0.33, 1)$. $Ca_E = 0.2$ for panel (a) and $Ca_E = 0.8$ for panel (b). Clean drop with circulation is on the left of each panel. On the right the drop is covered with $\chi = 0.7$ and the circulation is completely suppressed by the non-diffusing surfactant.

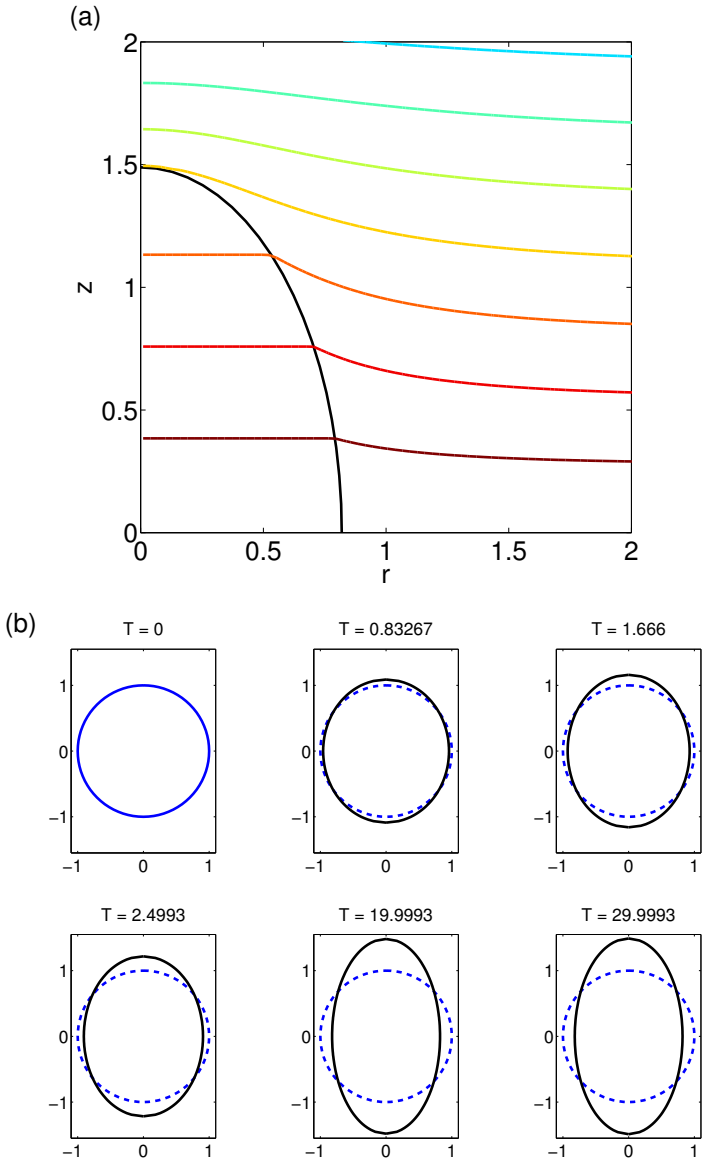

Figure 3.5 Electric potential lines (a) and time-dependent dynamics (b) for the clean viscous drop of Case A in [148] where $(\varepsilon_r, \sigma_r, \mu_r) = (1, 0.33, 1)$. The electric capillary number is $Ca_E = 0.8$. The dashed curve denotes the initial drop shape.

than Taylor's or Ajayi's results, and good agreement is obtained for deformation up to $D_{eq} \approx 0.5$. For the oblate case the spheroidal model gives the best agreement again, yet it begins to deviate significantly from the axial-symmetric results around $|D_{eq}| > \approx 0.3$. Figures 3.3(c) and 3.3(d) show a comparison of tangential flow between prolate and oblate. At a given Ca_E, the prolate deformation is larger than the oblate deformation. For a given deformation, say $D_{eq} = 0.01$ (circles in Figure 3.3(c)), the fluid flow is larger for the prolate drop than for the oblate drop. Based on these findings it is concluded that an initially uniform surfactant concentration will be much more redistributed in the oblate case before an equilibrium is reached and the Marangoni stress is established. Finally, Figure 3.4 shows the comparison of equilibrium drop shape and circulation between clean and surfactant-covered drops from the spheroidal model with $\chi = 0.7$ and parameters for Case A in Ref. [148]. On the left is a clean drop with circulation, and on the right is a surfactant-covered drop at equilibrium, depleted of any flow due to the immobilized fluid interface covered with non-diffusing surfactant. Figure 3.5(a) shows the corresponding electric potential lines for $Ca_E = 0.8$; the corresponding time-dependent deformation of the drop is shown in Figure 3.5(b).

3.4 Results

For a clean viscous drop, the spheroidal model can capture the equilibrium deformation up to $D_{eq} \approx 0.2$ for both prolate and oblate drops. Consequently, the focus is put on equilibrium drop deformation $|D_{eq}| \leq 0.2$ in the following results and discussion. In addition, the range of elasticity number is fixed $0.03 \leq E \leq 0.3$ (for a detailed discussion on the realistic ranges of E see Refs. [113, 38]). In the absence of surfactant, there are two prolate shapes: Prolate A with circulation from the equator to the pole, and prolate B with circulation from the pole to the equator (the same as in the oblate drop). As non-diffusing surfactant completely suppresses fluid flow at equilibrium

(Figure 3.4), there is no distinction (in terms of flow around the drop) between the two prolate modes. The complete suppression of flow due to the Marangoni stress also implies that the equilibrium drop deformation does not depend on viscosity mismatch.

3.4.1 Existence of Spheroidal Equilibrium

Taylor's spherical model for a clean viscous drop in a DC electric field gives the boundary (dashed line in Figure 3.6(a) with $\mu_r = 1$) between prolate and oblate drops in the $(\sigma_r, \varepsilon_r)$-plane. A prolate A drop is found for $\varepsilon_r > \sigma_r$ (above the dashed-dotted line), while a prolate B drop is found for $\varepsilon_r < \sigma_r$. More details on a clean viscous drop in a DC field can be found in Lac and Homsy [77]. For a viscous drop covered with non-diffusing surfactant in a DC electric field, the second- order small-deformation predicts a spherical shape when $D_L = 0$, which gives the solid lines in Figure 3.6(a).

It is not possible to derive such a discriminating condition analytically from the spheroidal model. Instead the spheroidicity of the equilibrium shape around $D_L = 0$ is checked numerically, and the transition between prolate and oblate across $D_L = 0$ boundary is verified. In addition, the spheroidal model can provide the existence of admissible equilibrium spheroidal shapes in the $(\sigma_r, \varepsilon_r)$-plane. Using the Langmuir equation of state, the equilibrium surface tension and drop shape from Equations (3.15) and (3.18) are calculated for a given set of $(\sigma_r, \varepsilon_r)$. The existence of an equilibrium spheroidal drop is established if both the surface tension and surfactant distribution are physical: $\gamma > 0$ from (3.15) and $0 \leq \chi\Gamma < 1$ from the equation of state. Figure 3.6(a) shows the existence of equilibrium for a spheroidal drop with $(E, \chi) = (0.1, 0.1)$ and three values of Ca_E denoted by three types of symbols (see legend). Overall one observes that almost all (except one) equilibrium spheroidal solutions are prolate for $(E, \chi) = (0.1, 0.1)$, and the region of existence for spheroidal equilibrium gets smaller as Ca_E increases. Figure 3.6(b) shows the boundaries for the existence of spheroidal equilibrium at $Ca_E = 0.2$ for four combinations of E and

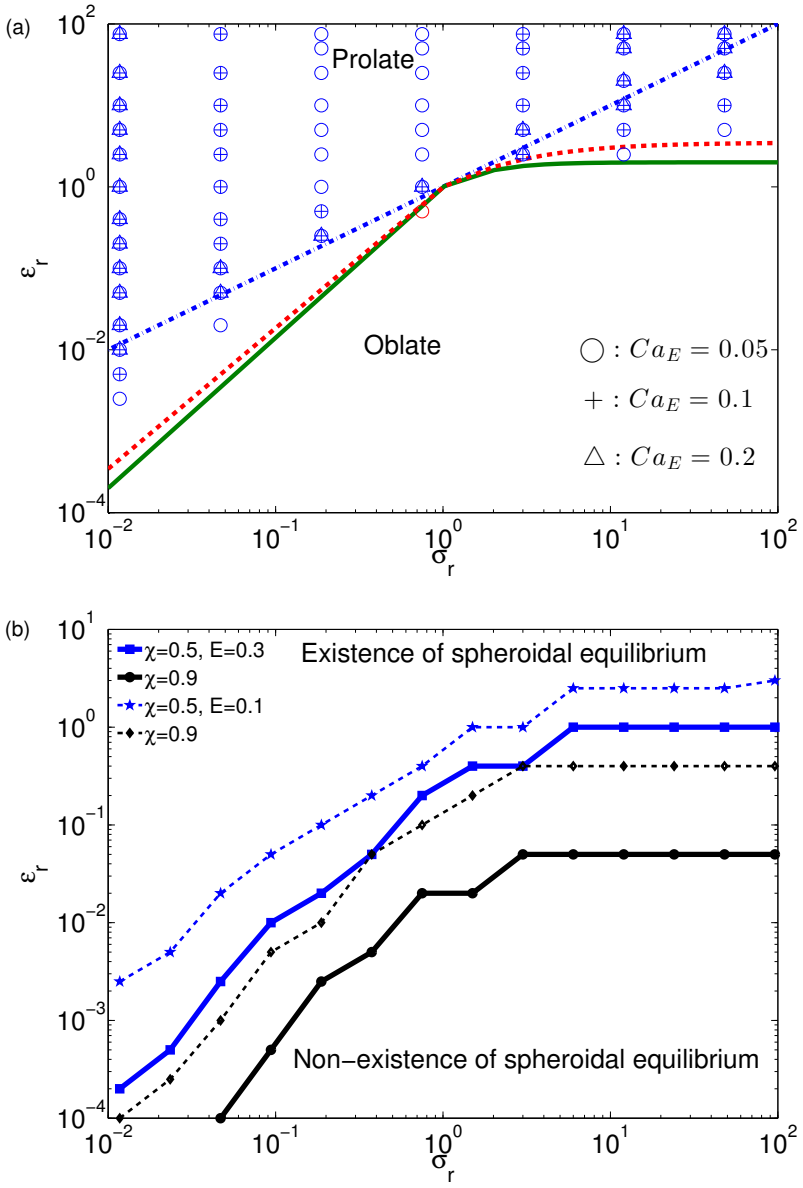

Figure 3.6 Shape and equilibrium boundaries on the $(\sigma_r, \varepsilon_r)$-diagram. (a) Symbols denote that a spheroidal equilibrium can be found at those points with $(E, \chi) = (0.1, 0.1)$, $Ca_E = 0.05$, 0.1, and 0.2 (see legend). Solid line is the boundary between prolate and oblate drops from the small-deformation theory. (b) Boundaries for spheroidal equilibrium using $Ca_E = 0.2$ with different values of E and χ (see legend). No spheroidal equilibrium is found below the boundary.

χ. For points on the boundaries, the value of ε_r is the lower bound for a spheroidal equilibrium at that value of σ_r : No equilibrium can be found below this point. The lack of existence of a spheroidal equilibrium implies that the spheroidal shape is not stable for these parameters. It is possible that non-spheroidal axisymmetric equilibrium drop shape would be stable as in the case of clean drop [77]. A larger region of spheroidal equilibrium is found for larger χ and/or larger E.

3.4.2 Comparison against Experiments and Numerical Simulations

Ha and Yang [51, 52] used soluble surfactant to investigate the electro-deformation of a surfactant-covered viscous drop in a DC electric field. The normalized surfactant coverage χ on the drop surface can be computed from C_∞, the soluble surfactant concentration, as $\chi = \frac{C_\infty}{C_\infty+\delta}$ assuming that (1) surfactant exchange between the bulk and the drop surface is in equilibrium and (2) the soluble surfactant concentration is homogeneous and remains constant. The parameter δ is an equilibrium coefficient related to the adsorption/desorption rate coefficients [4]. One can estimate E and δ by fitting the surface tension isotherm (Figure 9 of Ha and Yang [52]) to the formula

$$\gamma_C = \gamma_0 + RT\Gamma_\infty \ln\left(1 - \frac{C_\infty}{C_\infty + \delta}\right), \tag{3.20}$$

where γ_C is the surface tension in the presence of soluble surfactant. We find that (1) for experiments 1-6, $E \approx 0.06$, $\delta \approx 6.46 \times 10^{-7} M$, and $0.13 < \chi < 0.99$, (2) for experiments 7-12, $E \approx 0.08$, $\delta \approx 6.00 \times 10^{-7} M$, and $0.14 < \chi < 0.99$, (3) for experiments 13-17, $E \approx 0.04$, $\delta \approx 7.74 \times 10^{-8} M$, and $0.5 < \chi < 0.99$, and (4) for experiments 18-21, $E \approx 0.04$, $\delta \approx 4.0 \times 10^{-5} M$, and $0.65 < \chi < 0.97$. Due to limited data points for experiments 18-21 (three points for fitting in Figure 9 of Ref. [52]), the error of these estimates is quite large. There are no data for experiments 22-27 where the interior/exterior combination is silicone oil/castor oil, which is opposite to experiments 18-21.

The equilibrium drop deformation as a function of electric capillary number is calculated with the above estimates for (E, δ) and χ at a given C_∞. Figure 3.7 shows the comparison of D_{eq} versus Ca_E (or Weber number in Ha and Yang [52]) between experiments (symbols), second-order small- deformation (dashed-dotted line) and spheroidal model (solid line). Note that in the small deformation theory the equilibrium drop deformation D_{eq} does not depend on μ_r, and its dependence on the elasticity number is implicit through the equilibrium surface tension in the electric capillary number Ca_E (see [109] or Appendix B). Panel (a) is the comparison for a prolate drop (experiments 6 and 8 from Figure 4 of Ref. [52]), and panel (b) is the comparison for an oblate drop (experiment 25 from Figure 6 of Ref. [52]). Experiment 25 is used to represent the data set of experiments 22-25. Because (E, δ) for experiments 22-25 cannot be estimated from the data, the same value of (E, δ) from experiment 21 (panel (c)) is used, which is representative of experiments 18-21 (see Figure 5 of Ref. [52]).

The equilibrium drop deformation from the small-deformation analysis does not dependent on (E, χ), and agrees with the spheroidal model and the experiments for $Ca_E \leq 0.1$. The spheroidal model results, on the other hand, depend on (E, χ) and agree well with the experiments for large Ca_E. From the prolate comparison in Figures 3.7(a) and 3.7(c), one can conclude that the small-deformation results are reliable for D_{eq} up to 0.1, while the spheroidal model agrees with the experimental data up to $D_{eq} \approx 0.2$. For the oblate deformation in Figure 3.7(b), small-deformation results agree well with spheroidal results, yet both are very different from experiments. In the inset of Figure 3.7(b), the experimental capillary number is multiplied by 2.7. The result shows excellent agreement between the theories and the experiment, suggesting that the measurements of the electric properties of the fluids may be erroneous.

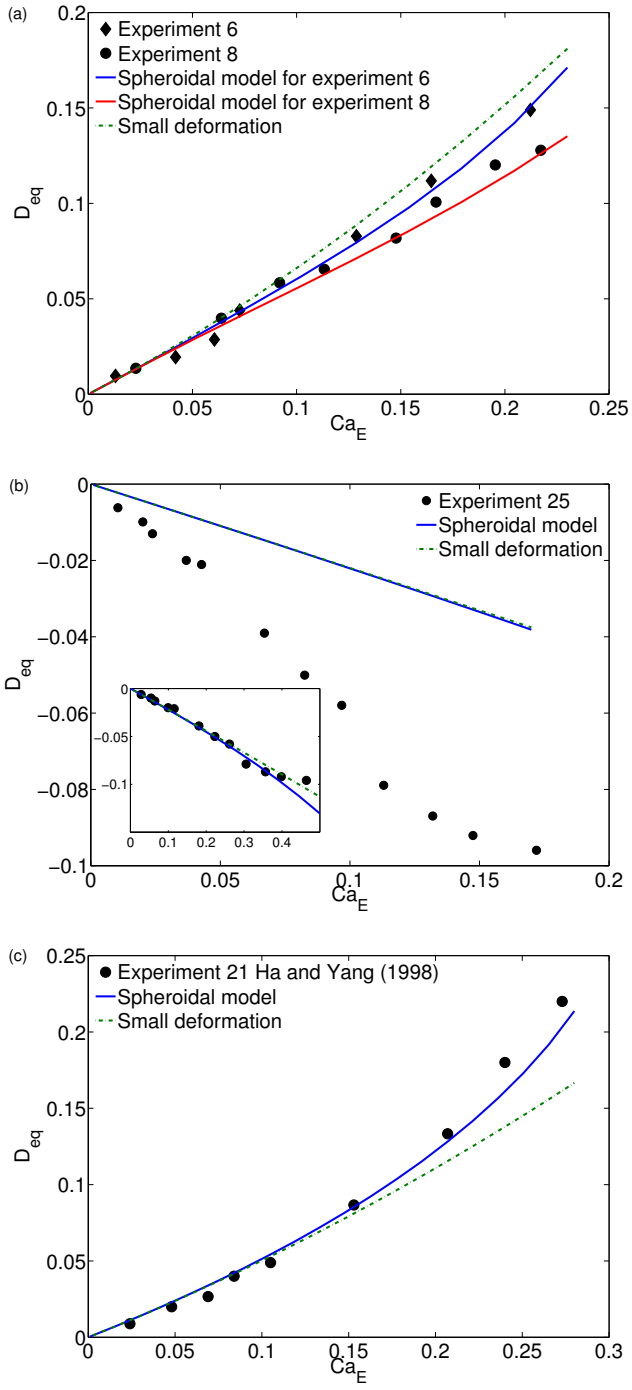

Figure 3.7 Equilibrium deformation from experiments [52] (symbols), predictions from small-deformation (dashed-dotted lines), and spheroidal results (solid lines). (a) $(\varepsilon_r, \sigma_r, \mu_r) = (0.0355, 10^{-6}, 10^3)$. (b) $(\varepsilon_r, \sigma_r, \mu_r) = (1.3, 10, 15.38)$. (c) $(\varepsilon_r, \sigma_r, \mu_r) = (0.73, 0.1, 12.5)$. See text for values of (E, χ).

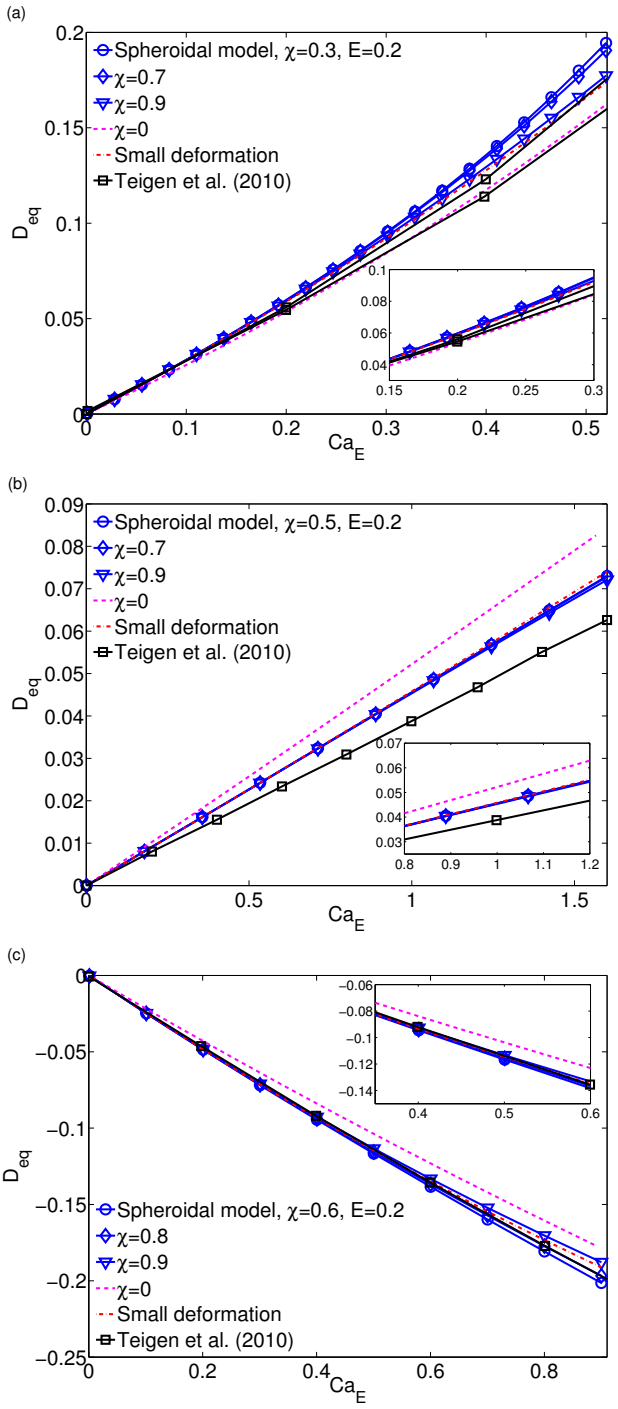

Figure 3.8 Comparison of the equilibrium drop deformation. Simulations from [148] (see legend), or models from the second-order small-deformation (dashed-dotted lines), and spheroidal theories (see legend). (a) Case A. (b) Case B. (c) Case C. See text for values of electric and surfactant parameters.

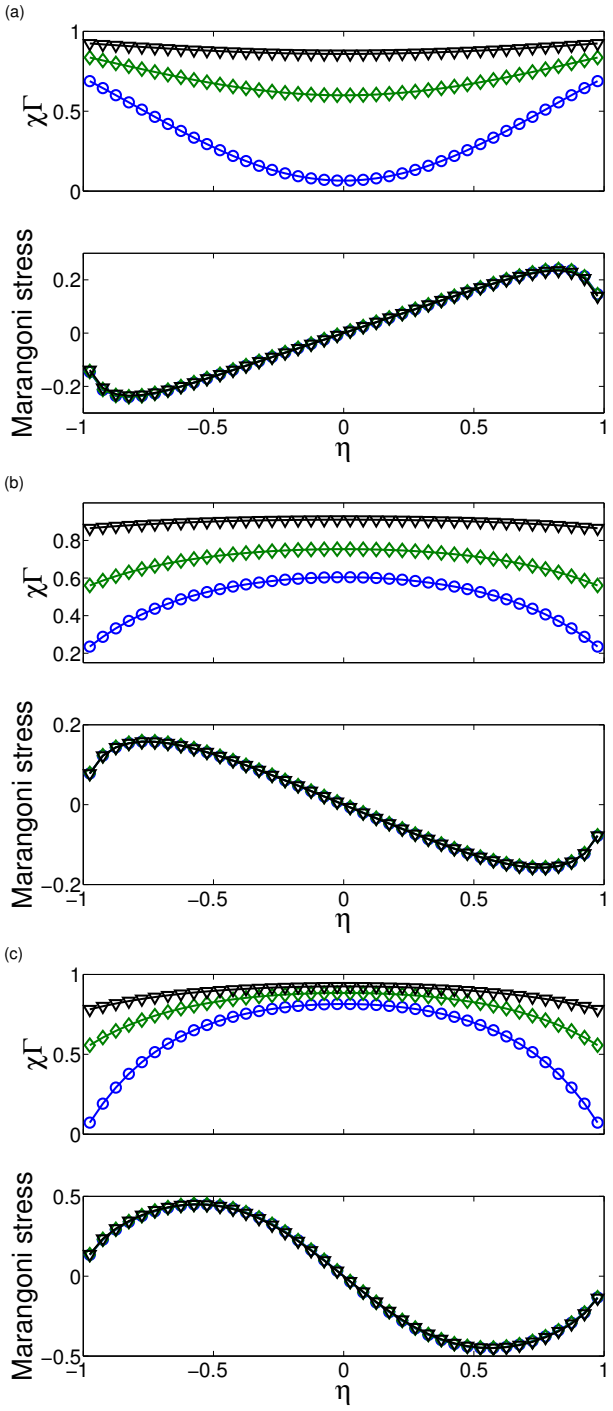

Figure 3.9 Distribution of surfactant concentration $\chi\Gamma$ and Marangoni stress for Figure 3.8. (a) Case A in Ref. [148] with $Ca_E = 0.46$. (b) Case B in Ref. [148] with $Ca_E = 1.6$. (c) Case C in Ref. [148] with $Ca_E = 0.9$.

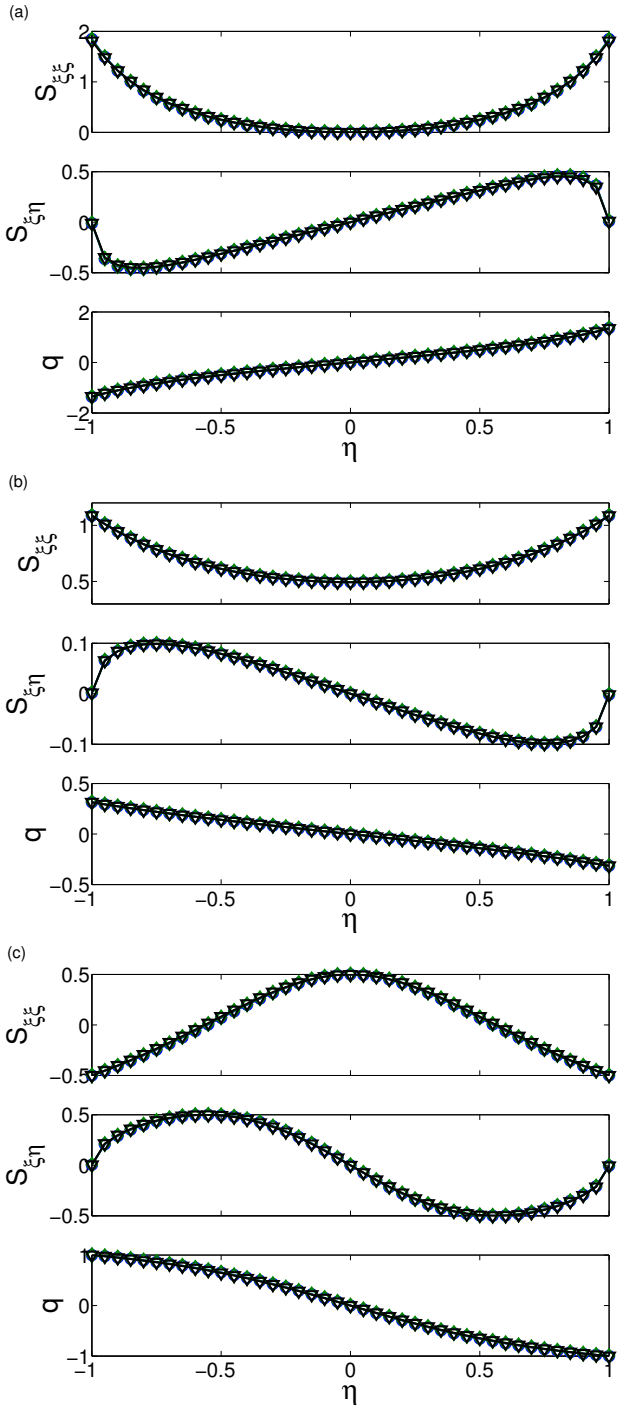

Figure 3.10 Distribution of normal electric stresses $S_{\xi\xi}$, tangential electric stresses $S_{\xi\eta}$, and surface charge q for Figure 3.8. (a) Case A in Ref. [148] with $Ca_E = 0.46$. (b) Case B in Ref. [148] with $Ca_E = 1.6$. (c) Case C in Ref. [148] with $Ca_E = 0.9$.

Teigen and Munkejord [148] numerically investigated the deformation of a drop covered with diffusing insoluble surfactant with a small Peclet number (10). They studied three special cases: A prolate A drop, a prolate B drop, and an oblate drop. Their axisymmetric simulation results showed that the fluid flow at equilibrium is not completely suppressed by the diffusing surfactant. They also reported that surfactant increases the equilibrium drop deformation for prolate A and oblate drops, while for prolate B the deformation is reduced by surfactant.

Figure 3.8 shows the comparison of D_{eq} for these three cases. For small Ca_E, one can note that the spheroidal results agree with both the simulation results [148] and the small-deformation results in all three cases. This finding enhances the credibility of our oblate results in Figure 3.7(b), and implies that the oblate experimental data (experiments 22-25 and 27 from Figures 6 and 7 in Ref. [52]) may be erroneous. Furthermore, it is found that surfactant indeed increases $|D_{eq}|$ for small Ca_E. For large Ca_E, close inspection in Figure 3.8 shows a non-monotonic dependence on the surfactant coverage. Such behavior is explained in terms of surface dilution and tip stretching in Section 3.4.3.

Figure 3.9 shows the distribution of surfactant concentration and Marangoni stress and Figure 3.10 shows electric stresses and surface charge distribution for the parameters in Figure 3.8. Comparing Figure 3.9(a) with Figures 9 and 10 in Ref. [148] (arc length $s = 3$ in their results corresponds to $\eta = 0$), one can observe similar surfactant concentration and Marangoni stress distributions, even though Marangoni stress from the spheroidal model is quite insensitive to χ. The electric stresses and induced surface charge in Figure 3.10 are also insensitive to χ. One further notes that, even though the non-diffusing surfactant completely suppresses the fluid flow, the spheroidal results for the prolate B parameters (Case B) are more similar to results for the oblate parameters (Case C) in terms of distributions of Marangoni stress, tangential electric stress and the induced surface charge.

3.4.3 Surface Dilution versus Tip Stretching

A measure to quantify the surfactant effect is the average surface tension defined as [113]

$$\gamma_{avg} \equiv \frac{\int_{\xi=\xi_0(t)} \gamma ds}{\int_{\xi=\xi_0(t)} ds}. \tag{3.21}$$

At high surfactant coverage, drop deformation dilutes the surfactant concentration and increases the average surface tension $\gamma_{avg} > 1$, leading to smaller drop deformation than the uniform tension (clean drop) case at a given Ca_E. On the other hand, if the surfactant coverage is small, larger surfactant concentration gradient is easily realized when surfactant accumulates at the drop tips, leading to higher curvature by stretching out to the exterior (and hence larger drop deformation) [113]. The latter mechanism is called tip stretching for $\gamma_{avg} < 1$, while the former mechanism is called surface dilution for $\gamma_{avg} > 1$.

Adding more surfactant in the tip-stretching dominant regime leads to larger drop deformation [38, 113]. Another signature of tip stretching is the large surfactant concentration gradient, and hence the Marangoni stress. However, when surface dilution takes over, surfactant leads to less drop deformation and smaller surfactant concentration gradient (Marangoni stress) is expected [113].

Figure 3.11 shows the average surface tension for the three cases in Figure 3.8. As the surfactant coverage increases, one can see that the dominant mechanism goes from tip stretching to surface dilution in all three cases. Significant decrease in drop deformation with increasing surfactant coverage is observed for both prolate A (Case A, Figure 3.8(a)) and oblate (Case C, Figure 3.8(c)), while very little change in D_{eq} is found for prolate B.

To further illustrate that the average surface tension is a good indicator for the underlying physical mechanisms involving surfactant, the equilibrium drop shape is computed using the same parameters for Figure 19 in Lac and Homsy [77] with

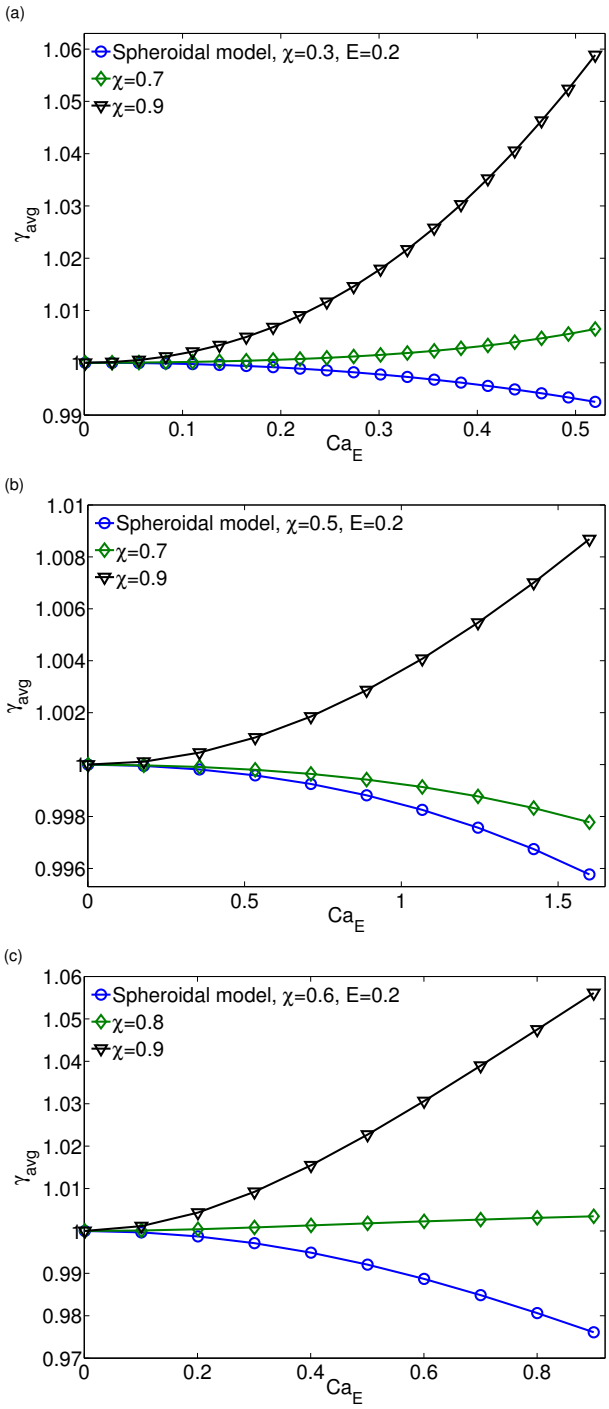

Figure 3.11 Average surface tension for the three cases in Ref. [148]. Panels (a), (b), and (c) correspond to Cases A, B, and C, respectively.

different values of surfactant coverage χ. Figure 3.12(a) shows D_{eq} versus Ca_E at four values of surfactant coverage, and Figure 3.12(b) shows the corresponding equilibrium surfactant concentration distribution (top) and Marangoni stress (bottom). The results show that surfactant-laden drop has larger D_{eq} for $0 < \chi \leq 0.7$. For $\chi = 0.9$ the large surfactant coverage leads to smaller D_{eq} compared to the clean drop for $Ca_E > 0.03$. The Marangoni stress distribution (panel (b)) is almost identical for all surfactant coverages, while the average surface tension in panel (c) clearly indicates that surface dilution is much more dominant at $\chi = 0.9$, and thus smaller drop deformation for $\chi = 0.9$ in panel (a). Similar behavior is also reported for the surfactant effects on the deformation of a viscous drop in an extensional flow [38, 113]. Such non-monotonic surfactant dependence of the equilibrium drop deformation is not captured by the second-order small-deformation theory.

3.5 Conclusion

In this work, the effect of surfactant on equilibrium drop deformation was investigated theoretically. Small deviations from sphericity were analyzed by a second-order small-deformation theory. Large deformations were described by a spheroidal model based on [169]. In contrast to the approach in [169], the tangential electric stress was balanced by the Marangoni stress at equilibrium in the presence of non-diffusing surfactant. As a result, the equilibrium surface tension was obtained from the tangential electric stress, and the corresponding equilibrium shape for a given equation of state was solved numerically. The range of validity of both spheroidal model and the small-deformation model was determined by comparing against experiments [52] and numerical simulations [148], using exactly the same values for physical parameters. For small Ca_E one could always find perfect agreement between small-deformation results and spheroidal results. Between the two models and experiments, the spheroidal model gave better agreement with the experiments over a wider range of Ca_E. Detailed

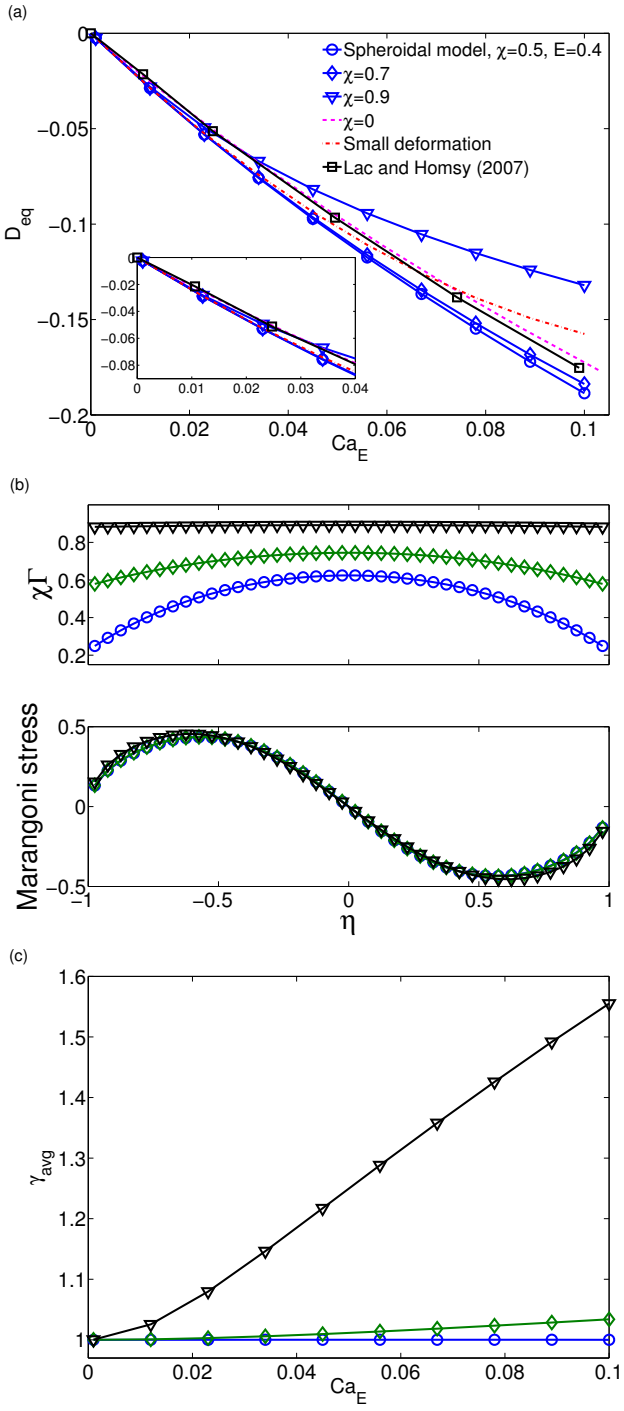

Figure 3.12 Surfactant effects on drop deformation for $(\varepsilon_r, \sigma_r, \mu_r) = (0.05, 0.5, 1)$, where an equilibrium oblate clean drop is found for all values of Ca_E. (a) D_{eq} versus Ca_E at different χ. (b) Surfactant concentration $\chi\Gamma$ (top) and Marangoni stress (bottom). (c) γ_{avg} versus Ca_E.

comparison with numerical simulations for Case A in [148] showed good quantitative agreement in the distribution of surfactant concentration and Marangoni stress.

As non-diffusing surfactant suppressed the fluid flow by immobilizing the interface via the Marangoni stress at equilibrium, adding non-diffusing surfactant eliminated the distinction between prolate A and prolate B drops in terms of fluid flow around the viscous drop. However, one still observed different features of tangential electric stress and surface charge distribution between these two parameter regimes in the presence of surfactant: For parameters in the prolate B clean drop regime, the Marangoni stress, tangential electric stress $S_{\xi\eta}$ and surface charge q are similar to those in the oblate clean drop regime. To the author's knowledge, this has not been reported in the literature.

Furthermore, the spheroidal model captured the surfactant effects at large electric capillary number. In the tip stretching regime the drop deformation was increased by a small amount of surfactant while in the surface dilution regime the drop deformation was decreased by increasing surfactant coverage. More pronounced surface dilution effect were found at large Ca_E. Also investigated was how the existence of an equilibrium spheroidal shape depends on the electric capillary number, elasticity number, and the surfactant coverage. At low surfactant coverage, equilibrium was reached mostly for prolate shape, and increasing the electric capillary number diminished the existence of equilibrium shape. At high surfactant coverage, surface dilution took over and stabilized the equilibrium spheroidal drop at high Ca_E.

CHAPTER 4

ELECTRO-DEFORMATION OF A VESICLE IN AN AC ELECTRIC FIELD

4.1 Introduction

In this chapter, the spheroidal model in [170] is extended to study the equilibrium electro-deformation of a vesicle in AC fields. Unlike the dynamical approach for solving the transmembrane potential in [170], an equilibrium transmembrane potential for a spheroidal dielectric shell in AC fields is developed.

The chapter is organized as follows: In Section 4.3 the problem is formulated. In Section 4.3.1 the equilibrium transmembrane potential for a spheroidal dielectric shell is presented, then the governing equation is derived in Section 4.3.2. The results are summarized in Section 4.4: Initially a comparison between the spheroidal model and the small deformation theory for a prolate vesicle is presented; in Section 4.4.1 the dependence of vesicle deformation, transmembrane potential and electric stresses on the field frequency is considered. In Section 4.4.2, the predictions, as well as comparison with experiment for the shape elongation and transition frequency are discussed.

4.2 Vesicles

Vesicles are closed lipid bilayer membranes that serve as the simplest and minimal models of biological cell membranes. At physiological temperature, lipid membranes are fluid: The lipid molecules are free to move. This fluidity is characterized by the diffusion coefficient, η_s that lie in the range $10^{-9} - 5 \times 10^{-9}$N s m^{-1} [35]. The energy required to bend lipid membrane is comparable to the thermal energy. The bending rigidity, κ characterizes how easy it is to curve the lipid bilayer, and is typically in the order of $20k_BT$, where k_B is the Boltzmann constant and T is the absolute

temperature. Moreover, bilayer membranes respond to external perturbations: Weak tensions smooth out undulations, while high tensions can lead to bilayer stretching and change in the area per lipid molecule. Stretching is characterized by the stretching modulus, K_a, with values in the range $200 - 300\text{mN m}^{-1}$ [122].

Different time scales are involved in the dynamic response of a vesicle in an electric field. Free charges accumulate at the membranes and the vesicles become polarized. The time scale involved in this process is the Maxwell-Wagner time scale, t_{MW}. For a spherical vesicle,

$$t_{MW} = \frac{\varepsilon_{in} + 2\varepsilon_{ex}}{\sigma_{in} + 2\sigma_{ex}}, \tag{4.1}$$

where ε_j and σ_j are the dielectric constants, and conductivities, respectively, of the interior and exterior fluids. Moreover, the lipid bilayer is impermeable to ions and acts as a capacitor that charges on a time scale

$$t_c = r_0 C_m \left(\frac{1}{\sigma_{in}} + \frac{1}{2\sigma_{ex}} \right), \tag{4.2}$$

where r_0 is the radius of the vesicle, and C_m is the membrane capacitance.

The charging time t_c is usually much longer than the Maxwell-Wagner time t_{MW}. Estimates for experiments on vesicles in 1mM NaCl ($\varepsilon_{in} \sim \varepsilon_{ex} = 80\varepsilon_0$, $\sigma_{in} \sim \sigma_{ex} \sim 10$ mS/m, $C_m \sim 0.01$ F/m^2, and $r_0 \sim 10\mu$m) give $t_c \sim 10\mu$s and $t_{MW} \sim 0.01\mu$s. Undertsanding the interplay between these time scales will be key to understanding the dynamic response of vesicles to an AC electric field.

4.3 Problem Formulation

Consider a spheroidal vesicle enclosing an interior dielectric fluid $(\mu_i, \varepsilon_i, \sigma_i)$ suspended in an exterior dielectric fluid with $(\mu_e, \varepsilon_e, \sigma_e)$, see Figure 4.1. μ, ε and σ are the fluid viscosity, dielectric permittivity and conductivity, respectively. The subscript

denotes interior (i) or exterior (e) fluids. In the following subscript 'r' denotes the ratio between interior to exterior quantities.

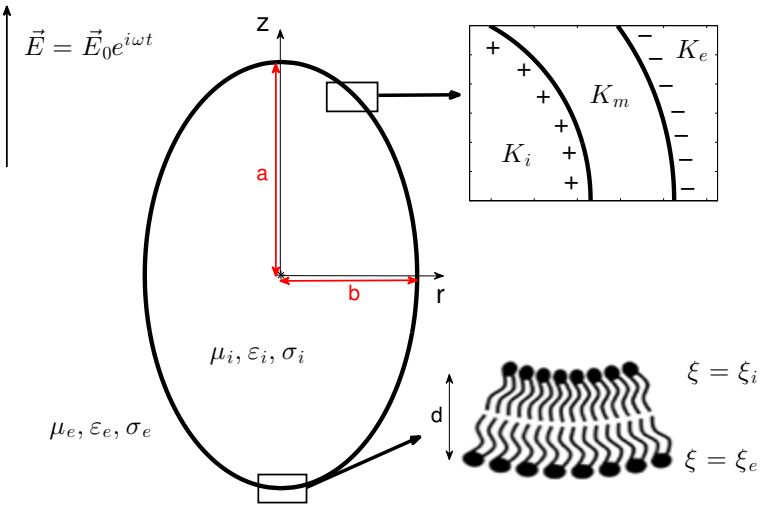

Figure 4.1 Schematic representation of a vesicle suspended in a leaky dielectric fluid.

Typical values of the fluid viscosity (larger than 10^{-3} Pa s) and vesicle size (several μm's) indicate that the fluid inertia are negligible. Consequently, the flow velocity in both interior and exterior fluids is governed by the incompressible Stokes equations (2.23). The stream function inside and outside the vesicle is given by (2.36)-(2.37), where the coefficients A_3^1, A_3^3, B_3^3 and B_3^5 are obtained using the continuity of velocity, kinematic condition $\boldsymbol{u} = \frac{d\boldsymbol{x}}{dt}$, and stress balance on the vesicle membrane, with $\boldsymbol{x}$ denoting the vesicle membrane location. The balance of stresses on the membrane gives

$$\boldsymbol{n} \cdot [\![\mathbf{T} + \mathbf{S}]\!] = \boldsymbol{\tau}^{mem}, \tag{4.3}$$

where $[\![f]\!] \equiv f_e - f_i$ denotes the difference between exterior and interior and $\boldsymbol{n}$ is the outward normal unit vector on the membrane. $\mathbf{T} = -p\mathbf{I} + \mu\left((\nabla \boldsymbol{u})^T + \nabla \boldsymbol{u}\right)$ is the hydrodynamic stress with $\mathbf{I}$ the identity tensor, and $\mathbf{S} = \varepsilon \boldsymbol{E}\boldsymbol{E} - \frac{\varepsilon}{2}(\boldsymbol{E} \cdot \boldsymbol{E})\mathbf{I}$ is the

Maxwell stress. The membrane traction (force density) consists of membrane tension and bending forces,

$$\boldsymbol{\tau}^{mem} = 2\sigma_h H\boldsymbol{n} - \kappa\left(4H^3 - 4KH + 2\nabla_s^2 H\right)\boldsymbol{n}, \tag{4.4}$$

where σ_h, κ, H and K are the membrane tension, bending rigidity, mean curvature and Gaussian curvature, respectively. The (homogenous) membrane tension is related to the excess area $\Delta \equiv \frac{A}{4\pi r_0^2} - 1$ as

$$\sigma_h = s_0 \exp\left[\frac{8\pi\kappa\Delta}{k_B T}\right], \tag{4.5}$$

where $s_0 = \sigma_0/(\kappa/r_0^2)$ is the dimensionless membrane tension.

The electric field is harmonic ($\boldsymbol{E} = \boldsymbol{E}_0 e^{\mathrm{i}\omega t}$) and irrotational, which implies that $\boldsymbol{E} = -\nabla\phi$ with ϕ the electric potential that satisfies (2.17) both inside and outside the vesicle. The potentials inside and outside the vesicle are given by (2.20)-(2.21), where the coefficients β_e and α_i need be computed using the interfacial jump conditions.

At the interface, the electric potential has a jump

$$\phi_i - \phi_e = \Delta\phi, \tag{4.6}$$

due to the capacitive nature of the membrane. The induced charges at the interface cause a discontinuity in the displacement vector

$$[\![\varepsilon\boldsymbol{E}\cdot\mathbf{n}]\!] = Q(\omega, t), \tag{4.7}$$

where Q is the induced charge density. If we neglect the effects of charge convection along the membrane, the electric current conservation at the interface gives

$$[\![\sigma\boldsymbol{E}\cdot\mathbf{n}]\!] = -\frac{dQ}{dt}. \tag{4.8}$$

Substituting (4.7) into (4.8) yields the continuity condition

$$[\![-K\nabla\phi\cdot\mathbf{n}]\!] = 0, \tag{4.9}$$

where the dielectric properties are characterized by the complex conductivity $K_j = \sigma_j + i\omega\varepsilon_j$. σ_j, ε_j and ω are the conductivity, permittivity and electric field frequency, respectively. For the vesicle's membrane, $K_m = G_m d + iC_m d$, where G_m and C_m are the membrane conductance and capacitance.

The governing equations are non-dimensionalized by scaling length to r_0, time to the charging time $t_c = \varepsilon_e/\sigma_e$, the electric potential to $E_0 r_0$, bending force and membrane tension to κ/r_0^2 and electric stresses to $\varepsilon_e E_0^2$. For example, the resultant dimensionless complex conductivities are given by

$$K_e = \frac{1}{x} + i\frac{\omega}{x}, \quad K_i = \frac{\sigma_r}{x} + i\frac{\omega\varepsilon_r}{x}, \quad K_m = \frac{\sigma_m}{\sigma_e x} + i\omega\frac{\varepsilon_m}{\varepsilon_e x} \tag{4.10}$$

where the conductivity and permittivity ratios are defined as $\sigma_r = \frac{\sigma_i}{\sigma_e}$ and $\varepsilon_r = \frac{\varepsilon_i}{\varepsilon_e}$. $x = \frac{d}{r_0}$ is the dimensionless thickness. σ_m and ε_m are the membrane conductivity and permittivity, respectively.

4.3.1 Transmembrane Potential

In the leaky dielectric model the bulk charges neutralize instantaneously, leaving induced charges on the interface between fluids of mismatched dielectric constant. Because the membrane is impermeable, the charges accumulate on either side of the vesicle, inducing a potential. The membrane potential depends on the geometry of the vesicle; even small deviations from an initial shape can induce noticeable changes in the potential. In spite of the evidence, studies of vesicles subjected to AC electric fields [94, 157] often use the transmembrane potential derived for spherical shells [49, 150].

There are relatively few analytical studies [20, 66] on the induced membrane potential for spheroidal vesicles. The main reason is that solving Laplace equations in spheroidal coordinates introduces an unrealistic non-uniform membrane thickness, which results from the alignment of cell boundaries with coordinate surfaces . To

resolve the issue, Klee and Plonsey [73] used numerical simulations, while Gimsa *et al.* [45, 95, 96] devised a resistor-capacitor (RC) approach to determine the induced transmembrane potential. Later, their skepticism proved unfounded as Konik [74] showed that small variations in the membrane thickness of spheroidal cells have no effects on the transmembrane potential.

Herein, a model of the induced transmembrane potential for a spheroidal shell in an AC electric field is developed.

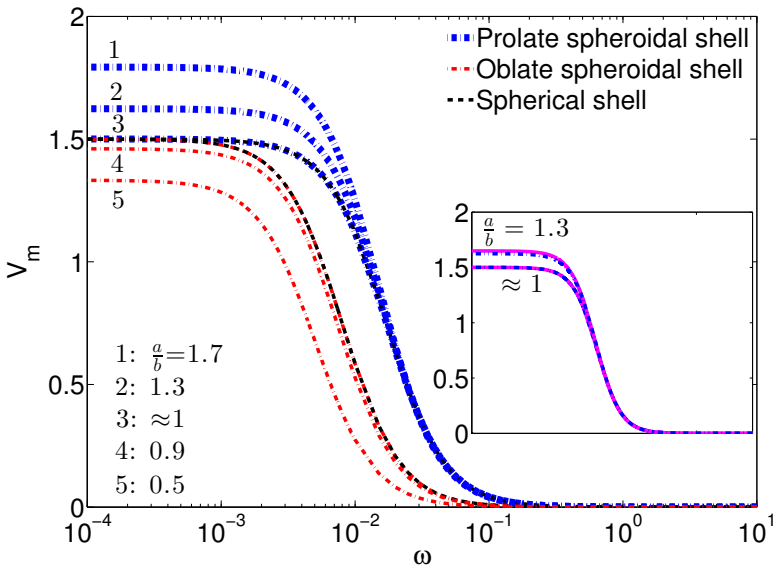

Figure 4.2 Transmembrane potential calculated from Eq. 4.12 for various aspect ratios. The thick (thin) dash-dotted lines are prolate, $\sigma_r = 1.5$ (oblate, $\sigma_r = 0.5$) predictions. The dashed line is the spherical shell potential.

Figure 4.1 shows a sketch of the system. The vesicle consists of three sub-compartments: interior (i), exterior (e), and the membrane (m) (see inset). The transmembrane potential is obtained by solving Laplace equations in all three domains. The potential in each domain takes the truncated form:

$$\phi_j = (\alpha_j \xi + \beta_j Q_1(\xi))\,\eta, \quad j = i, e, m, \tag{4.11}$$

Boundary conditions in the far-field and inside the vesicle immediately yield $\alpha_e = -c$ and $\beta_i = 0$. The remaining coefficients $\beta_e, \alpha_m, \beta_m, \alpha_i$ are determined from boundary conditions at the membrane interfaces (see Appendix E). Substituting the coefficients in (4.11) we get :

$$\Delta\phi = \phi_i(\xi_i) - \phi_e(\xi_e) \equiv V_m\eta, \tag{4.12}$$

where $V_m = cF(\omega)/D(\omega)$ is the 'amplitude' of the potential, $D(\omega)$ is given by (E.7), and

$$\begin{aligned} F(\omega) &= -K_e(Q_1(\xi_e) - \xi_e Q_1'(\xi_e))\left((K_i - K_m)\xi_i Q_1(\xi_e)\right. & (4.13)\\ &\quad \left.+(-K_i\xi_e + K_m\xi_i)Q_1(\xi_i) + K_m(\xi_e - \xi_i)\xi_i Q_1'(\xi_i)\right). & (4.14)\end{aligned}$$

Figure 4.2 provides a comparison of the transmembrane potential magnitude V_m between the spherical and spheroidal models. At low frequencies, the spherical shell potential reaches the maximum value $V_m = 3/2$ while the spheroidal model plateaus to a maximum that depends on the shape aspect ratio: the larger the shape elongation a/b, the larger the maximum transmembrane potential, in agreement with earlier findings about the dependence of the potential on shape [96]. One can note that by solving the Laplace equation in each dielectric spheroidal shell, the η dependence in the spheroidal shell is the same as that in the spherical shell, while Gimsa *et al.*'s model cannot capture the η dependence.

4.3.2 Electrohydrodynamic Deformation

With the transmembrane potential for the spheroidal shell in (4.12), the electric coefficients are calculated as part of the potential solutions in (2.19):

$$\begin{aligned} \phi_e &= \left(-c\xi + \alpha Q_1(\xi)\right)\eta e^{\mathbf{i}\omega t}, & (4.15)\\ \phi_i &= \beta\xi\eta e^{\mathbf{i}\omega t}, & (4.16)\end{aligned}$$

where α and β are obtained by matching the boundary conditions in (4.6) and (4.9):

$$\alpha = \frac{c\xi_o\left(K_r - 1\right) - K_r V_m}{K_r Q_1 - \xi_o Q_1'}, \quad \beta = \frac{c\left(\xi_o Q_1' - Q_1\right) - V_m Q_1'}{K_r Q_1 - \xi_o Q_1'}, \tag{4.17}$$

with $K_r = \frac{K_i}{K_e}$. The electric field $\boldsymbol{E}$ can be written as the real part of $\mathcal{E}$ as $\boldsymbol{E} = \Re(\mathcal{E}) = \frac{1}{2}\left(\mathcal{E} + \mathcal{E}^*\right)$ (where * denotes complex conjugation) and substitute it into the Maxwell stress [159]:

$$\mathbf{S}(\omega) = \frac{\varepsilon}{4}\left(\mathcal{E}\mathcal{E}^* + \mathcal{E}^*\mathcal{E} - |\mathcal{E}|^2\,\mathbf{I}\right) + \frac{\varepsilon}{4}\left(\mathcal{E}\mathcal{E} + \mathcal{E}^*\mathcal{E}^* - \frac{1}{2}\left[\mathcal{E}\cdot\mathcal{E} + \mathcal{E}^*\cdot\mathcal{E}^*\right]\mathbf{I}\right), \tag{4.18}$$

where the first group on the right hand side is the time-averaged Maxwell stress tensor, and the second group is the time-dependent (harmonic) terms. The present work is concerned with only the first group for equilibrium vesicle shapes.

Because the fluid velocity field is axisymmetric, the stream function ψ for both inside and outside the vesicle is given by (2.36)-(2.37). The four coefficients A's and B's, along with the shape function (ξ for prolate or λ for oblate), can be completely determined from the kinematic continuity condition, velocity boundary conditions and the stress balance (4.3) on the membrane. Following the procedures in [170], one projects the stress balance onto the corresponding velocities [22] to close the system:

$$\int_{\xi=\xi_o(t)} u\left[[\![\mathbf{T}_{\xi\eta}]\!] + [\![\mathbf{S}_{\xi\eta}]\!]\right] ds = 0, \tag{4.19}$$

$$\int_{\xi=\xi_o(t)} v\left[[\![\mathbf{T}_{\xi\xi}]\!] + [\![\mathbf{S}_{\xi\xi}]\!] - \tau^{mem}\right] ds = 0. \tag{4.20}$$

In prolate spheroidal coordinates,

$$\mathbf{T}_{\xi\xi} = -p + 2\mu\left(\frac{\partial v}{h_\xi \partial\xi} + \frac{u}{h_\xi h_\eta}\frac{\partial h_\xi}{\partial\eta}\right), \quad \mathbf{T}_{\xi\eta} = \mu\left(\frac{\partial(u/h_\eta)}{\partial\xi}\frac{h_\eta}{h_\xi} + \frac{\partial(v/h_\xi)}{\partial\eta}\frac{h_\xi}{h_\eta}\right), \tag{4.21}$$

$$\mathbf{S}_{\xi\xi} = \frac{\varepsilon}{4}\left(\mathcal{E}_\xi\mathcal{E}_\xi^* - \mathcal{E}_\eta\mathcal{E}_\eta^*\right), \quad \mathbf{S}_{\xi\eta} = \frac{\varepsilon}{4}\left(\mathcal{E}_\xi\mathcal{E}_\eta^* + \mathcal{E}_\eta\mathcal{E}_\xi^*\right), \tag{4.22}$$

where h_ξ and h_η are the scale factors in the spheroidal coordinates, $\mathcal{E}_\xi = -\frac{\partial\phi}{\partial\xi}$ and $\mathcal{E}_\eta = -\frac{\partial\phi}{\partial\eta}$ are the normal and tangential electric field. The excess area in (4.5) can

be expressed in terms of ξ_0 as

$$\Delta = \frac{1}{2}\left(1-\xi_o^{-2}\right)^{-2/3}\left[1-\xi_o^{-2}+\sqrt{\xi_o^2-1}\arcsin\left(\xi_o^{-1}\right)\right]-1. \tag{4.23}$$

The formulation for the oblate case follows in a similar fashion: The oblate spheroidal coordinates (λ,η) is related to the cylindrical coordinates (r,z) as $z=\bar{c}\lambda\eta$, $r=\sqrt{(\lambda^2+1)(1-\eta^2)}$, with $\bar{c}\equiv\sqrt{b^2-a^2}$ for $\lambda\in[0,\infty)$ and $\eta\in[-1,1]$. Surfaces of constant λ are oblate spheroids while surfaces of constant η are hyperboloids. The oblate spheroidal coordinates can be obtained through transforming the prolate spheroidal coordinates: $\xi\to\mathbf{i}\lambda$ and $c\to-\mathbf{i}\bar{c}$ with $\mathbf{i}$ the imaginary unit. For example, the operator

$$E^2=\frac{1}{c^2\left(\lambda^2+\eta^2\right)}\left[(\lambda^2+1)\frac{\partial^2}{\partial\lambda^2}+(1-\eta^2)\frac{\partial^2}{\partial\eta^2}\right],$$

the electric potential coefficients and excess area take the form

$$\alpha=\frac{\bar{c}\lambda_o\left(K_r-1\right)-K_rV_m}{K_rQ_1-\lambda_oQ_1'},\quad \beta=i\frac{\left[\bar{c}Q_1+\left(V_m-c\lambda_o\right)Q_1'\right]}{K_rQ_1-\lambda_oQ_1'}, \tag{4.24}$$

$$\Delta=\frac{1}{2}\left(1+\lambda_o^{-2}\right)^{-2/3}\left[\sqrt{\lambda_o^{-2}+\lambda_o^{-4}}+\tanh^{-1}\left(\left(\lambda_o^2+1\right)^{-1/2}\right)\right]-1. \tag{4.25}$$

If χ designates the generic shape function, with $\chi=\xi_o$ for prolate and $\chi=\lambda_o$ for oblate, then the dimensionless governing equation is

$$\frac{d\chi}{dt}=\frac{\delta\left[\mathcal{Q}_Nf_{21}+\mathcal{Q}_T\frac{f_{11}(\mu_rf_{22}+f_{23})}{\mu_rf_{14}+f_{15}}-Ca_E^{-1}\left(\sigma_hf_{24}+f_\kappa\right)\right]}{\frac{2}{3}\left(\mu_rf_{25}+f_{26}\right)}, \tag{4.26}$$

$$\mathcal{Q}_N=\pm\frac{1}{2c^2}\left[2c^2-2c\tau_3\left(Q_1'+\frac{Q_1}{\chi}\right)+\left(\tau_3^2+\tau_4^2\right)\left(Q_1'^2+\left(Q_1/\chi\right)^2\right)-2\frac{\left(\tau_1^2+\tau_2^2\right)}{\varepsilon_r}\right], \tag{4.27}$$

$$\mathcal{Q}_T=\frac{1}{2c^2}\left[c^2\chi+\left(\tau_3^2+\tau_4^2\right)Q_1Q_1'-c\tau_3\left(Q_1+\chi Q_1'\right)-\left(\tau_1^2+\tau_2^2\right)\chi/\varepsilon_r\right], \tag{4.28}$$

where the symbols $\pm$ designate the prolate $(+)$ or oblate $(-)$. $Ca_E=\frac{\varepsilon_e r_0^3E_0^2}{\kappa}$ is the electric capillary number. $\delta=\frac{t_c}{t_{EHD}}$, where $t_{EHD}=\frac{\mu_i}{\varepsilon_eE_0^2}$ is the timescale

characterizing the electrohydrodynamics flow (EHD). The functions $f_{11} - f_{26}$, f_κ are given by (D.1)-(D.11) for the prolate shape, and (D.13)-(D.23) for the oblate shape. Setting $\frac{d\chi}{dt} = 0$ the steady-state equilibrium shape is obtained by solving the non-linear equation:

$$\mathcal{Q}_N f_{21} + \mathcal{Q}_T \frac{f_{11}\left(\mu_r f_{22} + f_{23}\right)}{\mu_r f_{14} + f_{15}} = Ca_E^{-1}\left(\sigma_h f_{24} + f_\kappa\right). \tag{4.29}$$

Equation (4.29) shows that an equilibrium shape is achieved when the electric forces (on the left) are balanced by the tension and bending forces (on the right).

4.4 Results

4.4.1 Comparison with Small-Deformation Theory

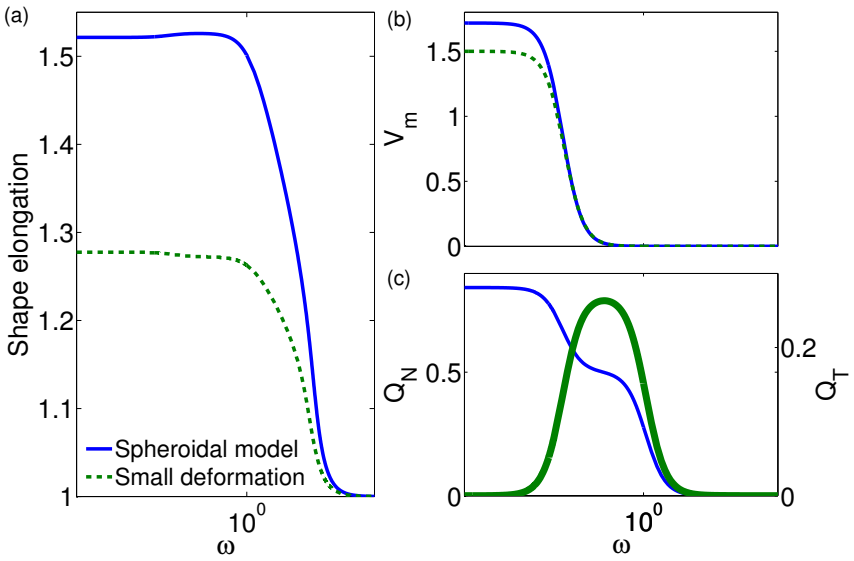

Figure 4.3 Comparison of equilibrium deformation for a prolate vesicle from the spheroidal model (solid curve) and small deformation (dashed curve) for $\sigma_r = 1.5$; $Ca_E = 6837$ and $s_0 = 1$. (a) Equilibrium deformation as a function of frequency ω. (b) Transmembrane potential. (c) Normal (thin curve) and tangential (thick curve) electric stresses from (4.27) and (4.28).

Figure 4.3(a) shows the equilibrium shape elongation from the spheroidal model (solid lines) and the small-deformation theory (dashed lines) [157] for $\sigma_r = 1.5$, $Ca_E =$

6837 and $s_0 = 1$. The shape elongation $a/b = \xi_0/\sqrt{\xi_0^2 - 1}$ for prolate while $a/b = \lambda_0/\sqrt{\lambda_0^2 + 1}$ for oblate. It is found that, for the same membrane tension s_0, the spheroidal model predicts larger deformation than the small deformation theory at a given frequency. The corresponding transmembrane potential magnitude V_m and the electric stresses are shown in figure 4.3(b) and (c). As expected from Section 4.3.1, the membrane potential from the spheroidal model is higher at low frequencies. The decrease in membrane potential at $\omega \approx 5 \times 10^{-3}$ in (b) coincides with an increase in the tangential electric stress, and a decrease in the electric pressure in (c).

4.4.2 Comparison with Experiment

The equilibrium vesicle shape is spherical at high frequencies when the transmembrane potential vanishes. At low frequency ($\omega < 10^2$) experiments show that the equilibrium vesicle shape can be prolate if $\sigma_r > 1$ or oblate if $\sigma_r < 1$. In particular, the equilibrium oblate vesicle for $\sigma_r < 1$ crosses over to the prolate equilibrium shape for even smaller frequency $\omega < 10^{-2}$. These experimental findings [6] are summarized (symbols) in Figure 4.4 and Figure 4.5, where the comparison between the spheroidal model (solid lines) and the small-deformation model [157] (broken lines) is also shown. Following the approach in [157] s_0 is used as a fitting parameter (see Table 4.1) and fix the bending stiffness $\kappa = 10 k_B T$. s_0 used in the spheroidal model is at least an order of magnitude larger than in small deformation. Nevertheless, they are comparable to values reported in previous work [76].

Figure 4.4(a) is for $\sigma_r > 1$ ('transition' *(1)* in [6]) where the equilibrium vesicle shape elongation is always greater (prolate) or equal (spherical) to one. There is better agreement from the spheroidal model for $\sigma_r = 1.7$, while for $\sigma_r = 4.3$ the spheroidal results are in better agreement except for $\omega > 10$. Figure 4.4(b) is for $\sigma_r < 1$ ('transition' *(4)* in [6]) where the equilibrium vesicle shape can cross over from spherical at high frequencies $\omega > 20$ to oblate at intermediate frequencies $\sim$

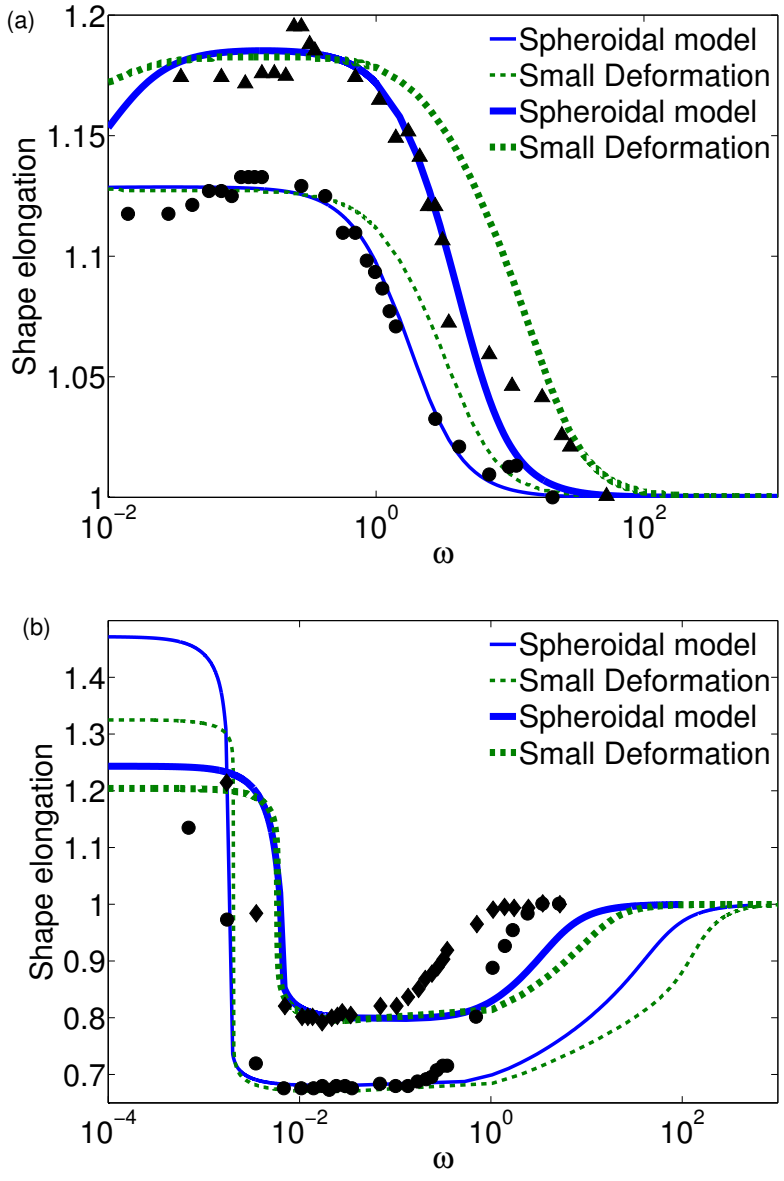

Figure 4.4 Comparison between the experimental data of Aranda *et al.* [6] (symbols), the small deformation theory (dashed curves), and the current model (solid curves). (a) $\sigma_r > 1$; (b) $\sigma_r < 1$.

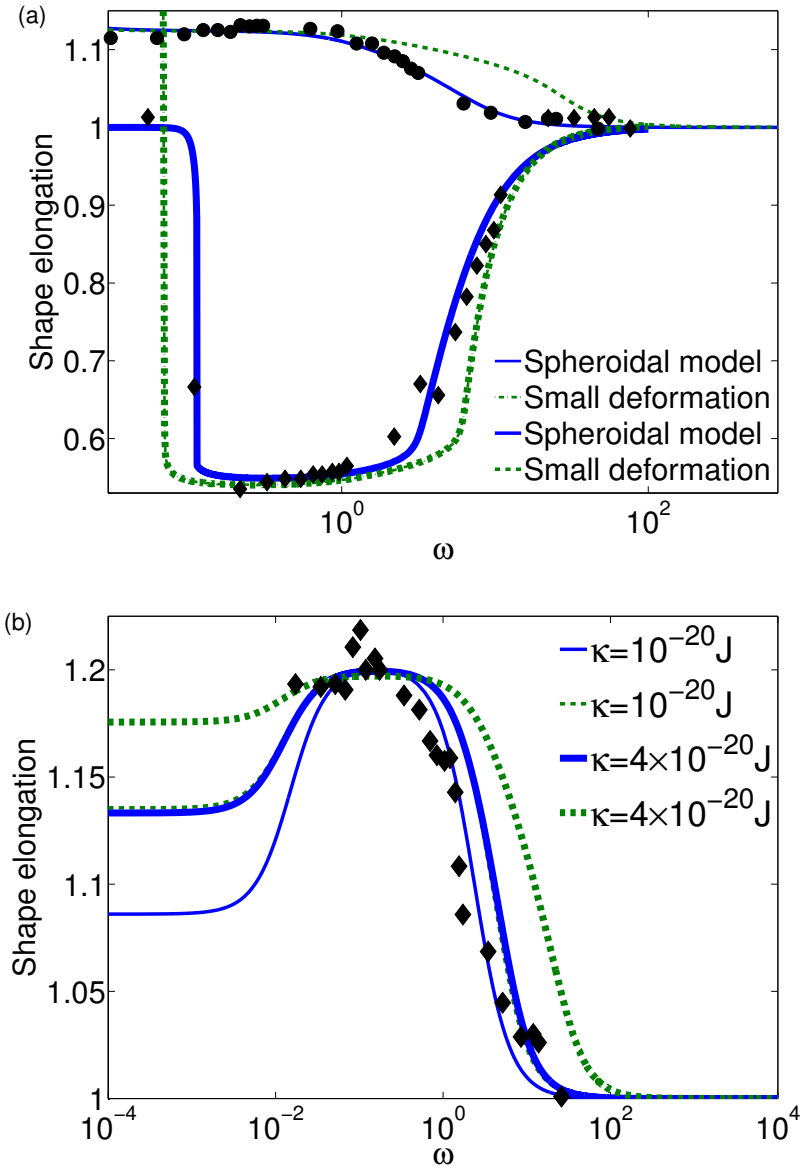

Figure 4.5 (a) Comparison between the experimental data (symbols) of Aranda *et al.* [6], small deformation theory (dashed curves), and the current model (solid curve). The conductivity ratio $\sigma_r \approx 1$. (b) Comparison between the experimental data of Aranda *et al.* [6] (symbols), small deformation theory (dashed curves), and the current model (solid curves). The conductivity ratio, $\sigma_r = 4.5$.

Table 4.1 Fitted Values of $s_0 = \bar{\sigma}_0 r_0^2/\kappa$ for the Experimental Data in [6] with $\varepsilon_r = 1$, $\mu_r = 1$, $\kappa = 10 k_B T$, and $E_0 = 0.2$kV/cm

Experiment	s_0 used in spheroidal model	s_0 used in small-deformation model
$\sigma_r = 4.3$, $r_0 = 21.6\mu$m	43 000	3000
$\sigma_r = 1.7$, $r_0 = 27.5\mu$m	80 000	20 000
$\sigma_r \approx 1$ (Pr), $r_0 = 27.5\mu$m	1000	1
$\sigma_r \approx 1$ (Ob), $r_0 = 37.5\mu$m	10^{-6}	10^{-7}
$\sigma_r = 0.5$, $r_0 = 12.8\mu$m	1000	100
$\sigma_r = 0.4$, $r_0 = 27.2\mu$m	70	1

$3 \times 10^{-3} \leq \omega \leq\sim 1$, and to prolate at low frequencies $10^{-4} \leq \omega \leq\sim 3 \times 10^{-3}$. In this case neither model agrees with the experiments for $1 > \omega > 0.5$, where the equilibrium vesicle shape crosses over from oblate to spherical as ω increases.

In 'transition' *(3)* of [6] where σ_r is close to unity, the value of σ_r determines the shape of the vesicles: Prolate for $\sigma_r > 1$ and oblate for $\sigma_r < 1$. Figure 4.5(a) shows the comparison between models and experiments for $\sigma_r \approx 1$.

The effect of bending rigidity on the equilibrium vesicle shape is investigated next. For experiments in [6], the bending stiffness varies between 4×10^{-20} J [76] and 2.3×10^{-19} J [136]. In addition, recent measurements on SOPC bilayer membranes yielded a bending stiffness as low as 7×10^{-21} J [118]. Figure 4.5(b) shows a comparison between theories and experiments for $\sigma_r = 4.5$ and with various values of the bending stiffness. Both theories are very sensitive to changes in the bending stiffness: There is good agreement with experiments up to $\kappa = 4 \times 10^{-20}$ J for the spheroidal model, and

up to $\kappa = 10^{-20}$ J for the small deformation. Beyond these values, the two models overestimate the deformation.

Vesicles morph into various shapes at different frequencies and conductivity ratios. To elucidate the extent and range of these variations, Aranda *et al.* [6] constructed a morphological diagram: They performed a series of experiments using over 60 vesicles ranging $4 - 50\mu$m in size. Fixing the conductivity inside the vesicles and varying the conductivity of the external phase, the authors then subjected the vesicles to an AC field of frequencies ranging between ≈ 2 kHz $- 20$ MHz.

Figure 4.6 shows the shape variations in the $\sigma_r - \omega$ plane. The experimental data points indicate the value at which the vesicle changes shape as frequency increases. Figure 4.6 also compares the predictions from the spheroidal model, the theory based on small deformation, and the result using the energy minimization approach [116]. The spheroidal and small deformation models give agreements with experiments: The prolate-to-oblate and prolate-to-sphere frequencies increase with σ_r, while the oblate-to-sphere frequencies decrease with increasing σ_r. The model in [116] only shows qualitative agreements.

The frequency at which the equilibrium vesicle shape crosses over from prolate to oblate depends on the conductivity ratio and vesicles size [5, 6, 104, 116, 117]. In a recent experiment Peterlin [116] put vesicles of different sizes under a sequence of step-wise frequency changes, ranging from hundreds to a thousand hertz for a duration of ≈ 3 secs with the frequency increasing or decreasing around the crossover frequency, see the symbols in figure 4.7(a).

At the crossover frequency (from prolate to oblate, for example), the equilibrium vesicle shape is spherical, which corresponds to the limit $\xi \to \infty$, $\Delta \approx 0$, and V_m reduces to spherical shell potential. An asymptotic analysis is performed on the equilibrium vesicle shape elongation near the crossover frequency, where all functions of ξ are expanded in terms of $1/\epsilon^2$. For example, the Legendre polynomial $Q_1(\xi)$

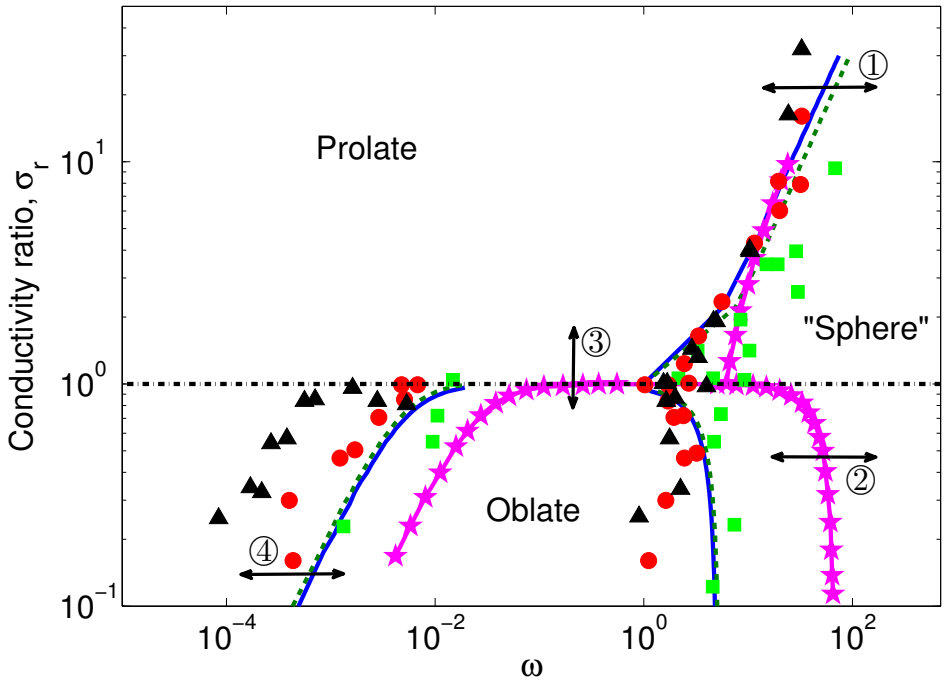

Figure 4.6 Morphological phase diagram. The fitted membrane tension is $s_0 = 45000$ for the spheroidal (solid line), and $s_0 = 10000$ for the small deformation (dashed line) models. The prediction from the energy minimization approach [116] is also shown. Filled symbols are experimental data [6]; the conductivity ratio, σ_r is determined by varying the conductivity of the external medium (σ_e) and holding the interior fixed at $\sigma_i = 15\mu$S/cm (□), 65μS/cm (◯), 130μS/cm (△). Other parameters are: $\kappa = 10k_BT$, $E_0 = 2 \times 10^4$ V/m.

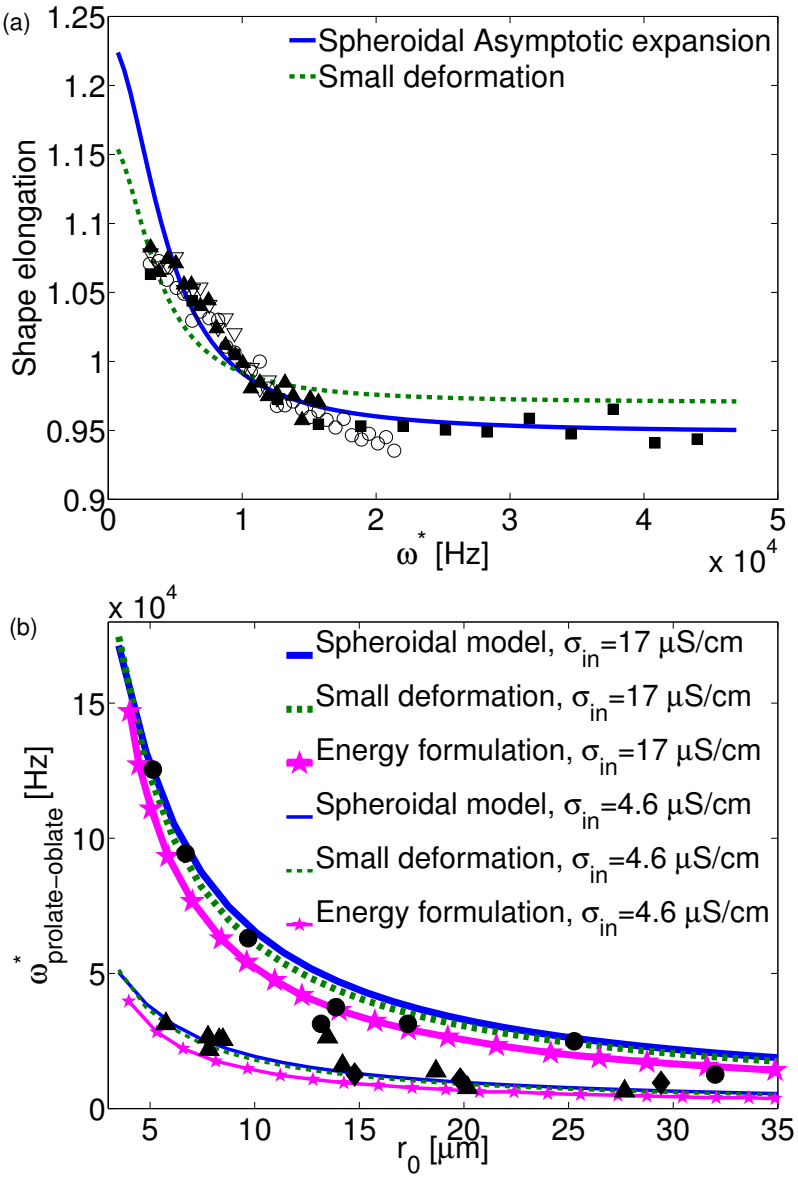

Figure 4.7 (a) Shape elongation as a function of dimensional frequency, ω^*. The conductivity ratio, $\sigma_r = 0.9$, and $s_0 = 1$ for all theoretical results. The symbols represent the experimental data in [116]. Full (open) symbols represent experiments with increasing and decreasing frequency changes as a check for hysteresis. Other physical parameters are $d = 4$ nm, $\kappa = 1.2 \times 10^{-19}$ J, $E_0 = 500$ V/m. (b) Prolate-oblate crossover frequency, ω^* as a function of vesicle radius, r_0.

and its derivative take the form $Q_1 \sim \frac{1}{3\xi^2} + \frac{1}{5\xi^4} + \mathcal{O}\left(\frac{1}{\xi^6}\right)$, $Q_1' \sim -\frac{2}{3\xi^3} - \frac{4}{5\xi^5} + \mathcal{O}\left(\frac{1}{\xi^7}\right)$. The semi-focal length $c \sim \frac{1}{\xi} + \mathcal{O}\left(\frac{1}{\xi^3}\right)$, and similarly for all the other functions in Appendix D. Substituting these expansions in (4.17), (4.27)-(4.29), leads to an expansion $\sum_{n=0} a_n \xi_0^{-2n} = 0$, where the coefficients a_n are functions of fluid and membrane properties. Keeping all the leading-order terms at $\mathcal{O}(1/\xi_0^2)$ one obtains an equation for ξ_0^2, which gives the solution

$$\xi_0(\omega) = \sqrt{\frac{2}{35}} \frac{\sqrt{-Ca_E ABC}}{G} \tag{4.30}$$

where coefficients A, B, C and G are given in Appendix G.

The leading-order shape elongation for a prolate vesicle near the crossover frequency is $\frac{a}{b} \sim 1 + \frac{1}{2\xi_0^2} + \mathcal{O}\left(\frac{1}{\xi_0^4}\right)$. Similarly for the crossover from oblate to prolate, the leading order shape elongation would be $\frac{a}{b} \sim 1 - \frac{1}{2\lambda_0^2} + \mathcal{O}\left(\frac{1}{\lambda_0^4}\right)$.

Figure 4.7(a) shows the comparison between the asymptotic analysis on the spheroidal model (solid line), calculation from the small deformation model (dashed line) and experiments (symbols). First, one can observe a small difference in the crossover frequency (value of ω^* when shape elongation is unity) between the solid and the dashed lines: This small difference is attributed to the different treatment of the stress balance on the membrane. Second, one can observe a significant difference in the slope at the crossover frequency between the two curves, with the spheroidal model in better agreement with the experimental data. Attempts to adjust s_0 to fit the small-deformation model to experimental data with the same slope at the crossover frequency have proven unsuccessful. The crossover frequency also depends on the initial spherical size of vesicles. Figure 4.7(b) shows the comparison results of the experiment in [116], where the spheroidal results (solid curves), the small-deformation results (dashed curves) and the energy-minimization results (starred solid curves)

are all plotted against the initial spherical radius r_0. All three theories show good agreement with the experimental data.

4.5 Conclusion

In this chapter, a spheroidal model was developed to study the equilibrium deformation of a vesicle in AC electric fields within the leaky dielectric framework. Such an approach has been shown to capture large equilibrium electro-deformation of a viscous surfactant-covered drop [109] and the transient dynamics of a vesicle in a DC field [170]. In the spheroidal model, the vesicle membrane was modeled as a non-conducting capacitive elastic membrane with a homogeneous tension that depends on the excess area. A spheroidal shell model was constructed to compute the potential across the vesicle membrane. By adjusting the membrane tension coefficient s_0, good agreement was found with the experiments in terms of the dependence of the vesicle shape elongation on the frequency ω, conductivity ratio σ_r, and the initial spherical radius of the vesicle. The effects of bending rigidity on the shape elongation were also explored. Furthermore, an asymptotic analysis on the spheroidal model around the prolate-oblate crossover frequency was conducted, and very good agreement with the experiments was found in terms of both the value of crossover frequency and the rate of change of shape elongation with respect to frequency.

This work did not consider effects of membrane conductance, which is found to destabilize a planar membrane under electric fields [133, 135]. The focus was on the equilibrium deformation and the time-dependent harmonic stresses were ignored. Consequently, the dynamic transient and oscillation around the averaged equilibria was not considered, yet the spheroidal model can easily incorporate the time-dependent stresses and this is now part of an ongoing work. In addition the vesicle area was not held constant in the model. Furthermore, the spheroidal model is applicable only to

spheroidal deformation, and cannot describe the dynamics and equilibrium shapes of an axisymmetric non-spheroidal vesicle.

CHAPTER 5

NUMERICAL SIMULATIONS OF A VISCOUS DROP

5.1 Introduction

Numerical studies have bee conducted to investigate the effects of electric fields on the dynamics of a single viscous drop [37, 43, 77, 119, 142], particle-particle interactions [11, 58], and various other systems [148], just to name a few. These studies can be classified based on the representation of the immersed boundary [13, 44, 62, 91, 92, 165, 168].

The immersed boundary method, originally developed by Peskin [114] to study blood flow through a beating heart, has recently been extended to investigate drop dynamic under an electric field. In the immersed boundary the equations governing the fluids are solved in a fixed Cartesian grid, and the drop is represented by Lagrangian markers, at which boundary forces are computed. The forces are then interpolated between the Eulerian grid and the Lagrangian markers using smoothed delta functions. However, regularizing the singular force leads to a method that is only first order. The immersed interface method of Leveque and Li [82] offers a more accurate method. The idea is to capture the jump conditions at the interface in a sharp manner, where the jumps are incorporated into a new finite difference scheme.

In this chapter, a numerical code based on the immersed interface method is developed to simulate the transient electro-deformation of an axisymmetric drop. Unlike previous works, the electric force is only defined at the boundary in such a way that applying the divergence operator to the Maxwell stress tensor is avoided altogether. This approach was only recently used in [11, 61]. The major differences between the present work and [61] is threefold: First, the present system is three-dimensional. Second, the one-sided interpolation in the present study is second-order. Third, the fluid equations are solved using a second-order method, resulting in

solutions with higher resolution than is generally achieved by the immersed boundary method.

This chapter is organized as follows: The governing equations are presented in Section 5.2. The numerical methods are described in Section 5.3: The immersed interface method to solve the the electric potential in axisymmetric coordinates is developed in Section 5.3.1, and the implementation of the immersed interface method for the flow field presented in Section 5.3.2. Finally, the convergence analysis and comparison against the spheroidal model of Chapter 1 are discussed in Section 5.4.

5.2 Governing Equations

The problem of an initially spherical viscous drop immersed in a fluid in a DC electric field, $\boldsymbol{E}_0$ in three-dimensional axisymmetric coordinates is considered. The equations governing the system consists of the incompressible Stokes equations with surface tension and electric force. The bulk fluid and the drop have different permittivity (ε^j) and conductivity (σ^j), where the superscript j denotes the bulk ($+$) and the interior of the drop ($-$), respectively. The drop interface Γ is given in parametric form $\mathbf{X}(s,t) = (R(s,t), Z(s,t))$ with $0 \leq s \leq 2\pi$. The ratios of permittivities and conductivities are defined as

$$\varepsilon_r = \frac{\varepsilon^-}{\varepsilon^+},\ \sigma_r = \frac{\sigma^+}{\sigma^-}. \tag{5.1}$$

In the *leaky dielectric* framework, bulk charges neutralize instantaneously, and the conservation of free charge density reduces to the Laplace equation governing the electric potential, ϕ:

$$\nabla \cdot (\varepsilon \nabla \phi) = 0, \tag{5.2}$$

with interface conditions

$$[\![\phi]\!] = 0, \qquad [\![\sigma \nabla \phi \cdot \boldsymbol{n}]\!] = \frac{dq_s}{dt} \tag{5.3}$$

at the drop interface. $\boldsymbol{n}$ is the unit outward normal, $q_s = [\![\varepsilon \nabla\phi \cdot \boldsymbol{n}]\!]$ represents the surface charge density, and $[\![\cdot]\!]$ denotes the jump between outside and inside quantities. The charging time scale, t_c is much faster than the time scale t_{EHD} of the electrohydrodyanimc flow. Consequently, and omitting charge convection, the jump condition on the normal electric field reduces to $[\![\sigma \nabla\phi \cdot \boldsymbol{n}]\!] = 0$. In the far-field, the electric potential satisfies $\nabla\phi^+ = -\boldsymbol{E}_0\hat{\boldsymbol{z}}$.

The stress induced in the dielectric medium is the result of the Maxwell stress tensor,

$$\mathbf{M} = \varepsilon \left(\boldsymbol{E}\boldsymbol{E} - \frac{1}{2}E^2\mathbf{I} \right), \tag{5.4}$$

where $\mathbf{I}$ is the identity tensor. Because the electric properties of the bulk and drop are piecewise constants, it is evident that the electric force $\boldsymbol{F}_E = \nabla \cdot \mathbf{M}$ affects the flow only near the drop interface. Therefore, the electric effects can be treated as an interfacial force given by the jump in Maxwell stress in the normal direction, as done in the boundary integral method [99]. The interfacial electric force is

$$\boldsymbol{f}_E = [\![\mathbf{M} \cdot \boldsymbol{n}]\!], \tag{5.5}$$

where $\boldsymbol{n}$ is the unit outward normal, and the electric body force

$$\boldsymbol{F}_E = \int \boldsymbol{f}_E(s,t)\delta(\boldsymbol{x} - \boldsymbol{X}(s,t))ds, \tag{5.6}$$

where the axisymmetric coordinates $\boldsymbol{x} = (r, z)$.

The flow field is governed by the incompressible Navier-Stokes equation,

$$\frac{\partial \boldsymbol{u}}{\partial t} + \boldsymbol{u} \cdot \nabla \boldsymbol{u} = -\nabla p + \mu \nabla^2 \boldsymbol{u} + \boldsymbol{F}, \tag{5.7}$$

$$\nabla \cdot \boldsymbol{u} = 0, \tag{5.8}$$

$$\tag{5.9}$$

where

$$\boldsymbol{F} = \int_0^{2\pi} \boldsymbol{f}(s,t)\delta^2\left(\boldsymbol{x} - \boldsymbol{X}(s,t)\right) ds.$$

The singularly supported force $\boldsymbol{f}$ consists of the surface tension [41, 79] and electric force, and is defined by

$$\boldsymbol{f} = \boldsymbol{f}_\gamma + \boldsymbol{f}_E = \gamma\left(\frac{R_s Z_{ss} - R_{ss} Z_s}{|\boldsymbol{X}_s|^3} + \frac{Z_s}{R}\right)\boldsymbol{n} + [\![\mathbf{M}\cdot\boldsymbol{n}]\!], \tag{5.10}$$

where $|\boldsymbol{X}_s| = \sqrt{R_s^2 + Z_s^2}$, and the subscript denotes partial derivatives with respect to s.

5.3 Numerical Methods

Let Δt be the time step and $t_n = n\Delta t$ the nth time-level with $n = 0, 1, 2, \ldots$. The set of Lagrangian markers $\mathbf{X} = (R_k^n, Z_k^n)$ for $k = 0, 1, 2, \ldots, N_B$ represents the position of the drop at time t_n. Assuming that the drop is a simple closed curve, $(R_0^n, Z_0^n) = (R_{N_B}^n, Z_{N_B}^n)$. The drop is immersed in the domain $\Omega = [-L, L] \times [-L, L]$, discretized as $r_i = ih$ and $z_j = jh$ along the r- and z-axis, respectively, with $i, j = -N, -N+1, \ldots, 0, \ldots, N-1, N$ and the mesh width $h = L/N$.

In cylindrical coordinates, the solutions are obtained in the half-plane $r \geq 0$, and solutions in the left half-plane $r < 0$ are obtained by symmetry thereafter. Figure 5.1 shows the computational domain, along with boundary conditions. For the electric potential, Dirichlet boundary conditions are imposed at the capacitor plates,

$$\phi^+ = -E\frac{L}{2} \text{ on } z = L \quad \text{and} \quad \phi^+ = E\frac{L}{2} \text{ on } z = -L. \tag{5.11}$$

In addition, Neumann boundary condition for the electric field is applied along the axis of symmetry and the rightmost boundary,

$$\nabla\phi \cdot \boldsymbol{n} = 0 \text{ on } r = 0 \text{ and } r = L. \tag{5.12}$$

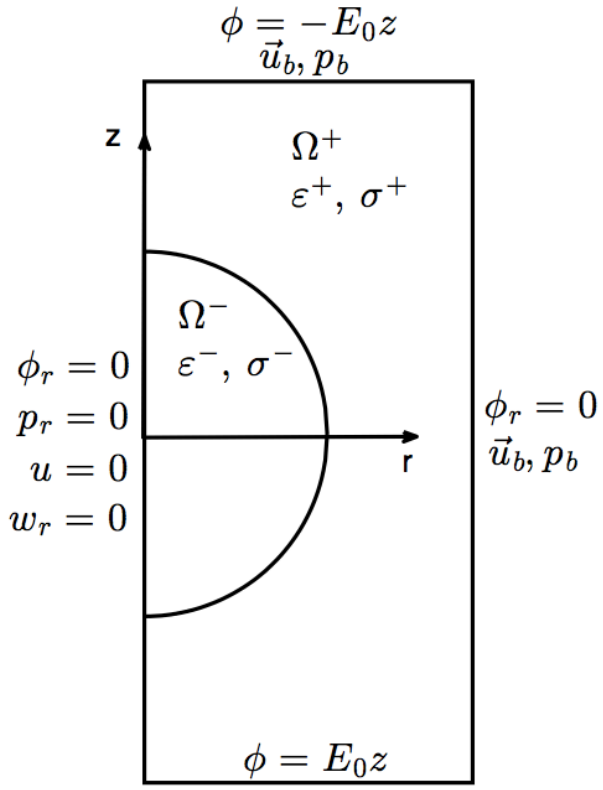

$$\vec{u}_b = \int\int (1/8\pi\mu)(\delta_{ij}/r + x_i x_j / r^3) f_j dS(x)$$
$$p_b = \int\int -(1/4\pi)\vec{f} \cdot \nabla(1/r) dS$$

Figure 5.1 The computational domain and imposed boundary conditions.

For the flow field, Neumann boundary conditions for pressure and velocity are applied in the z-direction,

$$\frac{\partial p}{\partial r} = 0, \qquad \frac{\partial w}{\partial r} = 0 \ \text{ at } \ r = 0, \tag{5.13}$$

and

$$u = 0 \ \text{ at } \ r = 0, \tag{5.14}$$

in the r-direction. The other three sides of the domain have Dirichlet boundary conditions for p, u, and w determined from boundary integrals,

$$p = \int\int -\frac{1}{4\pi} \boldsymbol{f} \cdot \nabla \left(\frac{1}{r}\right) dS, \tag{5.15}$$

$$\boldsymbol{u} = \int\int \frac{1}{8\pi\mu} \left(\frac{\delta_{ij}}{r} + \frac{x_i' x_j'}{r^3}\right) f_j dS(x'). \tag{5.16}$$

In the immersed interface method, grid points are classified as *regular* or *irregular* based on their proximity to the interface. A point (i, j) is *irregular* if its stencil consists of neighbors on either side of the interface, while a *regular* grid point has its four neighbors on the same side of the interface (see Figure 5.2).

5.3.1 Electric Potential and Fields

The elliptic equation (5.2) governing the electric potential is solved by extending the immersed interface method [82] to three-dimensional axisymmetric coordinates. At *regular* grid points, the equation is discretized using the standard five-point, second-order finite difference scheme,

$$\left(1 + \frac{h}{2r_i}\right) \phi_{i+1,j} + \left(1 - \frac{h}{2r_i}\right) \phi_{i-1,j} + \phi_{i,j+1} + \phi_{i,j-1} - 4\phi_{i,j} = 0, \tag{5.17}$$

where $\phi_{i,j} = \phi(r_i, z_j)$ and C_{ij} is a correction term resulting from the jump discontinuities across the interface. For irregular grid points, a new finite difference scheme that incorporates the jump conditions at the interface needs to be derived. The scheme

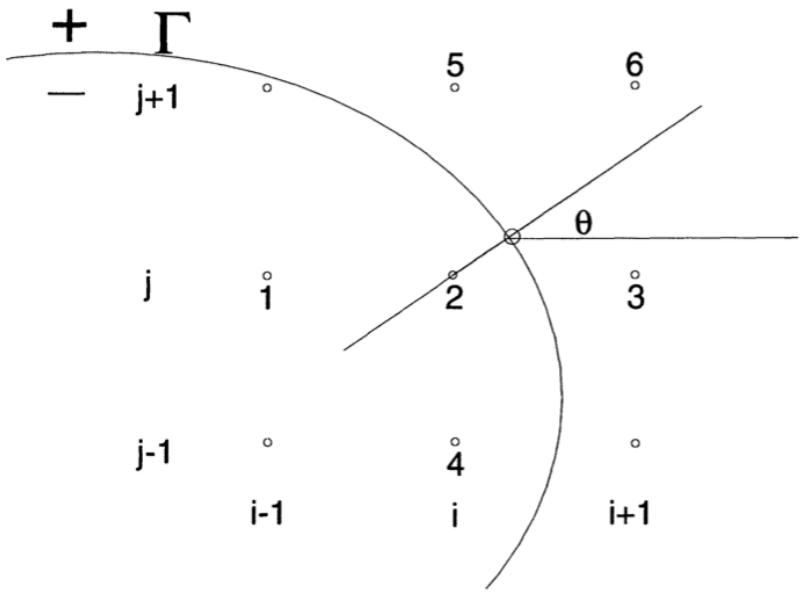

Figure 5.2 The geometry at an irregular grid point (i, j), from [82].

takes the form

$$\sum_k \gamma_k \phi_{i+i_k, j+j_k} = C_{ij}, \tag{5.18}$$

where coefficients γ_k, and the correction term C_{ij} needs to de determined. Because the interface conditions in (5.3) are homogeneous, the correction term $C_{ij} = 0$, and the jump in conductivities across the drop surface is accounted for in the coefficients γ_k in (5.18).

Computing the coefficients γ_k consists of the following steps:

- Select a point $(r^*, z^*) \in \Gamma$.
- Apply a local coordinate transformation in directions normal and tangential to the interface at point (r^*, z^*).
- Derive the jump conditions relating $(+)$ and $(-)$ values in the local coordinates.
- Choose an additional point to form a six-point stencil.

- Solve a linear system of equations for γ_k.

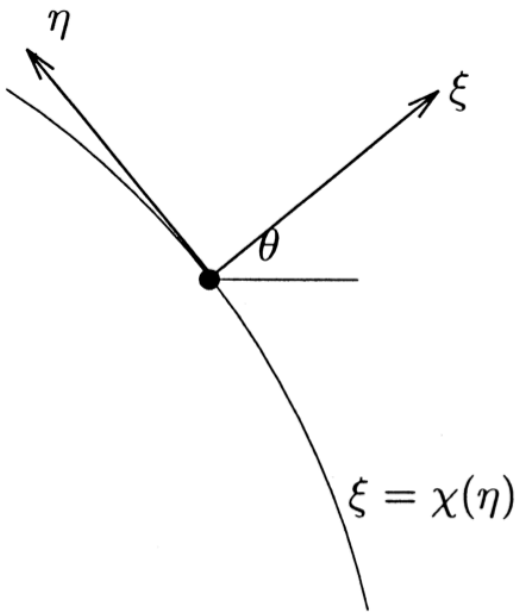

Figure 5.3 Local coordinates at the fluids interface.

The local coordinate transformation (see Figure 5.3) is

$$\xi = (r - r^*)\cos\theta + (z - z^*)\sin\theta, \tag{5.19}$$

$$\eta = -(r - r^*)\sin\theta + (z - z^*)\cos\theta, \tag{5.20}$$

where θ is the angle between the r-axis and the normal direction, pointing outward to the (+) side. In the neighborhood of (r^*, z^*), the interface lies in the η-direction, and thus is parameterized by $\xi = \chi(\eta)$. Note that $\chi(0) = 0$ and $\chi'(0) = 0$, provided the boundary is smooth. The interface conditions are derived based on the new coordinates, and after expanding the potential on either side of the interface about (r^*, z^*), one obtains a linear system of equations for the γ_k (see Appendix H).

Provided a solution exists, the system

$$a_1 + a_2 = 0, \tag{5.21}$$

$$a_3 + \rho a_4 + (a_{10} - a_8)(1-\rho)\chi'' = \sigma^- \frac{\cos\theta}{r}, \tag{5.22}$$

$$a_5 + a_6 + a_{12}(1-\rho)\chi'' + a_8(1-\rho)\frac{\sin\theta}{r} = -\sigma^- \frac{\sin\theta}{r}, \tag{5.23}$$

$$a_7 + \rho a_8 = \sigma^-, \tag{5.24}$$

$$a_9 + a_{10} + a_8(\rho - 1) = \sigma^-, \tag{5.25}$$

$$a_{11} + \rho a_{12} = 0, \tag{5.26}$$

gives the coefficients γ_k of the finite difference scheme at *irregular* grid points. The a_k's are defined as

$$\begin{aligned}
a_1 &= \sum_{\vec{x}\in\Omega^-} \gamma_{ij}, \quad a_2 = \sum_{\vec{x}\in\Omega^+} \gamma_{ij} \\
a_3 &= \sum_{\vec{x}\in\Omega^-} \gamma_{ij}\xi_i, \quad a_4 = \sum_{\vec{x}\in\Omega^+} \gamma_{ij}\xi_i \\
a_5 &= \sum_{\vec{x}\in\Omega^-} \gamma_{ij}\eta_j, \quad a_6 = \sum_{\vec{x}\in\Omega^+} \gamma_{ij}\eta_j \\
a_7 &= \sum_{\vec{x}\in\Omega^-} \gamma_{ij}\frac{\xi_i^2}{2}, \quad a_8 = \sum_{\vec{x}\in\Omega^+} \gamma_{ij}\frac{\xi_i^2}{2} \\
a_9 &= \sum_{\vec{x}\in\Omega^-} \gamma_{ij}\frac{\eta_j^2}{2}, \quad a_{10} = \sum_{\vec{x}\in\Omega^+} \gamma_{ij}\frac{\eta_j^2}{2} \\
a_{11} &= \sum_{\vec{x}\in\Omega^-} \gamma_{ij}\xi_i\eta_j, \quad a_{12} = \sum_{\vec{x}\in\Omega^+} \gamma_{ij}\xi_i\eta_j.
\end{aligned}$$

The discretization of (5.2) at all grid points form a linear system of equations,

$$\Delta_h \phi^n = g^n, \tag{5.27}$$

whose solution is the electric potential ϕ^n at the current time t_n; g^n is a vector that includes the boundary condition. Equation (5.27) is solved using the Generalized Minimal RESidual (GMRES) implementation from the NETLIB repository. As a stand-alone method, convergence can be slow depending on the structure and size of

Δ_h. Preconditioning the system is needed to achieve faster convergence. In this work, Successive Over-Relaxation (SOR) is used as the preconditioner to GMRES [31, 32, 33, 68, 125, 126]. Instead of (5.27), one solves the (left) preconditioned system

$$M^{-1}\Delta_h\phi^n = M^{-1}g^n, \tag{5.28}$$

where M is a full matrix, obtained from a few iterations, k_p of SOR.

GMRES with SOR-preconditioner is referred as SOR(k_p)-GMRES [32, 33], and it has been used successfully to solve the sea-ice momentum equation [81]. Note that the number of SOR iterations, k_p, is distinct from the number of GMRES iterations. Moreover, GMRES and SOR are matrix-free methods: They do not require the explicit knowledge of the coefficient matrix, and only need the result of a matrix-vector operation. This is a considerable advantage in terms of computational cost and memory, especially when the grid number N becomes large (> 100).

The rate of convergence of SOR, and therefore of SOR-GMRES, depends on the relaxation parameter ω. For faster convergence, $1 < \omega < 2$. Figure 5.4(a) shows the number of iterations to converge with a tolerance of 10^{-10} for the SOR-GMRES and SOR methods as a function of the relaxation parameter, ω. In Figure 5.4(b), the corresponding time it took to achieve the aforementioned tolerance is shown, again as a function of ω. The solid (SOR-GMRES) and dashed (SOR) curves represent different values of the grid number, $N = 64,\ 128,\ 256$. Also, note that the optimal ω is not necessary the same in both methods. When $N = 128$, SOR-GMRES produced converging solutions up to $\omega = 1.65$, while SOR failed to converge for $\omega \geq 1.6$.

Once the potential is known at every grid point, the jump in the maxwell stress at the interface can be computed. One-sided least square interpolation [87, 158] is used to calculate the interfacial potential and electrostatic field. A system of $m(\geq 6)$

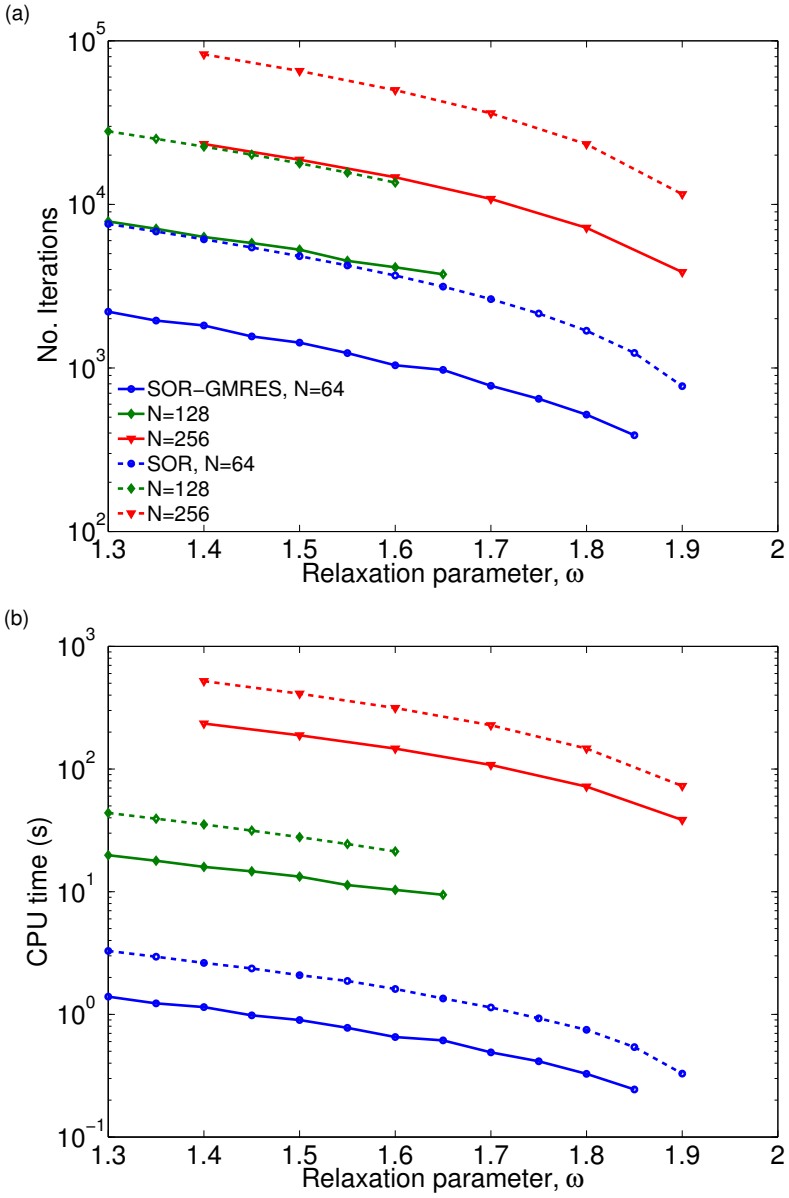

Figure 5.4 Number of iterations (a) and time to convergence (b) for SOR-GMRES (solid) and SOR (dashed) as a function of the relaxation parameter, ω.

equations is derived from the second-order Taylor expansion near the interface

$$\begin{aligned}\phi(r,z)_m =& A_1 + A_2(r-R_k)_m + A_3(z-Z_k)_m + A_4(r-R_k)_m^2 + A_5(z-Z_k)_m^2 \\ &+ A_6(r-R_k)_m(z-Z_k)_m,\end{aligned} \tag{5.29}$$

from the $m(\geq 6)$ grid points used for the extrapolation. The over-determined problem is re-written in matrix form,

$$\zeta \boldsymbol{A} = \boldsymbol{Y}, \tag{5.30}$$

where $\boldsymbol{A} = [A_1, A_2, \ldots, A_6]^T$, $\boldsymbol{Y} = \phi(r,z)_l$, and ζ is the coefficient matrix of relative distances.

Least square minimization method is used to solve for the coefficients $\boldsymbol{A}$. The matrix ζ is replaced by its Singular Value Decomposition (SVD),

$$\zeta = U\Sigma V^*, \tag{5.31}$$

where $U_{m\times m}$ and $V^*_{6\times 6}$ are unitary matrices, and

$$\Sigma = \begin{pmatrix} \Sigma_{1,1} & 0 & \ldots & 0 \\ 0 & \Sigma_{2,2} & \ldots & 0 \\ \vdots & \vdots & \ddots & \vdots \\ 0 & 0 & \ldots & \Sigma_{6,6} \\ \vdots & \vdots & & \vdots \\ 0 & 0 & \ldots & 0 \end{pmatrix} \tag{5.32}$$

consists of the 6 singular values of ζ. Then (5.30) can be recast as

$$U\Sigma V^* \boldsymbol{A} = \boldsymbol{Y}, \tag{5.33}$$

and one can obtain the solution

$$\boldsymbol{A} = V\Sigma^{-1}U^*\boldsymbol{Y}. \tag{5.34}$$

From this calculation, the electric potential and field at (R_k, Z_k) are immediately obtained:

$$\phi(R_k, Z_k) \approx A_1, \tag{5.35}$$

$$\phi_r(R_k, Z_k) \approx A_2, \tag{5.36}$$

$$\phi_z(R_k, Z_k) \approx A_3. \tag{5.37}$$

5.3.2 Flow Field

The incompressible Navier-Stokes (5.7)-(5.8) are solved using the velocity decomposition approach of Beale and Layton [9]. Though this chapter focuses on Stokes flow dynamics, the numerical algorithm for the full Navier-Stokes equations is described for completeness. The fluid velocity and pressure are expressed as the sum of a *Stokes* part (marked with the subscript 's') and a *continuous* part (denoted 'c'):

$$\boldsymbol{u} = \boldsymbol{u}_s + \boldsymbol{u}_c, \qquad p = p_s + p_c. \tag{5.38}$$

The *Stokes* part satisfies

$$-\nabla p_s + \mu \Delta \boldsymbol{u}_s + \boldsymbol{F} = 0, \tag{5.39}$$

$$\nabla \cdot \boldsymbol{u}_s = 0, \tag{5.40}$$

including the boundary force. Solutions of (5.39)-(5.40) are obtained using the approach proposed by Leveque and Li [83]: The equations are reduced to a sequence of three Poisson problems for the pressure, p_s and the components of velocity, u_s and v_s. In this dissertation, the code developed by Li [85, 86] is used. The implementation is based on Mayo's method [97], and is valid for geometries in axisymmetric cylindrical coordinates. Both the immersed interface method and Mayo's method differ only in the way the jumps are computed: Along directions normal and tangential to the interface for the immersed interface method, or along the coordinate lines in Mayo's technique (see Appendix H). The basic idea of incorporating the jumps into the finite

difference scheme at irregular grid points remains the same in both methods. Due to this fundamental similarity, here Mayo's technique is also referred as immersed interface method.

Taking the divergence of (5.39) and applying (5.40) leads to

$$\nabla^2 p_s = \nabla \cdot \boldsymbol{F}, \qquad [\![p]\!] = f_n, \quad [\![\partial p/\partial n]\!] = \frac{1}{r}\frac{\partial}{\partial s}(f_s r), \tag{5.41}$$

where f_n and f_s are the components of the boundary force normal and tangential to the interface, respectively. In practice, the singular source term is eliminated from the right-hand side, and instead the pressure satisfies Laplace equation,

$$\nabla^2 p_s = 0, \tag{5.42}$$

with specified jump conditions. Using the standard second-order finite difference discretization gives

$$\frac{1}{h^2}\left(p_{i+1,j} + p_{i-1,j} + p_{i,j+1} + p_{i,j-1} - 4p_{i,j}\right) + \frac{1}{2hr_i}\left(p_{i+1,j} - p_{i-1,j}\right) = C^p_{i,j}, \tag{5.43}$$

where the correction term $C^p_{i,j}$ is determined using the same methodology as in [82] (also, see Appendix H). The resulting system of discretized equations for p_s is solved using fast Fourier transforms (FFT). Note that $C_{i,j}$ is non-zero only at irregular grid points.

Next, the velocity field $\boldsymbol{u}_s = (u_s, v_s)$ is computed. Using the pressure p_s, the equation for the velocity field with its jump conditions is

$$\frac{1}{\mu}\nabla p_s = \mu \nabla^2 \boldsymbol{u}_s, \qquad [\![\boldsymbol{u}_s]\!] = 0, \quad \mu[\![\partial u_s/\partial n]\!] = f_s \sin\theta, \quad \mu[\![\partial v_s/\partial n]\!] = -f_s \cos\theta. \tag{5.44}$$

Discretizing the r-component of velocity gives

$$\frac{1}{h^2}\left(u_{i+1,j} + u_{i-1,j} + u_{i,j+1} + u_{i,j-1} - 4u_{i,j}\right) + \frac{1}{2hr_i}\left(u_{i+1,j} - u_{i-1,j}\right) = \pi_{i,j} + C^u_{i,j}, \tag{5.45}$$

where $\pi_{i,j} = (p_{i+1,j} - p_{i-1,j})/(2h\mu)$. A similar discretization is obtained for the z-component of $\boldsymbol{u}_s$. As in the case of p_s, solutions for the velocity are obtained by FFT.

The solutions of the *continuous* part are computed by taking the difference between (5.7) and (5.39):

$$\frac{\partial \boldsymbol{u}_c}{\partial t} + \boldsymbol{u} \cdot \nabla \boldsymbol{u}_c = -\nabla p_c + \mu \nabla^2 \boldsymbol{u}_c + \boldsymbol{F}_b, \tag{5.46}$$

$$\nabla \cdot \boldsymbol{u}_c = 0, \tag{5.47}$$

where

$$\boldsymbol{F}_b = -\frac{\partial \boldsymbol{u}_s}{\partial t} - \boldsymbol{u} \cdot \nabla \boldsymbol{u}_s.$$

Note that $\boldsymbol{F}_b$ is not only defined on the boundary. It is a continuous function on the whole domain because $\boldsymbol{u}_s$ and its material derivative are continuous across the interface. Moreover, one can deduce that the jump conditions for p_c and $\boldsymbol{u}_c$ are zero, since the jumps for $p_s, \boldsymbol{u}_s$ are the same as those for $p, \boldsymbol{u}$. This, along with the continuity of $\boldsymbol{F}_b$, suggests $p_c, \boldsymbol{u}_c$ can be solved on a regular grid, without corrections at the interface.

Equation (5.46) is discretized using a second-order backward difference formula. The equation becomes

$$\frac{3\boldsymbol{u}_c^{n+1} - 4\tilde{\boldsymbol{u}}_c^{n} + \tilde{\boldsymbol{u}}_c^{n-1}}{2\Delta t} + \nabla p_c^n = \mu \nabla^2 \boldsymbol{u}_c^{n+1} + \boldsymbol{F}_b^{n+1}, \tag{5.48}$$

where

$$\tilde{\boldsymbol{u}}_c^{n} = \boldsymbol{u}_c(\boldsymbol{x}^n, t^n), \tag{5.49}$$

$$\tilde{\boldsymbol{u}}_c^{n-1} = \boldsymbol{u}_c(\boldsymbol{x}^{n-1}, t^{n-1}). \tag{5.50}$$

$\tilde{\boldsymbol{u}}_c^{n}$ and $\tilde{\boldsymbol{u}}_c^{n}$ are obtained by solving an initial value problem for the particle $\boldsymbol{x}(t)$. See Ref. [9] for more details.

A second-order projection method is used to solve (5.48). First, the intermediate velocity $\boldsymbol{u}_c^*$ is obtained from

$$\frac{3\boldsymbol{u}_c^* - 4\tilde{\boldsymbol{u}}_c^n + \tilde{\boldsymbol{u}}_c^{n-1}}{2\Delta t} + \nabla p_c^n = \mu\nabla^2\boldsymbol{u}_c^* + \boldsymbol{F}_b^{n+1}. \tag{5.51}$$

Rewriting it as,

$$\left(\frac{3}{2\Delta t} - \mu\nabla^2\right)\boldsymbol{u}_c^* = \boldsymbol{F}_b^{n+1} - \frac{1}{2\Delta t}(-4\tilde{\boldsymbol{u}}_c^n + \tilde{\boldsymbol{u}}_c^{n-1}) - \nabla p_c^n, \tag{5.52}$$

this equation is discretized using standard second-order finite difference operators, then solved by fast Fourier transforms. Next, $\boldsymbol{u}_c^{n+1}$ is found by projecting $\boldsymbol{u}_c^*$ onto the subspace of divergence-free vector fields. This is accomplished by defining $\boldsymbol{u}_c^{n+1}$ as

$$\boldsymbol{u}_c^{n+1} = \boldsymbol{u}_c^* - \Delta t\nabla\Phi. \tag{5.53}$$

Taking the divergence of the above equation, Φ emerges as the solution of the Poisson equation

$$\Delta t\nabla^2\Phi = \nabla\cdot\boldsymbol{u}_c^*. \tag{5.54}$$

Once is Φ is known, the pressure is updated,

$$\nabla p_c^{n+1} = \nabla p_c^n + \frac{3}{2}\nabla\Phi - \mu\Delta t\nabla^3\Phi, \tag{5.55}$$

and one finally arrives at the equation,

$$\frac{3\boldsymbol{u}_c^{n+1} - 4\tilde{\boldsymbol{u}}_c^n + \tilde{\boldsymbol{u}}_c^{n-1}}{2\Delta t} + \nabla p_c^{n+1} = \mu\nabla^2\boldsymbol{u}_c^{n+1} + \boldsymbol{F}_b^{n+1}. \tag{5.56}$$

To update the position of the boundary, the Eulerian velocity, $\boldsymbol{u}$ is interpolated on the interface using a second-order interpolation scheme that incorporates the jumps across the boundary [83]. Considering the r component u_s of velocity, one first chooses

the three closest points, (r_{i1}, z_{j1}), (r_{i2}, z_{j2}), and (r_{i3}, z_{j3}) to the point (R_k, Z_k) on the interface. Then, the interpolated velocity U is

$$U = \gamma_1 u_{i1,j1} + \gamma_2 u_{i2,j2} + \gamma_3 u_{i3,j3} - C, \tag{5.57}$$

where the coefficients γ_k need to be determined using the methodology in Section 5.3.1. The coefficients can be calculated explicitly,

$$\gamma_2 = \frac{(z_{j1} - Z_k)(r_{i3} - r_{i1}) - (r_{i1} - R_k)(z_{j3} - z_{j1})}{(r_{i2} - r_{i1})(z_{j3} - z_{j1}) - (r_{i3} - r_{i2})(z_{j2} - z_{j1})}, \tag{5.58}$$

$$\gamma_3 = \frac{(z_{j3} - z_{j1})(r_{i1} - R_k) - (r_{i2} - r_{i1})(z_{j1} - Z_k)}{(r_{i2} - r_{i1})(z_{j3} - z_{j1}) - (r_{i3} - r_{i2})(z_{j2} - z_{j1})}, \tag{5.59}$$

$$\gamma_1 = -(\gamma_2 + \gamma_3), \tag{5.60}$$

and the correction term

$$C = -(a_2[\![u]\!] + a_4[\![u_r]\!] + a_6[\![u_z]\!]), \tag{5.61}$$

where a_i are linear combinations of the γ_k. The markers are then advanced using the second-order Adams-Bashforth method

$$\boldsymbol{X}^{n+1} = \boldsymbol{X}^n + \Delta t \left(\frac{3}{2}\boldsymbol{U}^n - \frac{1}{2}\boldsymbol{U}^{n-1} \right). \tag{5.62}$$

5.3.3 Numerical Algorithm

Prior to solving the governing equations, the system is non-dimensionalized using the following scale: $\boldsymbol{x} = r_0 \boldsymbol{x}^*$, $p = \dfrac{\gamma}{r_0} p^*$, and $\boldsymbol{u} = U \boldsymbol{u}^*$. Here r_0 is the initial radius of the drop. The dimensionless governing equations become (after dropping the *)

$$-\nabla p + Ca \Delta \boldsymbol{u} + \int_0^{2\pi} \left(\boldsymbol{f}_\gamma + Ca_E \boldsymbol{f}_E \right) \delta^2 \left(\boldsymbol{x} - \boldsymbol{X}(s,t) \right) ds = 0, \tag{5.63}$$

$$\nabla \cdot \boldsymbol{u} = 0, \tag{5.64}$$

$$\nabla \cdot (\varepsilon \nabla \phi) = 0, \quad [\![\phi]\!] = 0, \quad [\![\sigma \phi_n]\!] = 0, \tag{5.65}$$

$$\boldsymbol{E} = -\nabla \phi, \quad \mathbf{M} = \varepsilon \left(\boldsymbol{E}\boldsymbol{E} - \frac{1}{2} E^2 \mathbf{I} \right), \mathbf{F}_E = [\![\mathbf{M}]\!] \cdot \boldsymbol{n}. \tag{5.66}$$

The problem depends on the capillary number $Ca = \mu U/\gamma$, the electric capillary number $Ca_E = \varepsilon^+ E_0^2 r_0/\gamma$, and the parameters $\varepsilon_r,\ \sigma_r$. The capillary number represents the ratio of viscous force to surface tension; and the electric capillary number reflects the strength of the electric field.

Given the position of the boundary at time t_n, the numerical implementation of the equations proceeds as follows:

1. Determine the interfacial electric field from (5.36) and (5.37), and calculate the electric force.

2. Compute the interfacial tension force.

3. Solve the sequence of three Poisson problems for the pressure and velocity components at time t^{n+1}.

4. Interpolate the fluid velocity to the boundary markers, and update the position of the boundary $\boldsymbol{X}^{n+1}$.

As noted in [43], a boundary located between two parallel plate capacitor would move along the axis of symmetry and toward one of the plates indefinitely, in the event the boundary deviates even slightly from its equilibrium position. In numerical simulations, boundaries are discretized such that their centroid rarely lie exactly at the center of the computational domain, and one needs to resolve the issue of drifting. Various approaches have been used: In some instances [42, 43], the center of mass of the drop is maintained at the coordinate origin by applying additional constraint to the system. Others [112] take advantage of the symmetry with respect to the equatorial plane to reduce the computational domain by half. In this work, the drop centroid is computed at every time step and moved back to the coordinate origin.

5.4 Results

A series of tests is performed to assess the convergence of the numerical methods for the electric potential, the interfacial electric force and the fluid variables. The computational domain is the half-plane $[0,3] \times [-3,3]$ and the mesh width $h = \frac{3}{N}$, where N is the grid number. The capillary number Ca in (5.63) is set to unity. No exact solution exists for this problem, so the rate of convergence is measured using the ratio

$$\text{ratio} = \log_2 \left(\frac{\|P_N - P_{N/2}\|_\infty}{\|P_{2N} - P_N\|_\infty} \right), \tag{5.67}$$

where P is the variable being measured.

5.4.1 Convergence Test for the Interfacial Electric Force

In this section, the convergence of the electric potential and the interfacial electric force are investigated. The conductivity and permittivity ratios are set to $\sigma_r = 3$ and $\epsilon_r = 2$, and the grid number, N takes values $N = 64,\ 128,\ 256,\ 512$. The number of boundary markers scales with the grid number, $N_B = N$, and the drop shape is an ellipsoid with major axis $a = 1.1$ and minor axis $b = 0.9$.

Table 5.1 Mesh Refinement Results for the Electric Potential at Grid Points, ϕ, and for the Interpolated Potential at the Interface. Results are shown separately for the Interfacial Interior (ϕ^-) and Exterior (ϕ^+) Potential

N	$\|\phi_{2N} - \phi_N\|_\infty$	ratio	$\|\phi^-_{2N} - \phi^-_N\|_\infty$	ratio	$\|\phi^+_{2N} - \phi^+_N\|_\infty$	ratio
32	3.8276×10^{-2}	-	1.6066×10^{-3}	-	1.1716×10^{-2}	-
64	6.2882×10^{-3}	2.6057	3.5428×10^{-4}	2.181	1.1632×10^{-3}	3.3322
128	1.0205×10^{-3}	2.6234	7.1949×10^{-5}	2.2998	1.63×10^{-4}	2.8352
256	3.3777×10^{-4}	1.5952	1.8199×10^{-5}	1.9831	2.7578×10^{-5}	2.5633

Table 5.1 shows the convergence results for the electric potential and for the interfacial potential, interpolated from the interior $(-)$ and exterior $(+)$. One can see that the convergence of the maximum errors is essentially second-order. The r and z-components of the interfacial electric force are plotted in Figure 5.5 for different N_B. The figure shows that the interfacial force converges with increased number of markers. Table 5.2 shows the refinement results for the component of the interfacial

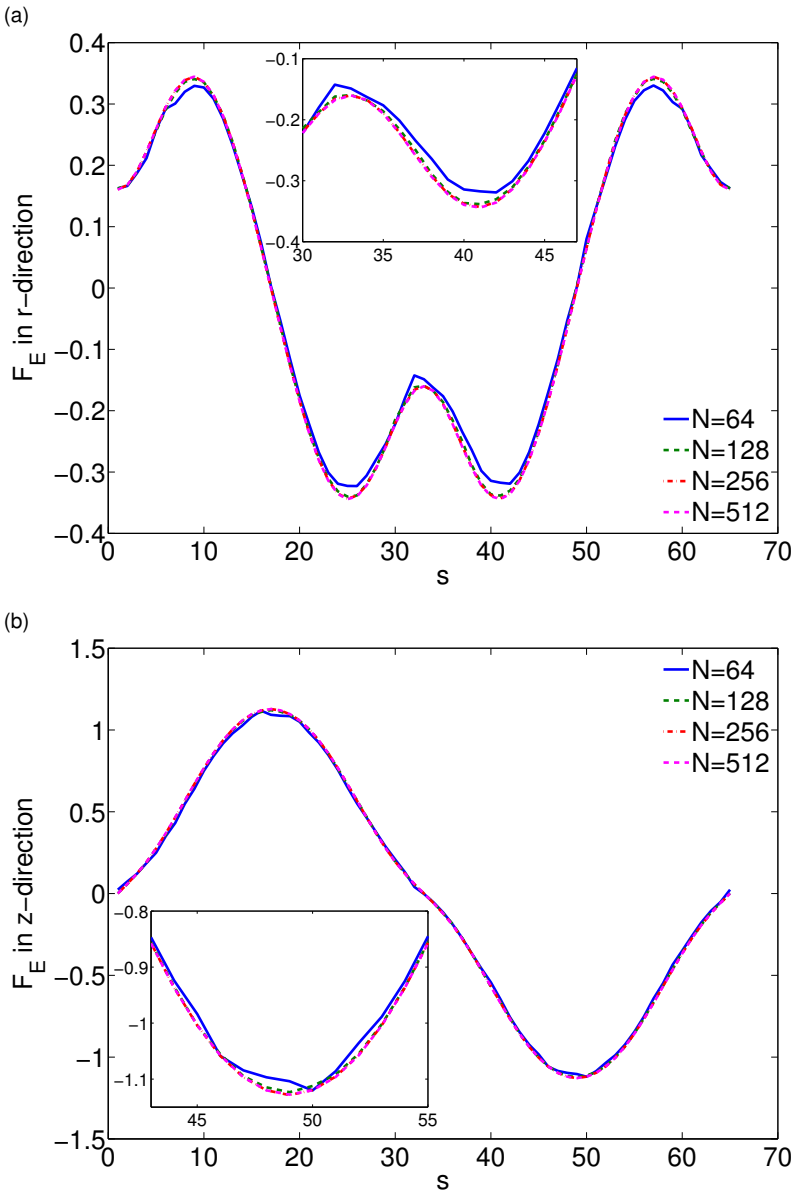

Figure 5.5 The interfacial electric force in the r and z-directions for boundary markers $N = 64,\ 128,\ 256,\ 512$.

electric force, further illustrating convergence of the force.

Table 5.2 Mesh Refinement Results for the Components of the Interfacial Electric Force $\mathbf{F}_E = (F_{E,r}, F_{E,z})$

N	$\|(F_{E,r})_{2N} - (F_{E,r})_N\|_\infty$	ratio	$\|(F_{E,z})_{2N} - (F_{E,z})_N\|_\infty$	ratio
64	2.4846×10^{-2}	-	3.181×10^{-2}	-
128	7.4899×10^{-3}	1.73	8.77×10^{-3}	1.8588
256	1.7042×10^{-3}	2.1358	2.2003×10^{-3}	1.9949

The successive error, defined as $\|(\boldsymbol{F}_E))_{2N} - (\boldsymbol{F}_E)_N\|_\infty$, is shown in Figure 5.6.

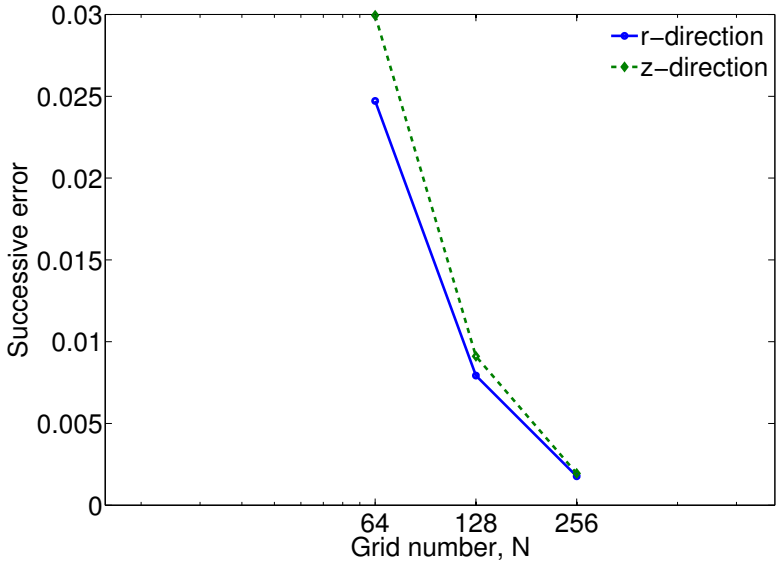

Figure 5.6 The successive error of the interfacial electric force. The rate of convergence is second-order.

5.4.2 Convergence Test for the Fluid Variables

In this section, the dynamics of a deforming drop is simulated to establish the spatial convergence of the fluid variables. Initially, the drop has a spherical shape, and the fluid is at rest. The conductivity ratio $\sigma_r = \frac{1}{10}$, and the permittivity ratio $\varepsilon_r = 0.04$.

The time step is chosen as $\Delta t = h/50$. Simulations are computed up to $T \sim 0.1$ for electric capillary number $Ca_E = 0.01$, corresponding to the limit of small deformation.

Table 5.3 shows the mesh refinement results for the fluid velocity. One can see that the convergence of the maximum errors is also second-order.

Table 5.3 Mesh Refinement Results for the Velocity Components u and v

N	$\|u_{2N} - u_N\|_\infty$	ratio	$\|v_{2N} - v_N\|_\infty$	ratio
32	8.4826×10^{-4}	-	3.6661×10^{-3}	-
64	1.9202×10^{-4}	2.1432	7.8144×10^{-4}	2.23
128	5.8371×10^{-5}	1.718	1.9147×10^{-4}	2.0291

5.4.3 Comparison with the Spheroidal Model

In this section, the time-dependent deformation of a drop in a DC electric field is simulated, and compared against the spheroidal model of Chapter 3. The deformation is quantified by the deformation number,

$$D = \frac{a-b}{a+b}, \tag{5.68}$$

where a and b represent the elongation along the major and minor axes, respectively. Additionally, the circulatory patterns predicted by the seminal work of Taylor are investigated for the prolate shape. According to [147], the flow pattern in the first quadrant is always clockwise for the prolate B, while it is counterclockwise for prolate A. The distinction depends on the parameters σ_r and ε_r: Clockwise circulation for $\sigma_r > \varepsilon_r$, and otherwise for $\sigma_r < \varepsilon_r$.

For the following results, the grid size $N = 128$, and simulations are run until the drop reaches steady-state. The simulation parameters are the same as

in [77]: $(\sigma_r, \varepsilon_r) = (10, 0.04)$ for Prolate A, and $(\sigma_r, \varepsilon_r) = (100, 0.1)$ for Prolate B. Figure 5.7 shows a comparison of the deformation between the spheroidal model

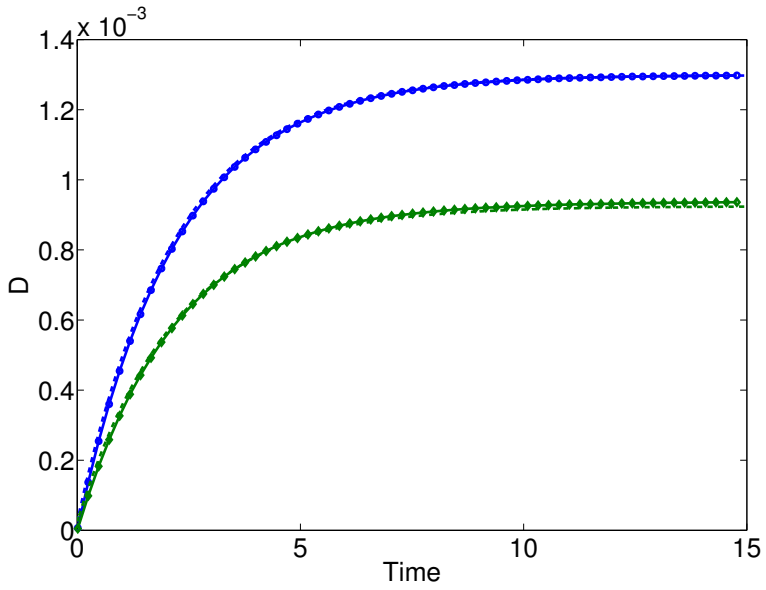

Figure 5.7 Numerical (solid) and analytical (dashed) predicted drop deformation.

and the numerical simulations. At steady-state ($T \sim 15$), the difference in the deformations predicted by the analytical and numerical results is 4.4×10^{-7} for the Prolate A, and 1.277×10^{-5} for Prolate B shapes.

Figure 5.8 and Figure 5.9 show the velocity field at different times for the parameters in Figure 5.7. One can note the flow patterns in each of the first quadrant: The induced flows are clockwise for Prolate B, and counter-clockwise for Prolate A. These results are in good agreement with those in [147].

5.5 Conclusion

In this chapter, a numerical code based on the immersed interface method was developed to simulate the electro-deformation of a leaky dielectric, viscous drop in Stokes flow. For the solution of the electric potential, the immersed interface method in [82] was extended to three-dimensional axi-symmetric cylindrical coordinates. To

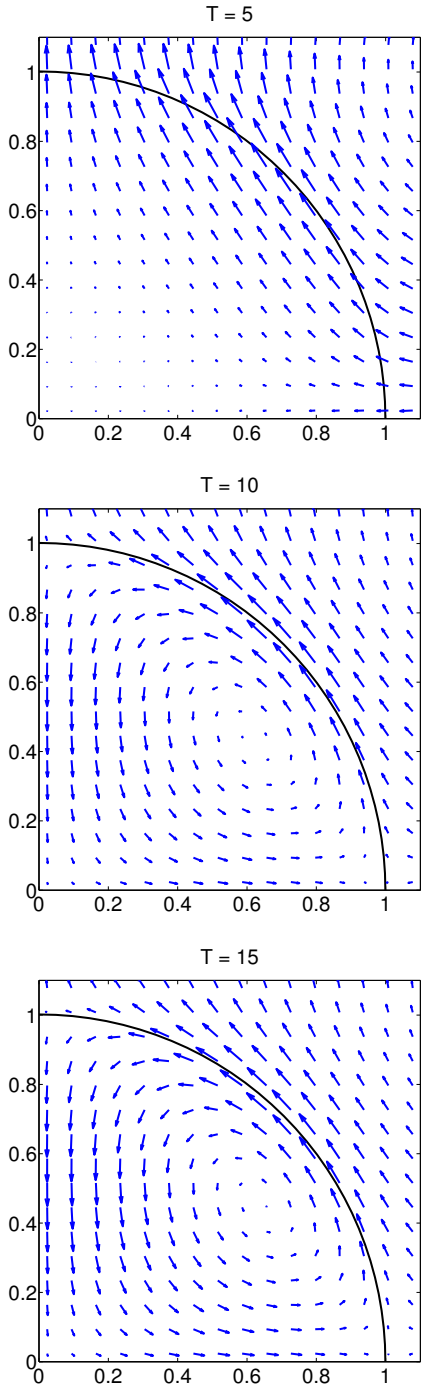

Figure 5.8 Time-dependent velocity field for the Prolate A shape. Here, $(\sigma_r, \varepsilon_r) = (10, 0.04)$. The electric capillary number is $Ca_E = 0.01$.

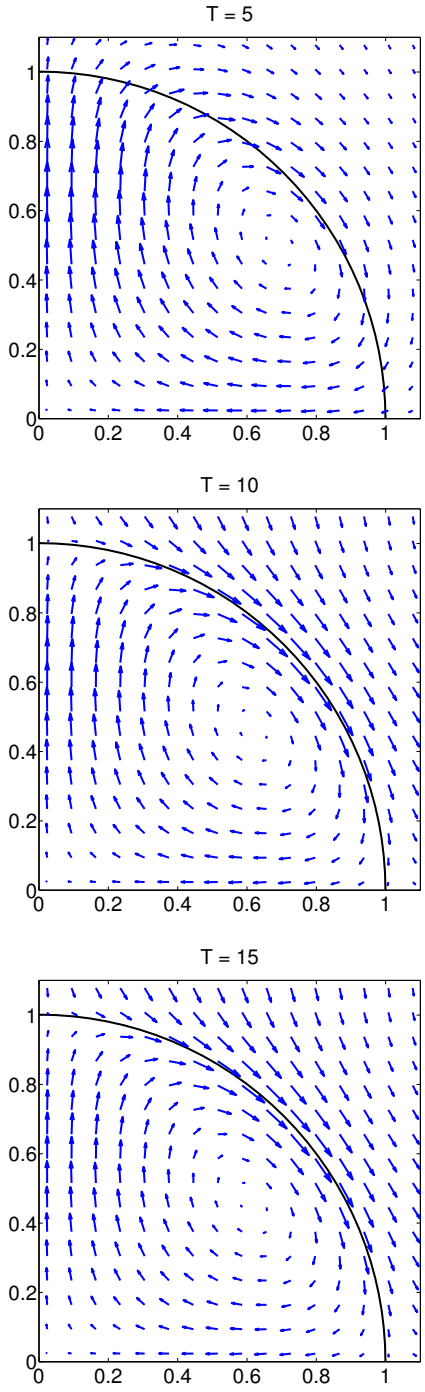

Figure 5.9 Time-dependent velocity field for the Prolate B shape. Here, $(\sigma_r, \varepsilon_r) = (100, 0.1)$. The electric capillary number is $Ca_E = 0.01$.

the author's knowledge, this had not been reported in the literature before. Using one-sided least-squares interpolation, the electric potential and electric field were obtained on either side of the drop surface, and the electric force was treated as an interfacial force, as in [61]. Mesh refinement results showed that the convergence of the maximum errors was (nearly) second order for the potential, the electric force and the fluid variables.

The code was used to obtain the time-dependent deformation of the drop for the two prolate modes: Prolate A and Prolate B. The simulation results compared well with predictions from the spheroidal model of Chapter 3 in terms of the drop deformation. Moreover, circulatory patterns in both cases also agreed with results in the literature.

CHAPTER 6

CONCLUSION

A set of analytical and numerical tools have been developed to investigate the steady and time-dependent dynamics of a deformable interface in an electric field. In Chapter 3, a spheroidal model was constructed to capture the equilibrium deformation of a surfactant-laden viscous drop in a DC electric field. Based on the electric properties of the fluids, the deformation was found to be either prolate or oblate. In addition, the prolate shape was further differentiated into prolate A or prolate B based on the circulatory patterns inside the drop. Surfactant effects on drop deformation were also studied. Depending on the elasticity number and surfactant coverage, surfactants were found to enhance deformation in some cases (tip stretching), while reducing deformation in others (surface dilution). Comparisons between the spheroidal model and experiments showed very good agreement, compared to the small-deformation theory. Furthermore, good agreement in the limit of large deformation was also found between the spheroidal model and numerical studies in the literature.

In Chapter 4, the spheroidal model was extended to study the electro-deformation of a vesicle in an AC electric field. The vesicle membrane was modeled as a spheroidal shell, and an expression for the transmembrane potential was derived. Equilibrium shapes were computed by balancing forces between the fluid, the membrane and the electric field. Comparisons between the small-deformation theory and the spheroidal results were drawn. The results showed that the spheroidal model gave better agreement with the experiments in the literature. The observation also held at the prolate-to-oblate crossover frequency, at which the spheroidal model was able to capture the rate of change of vesicle shape more accurately.

Finally, Chapter 5 presented a novel numerical code for the simulation of a viscous drop under DC electric field. The code is entirely based on the second-order

immersed interface. To the author's knowledge, this had not been reported in the literature. Numerical studies on the scheme shows numerical convergence and very good agreement with the analytical results of Chapter 3 for a surfactant-free drop. Moreover, the circulatory patterns inside the drop were also in agreement with those in the literature.

CHAPTER 7

ONGOING AND FUTURE WORK

The tools developed in this dissertation provide a range of options for further investigations. In this chapter, ongoing investigations are described, and future work is discussed.

7.1 Near-Contact Motion of Surfactant-covered Spheroidal Drops: Ionic Surfactant

The model is Chapter 3 can be modified to investigate the motion of spheroidal drops in the presence of insoluble ionic surfactant. The equation of state (3.2) can be substituted with [14]:

$$\gamma(\Gamma) - \gamma(0) = -k_B T \Gamma \left[1 + \frac{2\nu}{Z\bar{\Gamma}} \left(\sqrt{(Z\bar{\Gamma})^2 + 1} - 1 \right) \right], \tag{7.1}$$

Here, T is temperature, k_B is the Boltzmann's constant, and $\nu = \frac{z_s}{z}$ denotes the ratio of the charge valence of the surfactant molecules to the ions' charge valence. The dimensionless surfactant concentration is $\bar{\Gamma} = \Gamma/\Gamma_0$, and the surface potential parameter

$$Z = \frac{e^2 z z_s \Gamma_0}{2\varepsilon\kappa k_B T},$$

where e is an electron charge, and κ^{-1} is the Debye length. This change gives new equations for the equilibrium surfactant distribution, and for the equilibrium shape of the drop. More importantly, an analysis similar the the one presented in [14] for spherical drops can be extended to spheroidal drops. The goal is to determine how large deformations predicted by the spheroidal model would affect the results in [14].

7.2 Bilayer Lipid Membrane Structure

In Chapter 4, the vesicle membrane was approximated by a single layer. This approximation is valid assuming that the motion of the two membrane leaflets is

identical. In other word, the intermonolayer friction is large. This assumption can be relaxed, and the spheroidal approach can be extended to include the bilayer structure (two leaflets).

For the bilayer structure, the boundary conditions at the vesicle membrane still include the continuity of velocity, but only for the normal component:

$$\boldsymbol{u}_e \cdot \boldsymbol{n} = \boldsymbol{u}_i \cdot \boldsymbol{n} = \frac{d\boldsymbol{x}}{dt} \cdot \boldsymbol{e}_\xi. \tag{7.2}$$

The stress balance (4.19)-(4.20) are replaced with

$$\int_{\xi=\xi_0(t)} u \cdot [\![\mathbf{T}_{\xi\eta} + \mathbf{S}_{\xi\eta}]\!] = 0, \tag{7.3}$$

$$\int_{\xi=\xi_0(t)} u \cdot \left[\mathbf{T}^+_{\xi\eta} + \mathbf{T}^-_{\xi\eta} + \mathbf{S}^+_{\xi\eta} + \mathbf{S}^-_{\xi\eta} - 2\tilde{b}\,(\boldsymbol{u}_e - \boldsymbol{u}_i)\cdot\boldsymbol{t}\right] = 0, \tag{7.4}$$

$$\int_{\xi=\xi_0(t)} v \cdot [[\![-p + \mathbf{T}_{\xi\xi} + \mathbf{S}_{\xi\xi}]\!] - \gamma\,(\nabla\cdot\hat{\boldsymbol{n}})] = 0, \tag{7.5}$$

where $\tilde{b}$ [$\mathrm{Pa}\cdot\mathrm{s}\cdot\mathrm{m}^{-1}$] is the coefficient of friction. As before, (e) or (i) subscripts designate the exterior or interior of the vesicle, respectively.

Following the outline in Appendix I, one can derive the dimensional governing equation for the shape parameter in the prolate spheroidal coordinates:

$$\frac{d\xi_0}{dt} = \frac{\mathcal{Q}_N f_{31} + \chi\left(\mathcal{Q}^\Delta_T, \mathcal{Q}^\Sigma_T\right) - \sigma_h f_{36}}{\frac{2}{3}\mu_i D}. \tag{7.6}$$

The terms $\mathcal{Q}_N f_{31}$ and $\sigma_h f_{36}$ corresponds to $\mathcal{Q}_N f_{21}$ and $\sigma_h f_{24}$, resp. in Zhang *et al.* Moreover, the tangential component,

$$\chi\left(\mathcal{Q}^\Delta_T, \mathcal{Q}^\Sigma_T\right) = \frac{\varepsilon_e}{c^2}\frac{\mathcal{Q}^\Delta_T f_{11} f_{32}}{f_{17}} - \frac{\varepsilon_e}{c^2 T_1}\left(\frac{f_{15}f_{32}}{f_{17}} + f_{35}\right)\left(\frac{\tilde{b}c\mathcal{Q}^\Delta_T f_{11} f_{26}}{\mu_i\mu_r f_{17}} + \frac{\mathcal{Q}^\Delta_T f_{11} f_{21}}{f_{17}} - \mathcal{Q}^\Sigma_T f_{11}\right),$$

and

$$D = \mu_r f_{33} + f_{34} + \left(\frac{f_{15}f_{32}}{f_{17}} + f_{35}\right)\frac{T_2}{T_1} - \frac{[(\mu_r - 1)f_{12} - f_{13}]\,f_{32}}{f_{17}}.$$

Equation (7.6) is being used to investigate the effects of intermonolayer friction on the deformation of a vesicle. Predictions from the model will be validated against available experimental data [34].

7.3 Numerical Simulation of a Viscous Drop

The axisymmetric numerical code presented in Chapter 5 is currently being used to investigate the time-dependent dynamics of a viscous drop in the limit of large deformation, where spheroidal shapes may not exist. As the electric capillary number Ca_E is increased, the boundary becomes stiff due to the increasing electric force. Immersed boundary methods are known to require prohibitively small time steps [139] for stiff problems. To alleviate this short-coming, there's been much effort devoted to developing (semi-)implicit time-marching schemes, to allow for larger time steps [9, 80, 98, 108]. However, the implementation of these implicit methods often require a high degree of complexity, as the boundary force needs to also be treated implicitly. Alternatively, computation time can be reduced by employing fast methods to solve for the electric potential and the flow field. In Chapter H, the flow field is obtained using a fast solver and so the efficiency is already optimized. The use of SOR-GMRES to solve for the electric potential in Figure 5.7 requires about ten (10) seconds per time step iteration with $N = 128$, and an optimal SOR relaxation parameter. Much of that time is spent computing the preconditioner matrix, which is obtained for the entire computational domain. Two different methods, the multigrid approach of de Zeeuw [29, 88], and the augmented immersed interface method [87], are currently being tested to substitute for SOR-GMRES.

7.4 Electrokinetic Effects

Electrokinetic effects on the present results will be explored in the future. Hsu *et al.* [59] reported strong dependence of the electrokinetic behaviors of ellipsoidal polyelectrolyte (PE) on its shape. They incorporated the charged ions effects by assuming that the

electric field, $\boldsymbol{E}$ was much weaker than the field established by the PE. The spheroidal model in this dissertation could be extended in a similar fashion, by having the electric potential satisfy the Poisson-Nerst-Plank (PNP) equations, which account for the transport of various charged species in the fluids. The modified, electrokinetic equations could provide valuable insight into the dependence of equilibrium shape on the electric double layer thickness (Debye layer), which results from bulk electrolytes.

Relaxing the assumption in [59] will require numerical computations. The numerical code in this dissertation can be readily adapted to include electrokinetic effects. In the case of the drop, it will be interesting to see how ionic surfactant diffusion and solubility may modify equilibrium results reported in this work. In some time-dependent calculations it was found that, in some cases, non- diffusing surfactant cannot immobilize the drop surface to prevent the surfactant concentration from reaching the maximum packing. In reality surfactant diffusion is a weak effect, and is unlikely to greatly change the conclusion on the spheroidal equilibrium. However, the lack of a spheroidal equilibrium may be an indication that a non-spheroidal equilibrium shape is favored instead. The numerical code could help shed some light in understanding how the surfactant distribution and circulation may contribute to non-spheroidal drop deformation and different modes of drop breakup.

7.5 Numerical Simulation of Vesicles in an Electric Field

The various projects covered in this dissertation, and the projects that would follow have a specific goal in common: To investigate the dynamic process leading to the formation of pores on vesicles membranes. The literature abound with numerical studies of vesicles subjected to an imposed flow [152, 153, 60], but there exist few numerical studies of vesicle electrohydrodynamics. Kolahdouz and Salac developed a numerical approach to the electric field around a stationary vesicle in a DC electric field in three-dimensional cartesian coordinates. They are in the early development

of a numerical model for the dynamics of a vesicle in an electric field, based on the three-dimensional immersed interface method. The axisymmetric numerical code in this dissertation will be extended to simulate vesicles in DC or AC electric fields. Initially, the focus will be on electro-neutral bulk fluid using the leaky dielectric framework. Later on, electrokinetics effects will also be considered.

Solvents are known to destabilize lipid membrane in a DC electric field [78]. It is reasonable to expect more complex dynamics and equilibrium shapes for a vesicle immersed in electrolytes in an AC field. For example, a vesicle under an electric field may have very different morphology that depends on the net charges in the bulk. Numerical investigations will be conducted to determine how the morphological phase diagram in Figure 4.6 may be altered by solvent electrokinetics.

After determining the effects of electrolytes on vesicles dynamics, the logical next step will be to study the combined effects of an imposed flow and an electric field on vesicles dynamics, which is a more realistic scenario for vesicles in experiments. To the author's knowledge, this problem has only been investigated analytically by Schwalbe [134]. Numerical simulations have yet to be extended to this problem, which is a critical step toward greater understanding of electrically-induced membrane poration.

APPENDIX A

GENERALIZED EIGENFUNCTIONS IN SPHEROIDAL COORDINATES

The generalized functions of $\mathbf{E}^2$ used to express the stream function in spheroidal coordinates are

$$\Omega_0^{(1)} = - G_0(\xi)G_2(\eta) - G_2(\xi)G_0(\eta), \tag{A.1}$$

$$\Omega_0^{(2)} = \frac{1}{3}G_0(\xi)G_3(\eta) - G_2(\xi)G_1(\eta), \tag{A.2}$$

$$\Omega_0^{(3)} = \frac{1}{3}G_3(\xi)G_0(\eta) - G_1(\xi)G_2(\eta), \tag{A.3}$$

$$\Omega_0^{(4)} = \frac{1}{3}G_1(\xi)G_3(\eta) + \frac{1}{3}G_3(\xi)G_1(\eta), \tag{A.4}$$

$$\Omega_1^{(1)} = \Omega_0^{(4)}, \tag{A.5}$$

$$\Omega_1^{(2)} = - \Omega_0^{(3)}, \tag{A.6}$$

$$\Omega_1^{(3)} = - \Omega_0^{(2)}, \tag{A.7}$$

$$\Omega_1^{(4)} = \Omega_0^{(1)}, \tag{A.8}$$

$$\Omega_2^{(1)} = \frac{2}{25}G_2(\xi)G_4(\eta) + \frac{2}{25}G_4(\xi)G_2(\eta), \tag{A.9}$$

$$\Omega_2^{(2)} = \frac{2}{25}G_2(\xi)H_4(\eta) + \frac{2}{25}G_4(\xi)H_2(\eta) + \frac{1}{6}G_2(\xi)G_1(\eta), \tag{A.10}$$

$$\Omega_2^{(3)} = \frac{2}{25}H_2(\xi)G_4(\eta) + \frac{2}{25}H_4(\xi)G_2(\eta) + \frac{1}{6}G_1(\xi)G_2(\eta), \tag{A.11}$$

$$\Omega_2^{(4)} = \frac{2}{25}H_2(\xi)H_4(\eta) + \frac{2}{25}H_4(\xi)H_2(\eta) + \frac{1}{6}G_1(\xi)H_2(\eta) + \frac{1}{6}H_2(\xi)G_1(\eta), \tag{A.12}$$

$$\Omega_3^{(1)} = \frac{2}{49}G_3(\xi)G_5(\eta) + \frac{2}{49}G_5(\xi)G_3(\eta), \tag{A.13}$$

$$\Omega_3^{(2)} = \frac{2}{49}G_3(\xi)H_5(\eta) + \frac{2}{49}G_5(\xi)H_3(\eta) - \frac{1}{90}G_3(\xi)G_0(\eta), \tag{A.14}$$

$$\Omega_3^{(3)} = \frac{2}{49}H_3(\xi)G_5(\eta) + \frac{2}{49}H_5(\xi)G_3(\eta) - \frac{1}{90}G_0(\xi)G_3(\eta), \tag{A.15}$$

$$\Omega_3^{(4)} = \frac{2}{49}H_3(\xi)H_5(\eta) + \frac{2}{49}H_5(\xi)H_3(\eta) - \frac{1}{90}G_0(\xi)H_3(\eta) - \frac{1}{90}H_3(\xi)G_0(\eta), \tag{A.16}$$

and for $n = 4, 5, \ldots$

$$\begin{aligned}
\Omega_n^{(1)} =& \frac{\alpha_n}{2(2n-3)} \left[G_{n-2}(\xi) G_n(\eta) + G_n(\xi) G_{n-2}(\eta) \right] \\
&+ \frac{\beta_n}{2(2n+1)} \left[G_{n+2}(\xi) G_n(\eta) + G_n(\xi) G_{n+2}(\eta) \right], \qquad \text{(A.17)} \\
\Omega_n^{(2)} =& - \frac{\alpha_n}{2(2n-3)} \left[G_{n-2}(\xi) H_n(\eta) + G_n(\xi) H_{n-2}(\eta) \right] \\
&+ \frac{\beta_n}{2(2n+1)} \left[G_{n+2}(\xi) H_n(\eta) + G_n(\xi) H_{n+2}(\eta) \right], \qquad \text{(A.18)} \\
\Omega_n^{(3)} =& - \frac{\alpha_n}{2(2n-3)} \left[H_{n-2}(\xi) G_n(\eta) + H_n(\xi) G_{n-2}(\eta) \right] \\
&+ \frac{\beta_n}{2(2n+1)} \left[H_{n+2}(\xi) G_n(\eta) + H_n(\xi) G_{n+2}(\eta) \right], \qquad \text{(A.19)} \\
\Omega_n^{(4)} =& - \frac{\alpha_n}{2(2n-3)} \left[H_{n-2}(\xi) H_n(\eta) + H_n(\xi) H_{n-2}(\eta) \right] \\
&+ \frac{\beta_n}{2(2n+1)} \left[H_{n+2}(\xi) H_n(\eta) + H_n(\xi) H_{n+2}(\eta) \right]. \qquad \text{(A.20)}
\end{aligned}$$

The coefficients α_n and β_n are given by

$$\begin{aligned}
\alpha_n &= \frac{(n-3)(n-2)}{(2n-3)(2n-1)}, \qquad n \geq 4, \qquad \text{(A.21)} \\
\beta_n &= \frac{(n+1)(n+2)}{(2n-1)(2n+1)}, \qquad n \geq 4. \qquad \text{(A.22)}
\end{aligned}$$

APPENDIX B

SECOND-ORDER SMALL-DEFORMATION ANALYSIS FOR A SPHERICAL DROP

Consider a leading-order perturbative solution around a sphere in the form

$$\mathbf{E} = \mathbf{E}^{\infty} + \mathbf{E}^{(0)} + \ldots, \qquad \boldsymbol{u} = \boldsymbol{u}^{(0)} + \boldsymbol{u}^{(1)}(f, g) + \ldots. \tag{B.1}$$

The leading-order velocity field, $\boldsymbol{u}^{(0)}$, described the flow about a spherical drop generated by the imposed electric field, where f and g denote the drop deformation and surfactant distribution, respectively. The term $\boldsymbol{u}^{(1)}$ describes the flow driven by capillary and Marangoni stresses, i.e., relaxation of the deformed drop and surfactant back to the equilibrium spherical shape/uniform distribution. For the electric field applied in the z-direction, the shape function r_s and surfactant distribution are expressed as

$$r_s = r_0\left(1 + f_{20}\left(-\frac{1}{3} + \cos^2\theta\right)\right), \quad \Gamma = \Gamma_{eq}\left(1 + g_{20}\left(-\frac{1}{3} + \cos^2\theta\right)\right), \tag{B.2}$$

where f_{20} and g_{20} are the leading-order coefficients of scalar spherical harmonics (corresponding to $j = 2$ and $m = 0$ mode).

In the small-deformation analysis both the drop deformation and the deviation of Γ from the uniform distribution are assumed to be small [156] therefore we use the linear equation of state for the surface tension

$$\gamma(\Gamma) = 1 + \tilde{E}(1 - \Gamma), \tag{B.3}$$

where $\tilde{E} \equiv (\gamma_0 - \gamma_{eq})/\gamma_{eq}$. The relation between the capillary number based on the clean drop surface tension and the capillary number based on the equilibrium surface tension of the surfactant-covered drop is $Ca_0 = Ca_E(1 + \tilde{E})^{-1}$, and the Marangoni number $Ma = \tilde{E}Ca^{-1}$. The solution for $\mathbf{E}^{(0)}$ and $\boldsymbol{u}^{(0)}$ can be found in Refs. [155]

and [133], and for $\boldsymbol{u}^{(1)}$ in Refs. [156] and [133]. Combining these solutions one obtains the evolution equation for the shape and surfactant:

$$\frac{df_{20}}{dt} = c_{202} + Ca_0^{-1} C_c(\mu_r) f_{20} + Ma\left[C_{mf}(\mu_r) f_{20} + C_{mg}(\mu_r) g_{20}\right], \tag{B.4}$$

$$\frac{dg_{20}}{dt} = c_{222} + Ca_0^{-1} M_c(\mu_r) f_{20} + Ma\left[M_{mf}(\mu_r) f_{20} + M_{mg}(\mu_r) g_{20}\right]. \tag{B.5}$$

In the absence of surfactant, $Ma = 0$, and the evolution equations reduce to the Taylor solution for a clean drop. In (B.4) and (B.5), the inhomogeneous term represents the distortion of the drop shape and surfactant distribution by the straining EHD flow:

$$c_{202} = \frac{9(5 + (6 + 5/\sigma_r)/\sigma_r + (5 + (9 + 5/\sigma_r)/\sigma_r - 19/\varepsilon_r)/\mu_r - 16/\varepsilon_r)}{(19/\mu_r + 16)(2/\mu_r + 3)(2 + 1/\sigma_r)^2}, \tag{B.6}$$

$$c_{222} = \frac{27((3 + (13 + 3/\sigma_r)/\sigma_r - 19/\varepsilon_r)/\mu_r + 2(1 + (6 + \sigma_r)/\sigma_r - 8/\varepsilon_r))}{(19/\mu_r + 16)(2/\mu_r + 3)(2 + 1/\sigma_r)^2}. \tag{B.7}$$

The terms proportional to Ca_0^{-1} describe relaxation of the drop shape and surfactant distribution driven by capillary stresses:

$$C_c(\mu_r) = -\frac{40\mu_r(1 + \mu_r)}{(19 + 16\mu_r)(2 + 3\mu_r)}, \quad M_c(\mu_r) = -\frac{24\mu_r(3 + 2\mu_r)}{(19 + 16\mu_r)(2 + 3\mu_r)}. \tag{B.8}$$

The terms proportional to Ma describe relaxation of the drop shape and surfactant distribution driven by Marangoni stresses:

$$C_{mf}(\mu_r) = \frac{12\mu_r(3 + 2\mu_r)}{((19 + 16\mu_r)(2 + 3\mu_r)}, \quad C_{mg}(\mu_r) = \frac{2\mu_r(1 + 4\mu_r)}{(19 + 16\mu_r)(2 + 3\mu_r)}, \tag{B.9}$$

$$M_{mf}(\mu_r) = \frac{6\mu_r(26 + 24\mu_r)}{((19 + 16\mu_r)(2 + 3\mu_r)}, \quad M_{mg}(\mu_r) = -\frac{\mu_r(7 + 8\mu_r)}{(19 + 16\mu_r)(2 + 3\mu_r)}. \tag{B.10}$$

One obtains the discriminating function from (B.4) and (B.5)

$$D_L = \frac{9((1 + 1/\sigma_r)^2 - 4/\varepsilon_r)}{16(2 + 1/\sigma_r)^2}, \tag{B.11}$$

where $D_L = 0$ gives the boundary between prolate and oblate shapes on the $(\sigma_r, \varepsilon_r)$-plane. Continuing on to the second order terms (omitted here), one obtains the equilibrium drop deformation $D_{eq} \equiv \frac{a-b}{a+b}$ as

$$D_{eq} = D_L Ca_E \left[1 + \frac{1/\sigma_r(1/\sigma_r(139/\sigma_r + 264) - 696/\varepsilon_r + 111) + 336/\varepsilon_r - 154}{80(1/\sigma_r + 2)^3}\right]. \tag{B.12}$$

APPENDIX C

DERIVATION OF THE GOVERNING EQUATION FOR THE OBLATE SHAPE FUNCTION

The derivation of the governing equation for the shape function for prolate drop subjected to a dc electric field was done by Zhang *et al.* However the authors did not treat the case of oblate shapes. In the next few lines, the general governing equation for the shape function is derived using the oblate spheroidal coordinates described earlier.

Given the point, $\vec{x} = (x_1(\lambda,\eta,\phi), x_2(\lambda,\eta,\phi), x_3(\lambda,\eta,\phi))$ in oblate spheroidal coordinates, the scale factors are computed as $h_i = \left|\frac{\partial \vec{x}}{\partial q_i}\right|$. The scale factors in oblate spheroidal coordinates are

$$h_\lambda = c\sqrt{\frac{\lambda^2+\eta^2}{\lambda^2+1}},\ h_\eta = c\sqrt{\frac{\lambda^2+\eta^2}{1-\eta^2}},\ h_\zeta = c\sqrt{(\lambda^2+1)\,(1-\eta^2)}. \tag{C.1}$$

The velocity at every point $\boldsymbol{x} = \boldsymbol{x}(\lambda,\eta,c)$ on the droplet surface is

$$\frac{d\boldsymbol{x}}{dt} = h_\lambda \frac{d\lambda}{dt}\boldsymbol{e}_\lambda + h_\eta \frac{d\eta}{dt}\boldsymbol{e}_\eta + \frac{\boldsymbol{x}}{dc}\frac{dc}{dt}, \tag{C.2}$$

where $\boldsymbol{e}_i = \frac{1}{h_i}\frac{\partial \boldsymbol{x}}{\partial q_i}$. If we only consider the normal velocity component, which is in the direction of $\boldsymbol{e}_\lambda$, we obtain

$$v_\lambda = \frac{r_0}{3\sqrt{\lambda_o^2+1}(\lambda_o^3+\lambda_o)^{1/3}}\frac{3\eta^2-1}{\sqrt{\lambda_o^2+\eta^2}}\frac{d\lambda_o}{dt}. \tag{C.3}$$

The equation of a spheroid is given by $\dfrac{x_1^2+x_2^2}{b^2}+\dfrac{x_3^2}{a^2} = \dfrac{r^2}{b^2}+\dfrac{z^2}{a^2} = 1$, where $r = c\sqrt{(\lambda^2+1)(1-\eta^2)}$ and $z = c\lambda\eta$. The principal radii of curvature for a figure of revolution [39] are

$$R_1 = (z'')^{-1}\left[1+(z')^2\right]^{3/2}, \qquad R_2 = r(z')^{-1}\left[1+(z')^2\right]^{1/2}, \tag{C.4}$$

where the rotation is about the z axis and the derivatives $z^{(i)} \equiv \frac{d^i z}{dr^i}$. Solving for z, then carrying out the differentiations and substituting into (C.4), one obtains

$$R_1 = \frac{c(\lambda_o^2+\eta^2)^{3/2}}{\lambda_o(\lambda_o^2+1)^{1/2}}, \quad R_2 = \frac{c(\lambda_o^2+1)^{1/2}(\lambda_o^2+\eta^2)^{1/2}}{\lambda_o}, \tag{C.5}$$

and the curvature of the oblate spheroid is

$$\kappa = \frac{1}{R_1} + \frac{1}{R_2} = \frac{\lambda_o\left(2\lambda_o^2+1+\eta^2\right)}{c(\lambda_o^2+1)^{1/2}(\lambda_o^2+\eta^2)^{3/2}}. \tag{C.6}$$

Using the continuity of velocities and the kinematic equation, the coefficients A_3^1, B_3^3 and B_3^5 can be written in terms of A_3^3 and λ_o:

$$A_3^1 = A_3^3 H_3 + M\lambda_o', \tag{C.7}$$

$$B_3^3 = \frac{-A_3^3 G_5 H_3' - M G_5' \lambda_o'}{N}, \tag{C.8}$$

$$B_3^5 = \frac{A_3^3 G_3 H_3' + M G_3' \lambda_o'}{N}, \tag{C.9}$$

where $M = \frac{2}{3}c^3$ and $N = G_3 G_5' - G_3' G_5$.

We can eliminate A_3^3 as an unknown by substituting the expressions of A_3^1, B_3^3, and B_3^5 above into the tangential stress balance,

$$\int_{-1}^{1} u \cdot \left(\left[\!\left[\mathbf{T}_{\xi\eta}\right]\!\right] + \left[\!\left[\mathbf{S}_{\xi\eta}\right]\!\right]\right) h_\eta h_\zeta d\eta = 0,$$

to get

$$A_3^3 = \frac{-\varepsilon_i c\left[\varepsilon_r(-cE_0+\alpha Q_1')(-cE_0\lambda_o+\alpha Q_1) + \lambda_o\beta_1^2\right] f_{11} + \mu_i\left[\left(\mu_r-1\right) f_{12} + f_{13}\right] M\lambda_o'}{\mu_i\left(\mu_r f_{14} + f_{15}\right)}. \tag{C.10}$$

These expressions are then substituted into the normal stress balance to obtain an ODE for the shape function

$$\frac{d\lambda_o}{dt} = \frac{\mathcal{Q}_N f_{21} + \mathcal{Q}_T \frac{\lambda_o f_{11}(\mu_r f_{22}+f_{23})}{\mu_r f_{14}+f_{15}} - \gamma_0 f_{24}}{\frac{2\mu_i}{3}(\mu_r f_{25}+f_{26})}, \tag{C.11}$$

$$\mathcal{Q}_N = \frac{\varepsilon_i}{c^2}\left[-\varepsilon_r(-cE_0+\alpha Q_1')^2 - \varepsilon_r\left(-cE_0+\alpha\frac{Q_1}{\lambda_o}\right)^2 - 2\beta_1^2\right], \tag{C.12}$$

$$\mathcal{Q}_T = \frac{\varepsilon_i}{c^2}\left[\varepsilon_r(-cE_0+\alpha Q_1')\left(-cE_0+\alpha\frac{Q_1}{\lambda_o}\right) + b_1^2\right]. \tag{C.13}$$

In dimensionless form, the equation reads

$$\frac{d\lambda_o}{dt} = \frac{\mathcal{Q}_N f_{21} + \mathcal{Q}_T \frac{\lambda_o f_{11}(\mu_r f_{22}+f_{23})}{\mu_r f_{14}+f_{15}} - f_{24}}{\frac{2}{3}(\mu_r f_{25}+f_{26})}, \tag{C.14a}$$

$$\mathcal{Q}_N = \frac{C_{aE}}{c^2}\left[-(-c+\alpha Q_1')^2 - \left(-c+\alpha\frac{Q_1}{\lambda_o}\right)^2 - 2\beta^2/\varepsilon_r\right], \tag{C.14b}$$

$$\mathcal{Q}_T = \frac{C_{aE}}{c^2}\left[(-c+\alpha Q_1')\left(-c+\alpha\frac{Q_1}{\lambda_o}\right) + \beta^2/\varepsilon_r\right], \tag{C.14c}$$

where the electric capillary number is $C_{aE} = \frac{\epsilon_e r_0 E_0^2}{\gamma_0}$.

APPENDIX D

INTEGRALS IN THE SPHEROIDAL VESICLE MODEL

The functions $f_{11}(\xi_o) - f_{15}(\xi_o)$ are given by

$$f_{11} = \int \frac{\eta G_3(\eta)}{\xi_o^2 - \eta^2} d\eta, \tag{D.1}$$

$$f_{12} = \frac{1}{\xi_o^2 - 1} \int G_3(\eta) \left(\frac{2\eta G_3'(\eta)}{(\xi_o^2 - \eta^2)^2} + \frac{G_3''(\eta)}{\xi_o^2 - \eta^2} \right) d\eta, \tag{D.2}$$

$$f_{13} = \frac{G_3' G_5'' - G_5' G_3''}{2N} f_{11}, \tag{D.3}$$

$$f_{14} = -\xi_o H_3' \int \frac{\eta G_3(\eta)}{(\xi_o^2 - \eta^2)^2} d\eta + \frac{H_3''}{2} f_{11}, \tag{D.4}$$

$$f_{15} = \xi_o H_3' \int \frac{\eta G_3(\eta)}{(\xi_o^2 - \eta^2)^2} d\eta - \frac{(G_3 G_5'' - G_5 G_3'') H_3'}{2N} f_{11}, \tag{D.5}$$

where $N \equiv G_3(\xi_o) G_5'(\xi_o) - G_3'(\xi_o) G_5(\xi_o)$.

Furthermore, the functions $f_{21}(\xi_o) - f_{26}(\xi_o)$ are given by

$$f_{21} = \frac{\xi_o^2}{2} \int \frac{(3\eta^2 - 1)(\eta^2 - 1)}{\xi_o^2 - \eta^2} d\eta, \tag{D.6}$$

$$f_{22} = -H_3' \int \frac{(1 - 3\eta^2)(2\eta^4 + \xi_o^2 - 3\xi_o^2 \eta^2)}{(\xi_o^2 - \eta^2)^2} d\eta + 3 H_3 \xi_o \int \frac{1 - 3\eta^2}{\xi_o^2 - \eta^2} d\eta, \tag{D.7}$$

$$f_{23} = -\frac{49}{30N} G_3 H_3' (1 - 3\xi_o^2) + H_3' \int \frac{(1 - 3\eta^2)(2\eta^4 + \xi_o^2 - 3\xi_o^2 \eta^2)}{(\xi_o^2 - \eta^2)^2} d\eta, \tag{D.8}$$

$$f_{24} = \frac{1}{c} \left[\xi_o (\xi_o^2 - 1)^{1/2} \int \frac{(3\eta^2 - 1)}{(\xi_o^2 - \eta^2)^{3/2}} d\eta + \frac{\xi_o}{(\xi_o^2 - 1)^{1/2}} \int \frac{(3\eta^2 - 1)}{(\xi_o^2 - \eta^2)^{1/2}} d\eta \right], \tag{D.9}$$

$$f_{25} = -\frac{\xi_o}{\xi_o^2 - 1} \int \frac{(1 - 3\eta^2)(2\xi_o^2 - \eta^2 - 1) G_3'(\eta)}{(\xi_o^2 - \eta^2)^2} d\eta + 3\xi_o \int \frac{1 - 3\eta^2}{\xi_o^2 - \eta^2} d\eta - \frac{(\mu_r - 1) f_{12} + f_{13}}{\mu_r f_{14} + f_{15}} f_{22}, \tag{D.10}$$

$$f_{26} = \frac{\xi_o}{\xi_o^2 - 1} \int \frac{(1 - 3\eta^2)(2\xi_o^2 - \eta^2 - 1) G_3'(\eta)}{(\xi_o^2 - \eta^2)^2} d\eta - \frac{49}{30N} (1 - 3\xi_o^2) G_3' - \frac{(\mu_r - 1) f_{12} + f_{13}}{\mu_r f_{14} + f_{15}} f_{22}, \tag{D.11}$$

$$f_\kappa = \frac{-72 + 106\xi_o^2 - 225\xi_o^4 + 135\xi_o^6 + 45\xi_o^4 (4 - 3\xi_o^2) \sqrt{\xi_o^2 - 1} \csc^{-1}(\xi_o)}{15 c^3 \xi_o^3 (\xi_o^2 - 1)^2}. \tag{D.12}$$

The functions $f_{11}(\lambda_o) - f_{15}(\lambda_o)$ in are given by

$$f_{11} = \int \frac{\eta G_3(\eta)}{\lambda_o^2+\eta^2} d\eta, \tag{D.13}$$

$$f_{12} = \frac{1}{\lambda_o^2+1}\int G_3(\eta)\left(\frac{-2\eta G_3'(\eta)}{(\lambda_o^2+\eta^2)^2} + \frac{G_3''(\eta)}{\lambda_o^2+\eta^2}\right) d\eta, \tag{D.14}$$

$$f_{13} = \frac{G_3'G_5'' - G_5'G_3''}{2N} f_{11}, \tag{D.15}$$

$$f_{14} = \lambda_o H_3' \int \frac{\eta G_3(\eta)}{(\lambda_o^2+\eta^2)^2} d\eta - \frac{H_3''}{2} f_{11}, \tag{D.16}$$

$$f_{15} = -\lambda_o H_3' \int \frac{\eta G_3(\eta)}{(\lambda_o^2+\eta^2)^2} d\eta + \frac{(G_3G_5'' - G_5G_3'')H_3'}{2N} f_{11}, \tag{D.17}$$

where $N \equiv G_3(\lambda_o)G_5'(\lambda_o) - G_3'(\lambda_o)G_5(\lambda_o)$.

Furthermore, the functions $f_{21}(\lambda_o) - f_{26}(\lambda_o)$ are given by

$$f_{21} = \frac{\lambda_o^2}{2}\int \frac{(3\eta^2-1)(\eta^2-1)}{\lambda_o^2+\eta^2} d\eta, \tag{D.18}$$

$$f_{22} = H_3' \int \frac{(3\eta^2-1)(\lambda_o^2 - 3\lambda_o^2\eta^2 - 2\eta^4)}{(\lambda_o^2+\eta^2)^2} d\eta + 3\lambda_o H_3 \int \frac{3\eta^2-1}{\lambda_o^2+\eta^2} d\eta \tag{D.19}$$

$$f_{23} = -H_3' \int \frac{(3\eta^2-1)(\lambda_o^2 - 3\lambda_o^2\eta^2 - 2\eta^4)}{(\lambda_o^2+\eta^2)^2} d\eta + \frac{49}{30N}(1+3\lambda_o^2) g_3 H_3', \tag{D.20}$$

$$f_{24} = \frac{1}{c}\left[\lambda_o(\lambda_o^2+1)^{1/2}\int \frac{(1-3\eta^2)}{(\lambda_o^2+\eta^2)^{3/2}} d\eta + \frac{\lambda_o}{(\lambda_o^2+1)^{1/2}}\int \frac{(1-3\eta^2)}{(\lambda_o^2+\eta^2)^{1/2}} d\eta\right], \tag{D.21}$$

$$f_{25} = \frac{\lambda_o}{\lambda_o^2+1}\int \frac{(3\eta^2-1)(2\lambda_o^2+\eta^2+1)G_3'(\eta)}{(\lambda_o^2+\eta^2)^2} d\eta + 3\lambda_o \int \frac{3\eta^2-1}{\lambda_o^2+\eta^2} d\eta + \frac{(\mu_r-1)f_{12}+f_{13}}{\mu_r f_{14}+f_{15}} f_{22}, \tag{D.22}$$

$$f_{26} = -\frac{\lambda_o}{\lambda_o^2+1}\int \frac{(3\eta^2-1)(2\lambda_o^2+\eta^2+1)G_3'(\eta)}{(\lambda_o^2+\eta^2)^2} d\eta + \frac{49}{30N}(1+3\lambda_o^2) g_3' + \frac{(\mu_r-1)f_{12}+f_{13}}{\mu_r f_{14}+f_{15}} f_{23}, \tag{D.23}$$

$$f_\kappa = \frac{72 + 106\lambda_o^2 + 225\lambda_o^4 + 135\lambda_o^6 - 45\lambda_o^4(4+3\lambda_o^2)\sqrt{\lambda_o^2+1}\coth^{-1}(\sqrt{\lambda_o^2+1})}{15c^3\lambda_o^3(\lambda_o^2+1)^2}. \tag{D.24}$$

APPENDIX E

TRANSMEMBRANE POTENTIAL

The electric potential coefficients $\beta_e,\ \alpha_m,\ \beta_m,\ \alpha_i$ are obtained from the boundary conditions at $\xi = \xi_e$ and $\xi = \xi_i$ (see Figure 4.1):

1. Continuity of the potential:

$$\phi_e(\xi_e) = \phi_m(\xi_e), \quad \phi_m(\xi_i) = \phi_i(\xi_i), \tag{E.1}$$

2. Continuity of the normal component of the complex current density (4.9):

$$-\frac{K_e}{h_\xi}\frac{\partial \phi_e}{\partial \xi}\bigg|_{\xi_e} = -\frac{K_m}{h_\xi}\frac{\partial \phi_m}{\partial \xi}\bigg|_{\xi_e}, \quad -\frac{K_m}{h_\xi}\frac{\partial \phi_m}{\partial \xi}\bigg|_{\xi_i} = -\frac{K_i}{h_\xi}\frac{\partial \phi_i}{\partial \xi}\bigg|_{\xi_i}. \tag{E.2}$$

Condition 1 is justified because the normal component of the electric field must be bounded [65, 49]. The remaining electric potential coefficients are given by:

$$\alpha_i = \frac{cK_eK_m\left(\xi_iQ_i' - Q_i\right)\left(Q_e - \xi_eQ_e'\right)}{D(\omega)}, \tag{E.3}$$

$$\alpha_m = \frac{cK_e\left(\xi_eQ_e' - Q_e\right)\left(K_iQ_i - K_m\xi_iQ_i'\right)}{D(\omega)}, \tag{E.4}$$

$$\beta_m = \frac{c\xi_iK_e\left(K_i - K_m\right)\left(Q_e - \xi_eQ_e'\right)}{D(\omega)}, \tag{E.5}$$

$$\begin{aligned}\beta_e = {} & \frac{c\xi_iK_e\left(K_i - K_m\right)Q_e}{D(\omega)} \\ & + \frac{c\xi_e\left(K_i(K_m - K_e)Q_i + K_m\xi_i((K_m - K_i)Q_e' + (K_e - K_m)Q_i')\right)}{D(\omega)},\end{aligned} \tag{E.6}$$

where

$$\begin{aligned}D(\omega) = {} & K_e\xi_eQ_e'\left(-K_iQ_i + K_m\xi_iQ_i'\right) \\ & + Q_e\left(K_iK_mQ_i + (K_e - K_m)(K_i - K_m)\xi_iQ_e' - \xi_iQ_i'K_m^2\right),\end{aligned} \tag{E.7}$$

and $Q_e \equiv Q_1(\xi_e), Q_i \equiv Q_1(\xi_i), Q_e' \equiv Q_1'(\xi_e), Q_i' \equiv Q_1'(\xi_i)$.

APPENDIX F

MAXWELL STRESSES

To compute the Maxwell stress for a vesicle in an AC electric field (Chapter 4), note that the coefficients in Equation (4.17) (prolate) or Equation (4.24) (oblate) of the electric potential are complex valued. Substituting $\mathcal{E}_\xi = -\frac{\partial \phi}{\partial \xi}$, $\mathcal{E}_\xi^* = -\frac{\partial \phi^*}{\partial \xi}$, $\mathcal{E}_\eta = -\frac{\partial \phi}{\partial \eta}$, and $\mathcal{E}_\eta^* = -\frac{\partial \phi^*}{\partial \eta}$ into 4.22, and calculating the jump, one obtains

$$\begin{aligned}\llbracket \mathbf{S}_{\xi\xi} \rrbracket = \frac{1}{4c^2} \Bigg\{ & \frac{\eta^2 \left(\xi_o^2 - 1\right)}{\xi_o^2 - \eta^2} \left(c^2 - 2c\tau_3 Q_1' + \left(\tau_3^2 + \tau_4^2\right) \left(Q_1'\right)^2 \right) \\ & + \frac{\xi_o^2 \left(\eta^2 - 1\right)}{\xi_o^2 - \eta^2} \left(c^2 - \frac{2c\tau_3 Q_1}{\xi_o} + \left(\tau_3^2 + \tau_4^2\right) \left(\frac{Q_1}{\xi_o}\right)^2 \right) \\ & - \frac{\left(\tau_1^2 + \tau_2^2\right)}{\varepsilon_r} \left(\frac{\eta^2 \left(\xi_o^2 - 1\right)}{\xi_o^2 - \eta^2} + \frac{\xi_o^2 \left(\eta^2 - 1\right)}{\xi_o^2 - \eta^2} \right) \Bigg\}, \end{aligned} \tag{F.1}$$

and

$$\begin{aligned}\llbracket \mathbf{S}_{\xi\eta} \rrbracket = \frac{\eta}{2c^2} \frac{\sqrt{\left(\xi_o^2 - 1\right)\left(1 - \eta^2\right)}}{\xi_o^2 - \eta^2} \Big\{ & \left(c^2 \xi_o - c(Q_1 + \xi_o Q_1')\tau_3 + \left(\tau_3^2 + \tau_4^2\right) Q_1 Q_1' \right) \\ & - \left(\tau_1^2 + \tau_2^2\right) \xi_o / \varepsilon_r \Big\}, \end{aligned} \tag{F.2}$$

where $\tau_1 = \Re[\beta]$, $\tau_2 = \Im[\beta]$, $\tau_3 = \Re[\alpha]$, and $\tau_4 = \Im[\alpha]$. $\Re[\ ]$ and $\Im[\ ]$ denote the real and imaginary parts.

The equivalent equations in the oblate coordinates are

$$\begin{aligned}\llbracket \mathbf{S}_{\lambda\lambda} \rrbracket = \frac{1}{4c^2} \Bigg\{ & \frac{\eta^2 \left(\lambda_o^2 + 1\right)}{\lambda_o^2 + \eta^2} \left(c^2 - 2c\tau_3 Q_1' + \left(\tau_3^2 + \tau_4^2\right) \left(Q_1'\right)^2 \right) \\ & + \frac{\lambda_o^2 \left(\eta^2 - 1\right)}{\lambda_o^2 + \eta^2} \left(c^2 - \frac{2c\tau_3 Q_1}{\lambda_o} + \left(\tau_3^2 + \tau_4^2\right) \left(\frac{Q_1}{\lambda_o}\right)^2 \right) \\ & - \frac{\left(\tau_1^2 + \tau_2^2\right)}{\varepsilon_r} \left(\frac{\eta^2 \left(\lambda_o^2 + 1\right)}{\lambda_o^2 + \eta^2} + \frac{\lambda_o^2 \left(\eta^2 - 1\right)}{\lambda_o^2 + \eta^2} \right) \Bigg\}, \end{aligned} \tag{F.3}$$

and

$$[\![\mathbf{S}_{\lambda\eta}]\!] = \frac{\eta}{2c^2}\frac{\sqrt{\left(\lambda_o^2+1\right)\left(1-\eta^2\right)}}{\lambda_o^2+\eta^2}\left\{\left(c^2\lambda_o - c(Q_1+\lambda_o Q_1')\tau_3 + \left(\tau_3^2+\tau_4^2\right)Q_1Q_1'\right)\right.$$
$$\left. - \left(\tau_1^2+\tau_2^2\right)\lambda_o/\varepsilon_r\right\}. \tag{F.4}$$

APPENDIX G

ASYMPTOTIC ANALYSIS

The coefficients in Equation (4.30) are as follows:

$$A = (2+\sigma_r)^2 + 9\omega^2, \tag{G.1}$$

$$\begin{aligned} B = {} & 2\sigma_r^2(2+\sigma_r)^2 + \left(18\sigma_r^2 + C_m^2(\sigma_r-1)(2+\sigma_r)^2(5+2\sigma_r)\right. \\ & \left. +2C_m\sigma_r(\sigma_r+\sigma_r^2-2)\right)\omega^2, \end{aligned} \tag{G.2}$$

$$\begin{aligned} C = {} & -2\sigma_r^2(2+\sigma_r)^3\left(9Ca_E(19+13\sigma_r)+560(2+\sigma_r)(4+s_0)\right) - 71680C_m^2\omega^2 \\ & +\left(9Ca_E(2+\sigma_r)\left(-6\sigma_r^2(121+71\sigma_r)+C_m(\sigma_r-1)\sigma_r(2+\sigma_r)(130+107\sigma_r)\right.\right. \\ & \left.+C_m^2(60+23\sigma_r)(\sigma_r+\sigma_r^2-2)^2\right) + 280\left(-72\sigma_r^2(2+\sigma_r)^2(4+s_0)\right. \\ & \left.\left.+C_m^2\left(-64s_0-\sigma_r(4+\sigma_r)(4+\sigma_r(2+\sigma_r))(12+\sigma_r(6+\sigma_r))(4+s_0)\right)\right)\omega^2 \\ & -9\left(-711Ca_EC_m\sigma_r(\sigma_r+\sigma_r^2-2)+288\sigma_r^2\left(6Ca_E+35(4+s_0)\right)\right. \\ & \left.+5C_m^2(2+\sigma_r)^2(9Ca_E(\sigma_r-1)^2+112(2+\sigma_r)^2(4+s_0))\right)\omega^4 \\ & -22680C_m^2(2+\sigma_r)^2(4+s_0)\omega^6, \end{aligned} \tag{G.3}$$

$$\begin{aligned} G = {} & 3Ca_E\left((2+\sigma_r)^2+9\omega^2\right)\left(2\sigma_r^2(2+\sigma_r)^2+\left(18\sigma_r^2+C_m^2(\sigma_r-1)(2+\sigma_r)^2(5+2\sigma_r)\right.\right. \\ & \left.\left.+2C_m\sigma_r(\sigma_r+\sigma_r^2-2)\right)\omega^2\right). \end{aligned} \tag{G.4}$$

APPENDIX H

IMMERSED INTERFACE CONDITIONS

Here, the interface conditions needed for an immersed boundary in three-dimensional axisymmetric coordinates are derived. Recall the local coordinates,

$$\xi = (r - r^*)\cos\theta + (z - z^*)\sin\theta, \tag{H.1}$$

$$\eta = -(r - r^*)\sin\theta + (z - z^*)\cos\theta, \tag{H.2}$$

and the parametric form of the interface $\xi = \chi(\eta)$.

One can differentiate the continuity of potential at the interface

$$\phi^+ = \phi^- \tag{H.3}$$

with respect to η to obtain $\phi^+_\xi \chi' + \phi^+_\eta = \phi^-_\xi \chi' + \phi^-_\eta$, or

$$[\![\phi_\xi]\!]\chi' + [\![\phi_\eta]\!] = 0. \tag{H.4}$$

Differentiating again with respect to η yields,

$$[\![\phi_{\xi\xi}]\!](\chi')^2 + 2[\![\phi_{\xi\eta}]\!]\chi' + [\![\phi_\xi]\!]\chi'' + [\![\phi_{\eta\eta}]\!] = 0. \tag{H.5}$$

Evaluating (H.4) and (H.5) at $\eta = 0$ gives

$$[\![\phi_\eta]\!] = 0, \tag{H.6}$$

$$[\![\phi_\xi]\!]\chi'' + [\![\phi_{\eta\eta}]\!] = 0. \tag{H.7}$$

At a point $(\chi(\eta), \eta)$ of the interface, the unit normal vector $\boldsymbol{n} = (1, -\chi')$ and the normal derivative of the potential $\frac{\partial\phi}{\partial n} = \frac{\phi_\xi - \phi_\eta\chi'}{\sqrt{1+(\chi')^2}}$. The jump in the normal derivative of the potential becomes

$$\sigma^+\left(\phi^+_\xi - \phi^+_\eta\chi'\right) = \sigma^-\left(\phi^-_\xi - \phi^-_\eta\chi'\right). \tag{H.8}$$

Differentiating with respect to η gives

$$[\![\sigma\left(\phi_{\xi\xi}\chi' + \phi_{\xi\eta} - \phi_\eta\chi'' - \phi_{\xi\eta}(\chi')^2 - \phi_{\eta\eta}\chi'\right)]\!] = 0. \tag{H.9}$$

Evaluating (H.8) and (H.9) gives

$$[\![\sigma\phi_\xi]\!] = 0, \tag{H.10}$$

$$[\![\sigma\left(\phi_{\xi\eta} - \phi_\eta\chi''\right)]\!] = 0. \tag{H.11}$$

Summarizing the interface conditions, one gets

$$\phi^+ = \phi^-, \tag{H.12}$$

$$\phi^+_\xi = \rho\phi^-_\xi, \tag{H.13}$$

$$\phi^+_\eta = \phi^-_\eta, \tag{H.14}$$

$$\phi^+_{\xi\xi} = \rho\phi^-_{\xi\xi} - (1-\rho)\chi''\phi^-_\xi + (\rho-1)\phi^-_{\eta\eta} + (1-\rho)\frac{\sin\theta}{r}\phi^-_\eta, \tag{H.15}$$

$$\phi^+_{\eta\eta} = \phi^-_{\eta\eta} + (1-\rho)\chi''\phi^-_\xi, \tag{H.16}$$

$$\phi^+_{\xi\eta} = \rho\phi^-_{\xi\eta} + (1-\rho)\phi^-_\eta\chi'', \tag{H.17}$$

where $\rho = \frac{1}{\sigma_r}$. Equation (H.15) is derived from the differential equation. Denoting $\partial_x \equiv \frac{\partial}{\partial x}$, one can write

$$\begin{aligned}
\partial_r &= \cos\theta\partial_\xi - \sin\theta\partial_\eta, \\
\partial_z &= \sin\theta\partial_\xi + \cos\theta\partial_\eta, \\
\partial_{rr} &= \cos^2\theta\partial_{\xi\xi} - 2\sin\theta\cos\theta\partial\xi\eta + \sin^2\theta\partial_{\eta\eta}, \\
\partial_{zz} &= \sin^2\theta\partial_{\xi\xi} + 2\sin\theta\cos\theta\partial\xi\eta + \cos^2\theta\partial_{\eta\eta},
\end{aligned}$$

and the governing PDE for the potential becomes

$$\phi_{\xi\xi} + \frac{\cos\theta\phi_\xi - \sin\theta\phi_\eta}{r} + \phi_{\eta\eta} = 0. \tag{H.18}$$

Using (H.18), and expressing the potential $\phi^+_{\xi\xi}$ in terms of $\phi^-_{\xi\xi}$ gives (H.15).

The local truncation error T_{ij} of the finite difference in (5.18) is

$$\begin{aligned} T_{ij} =&\gamma_1\phi(\xi_1,\eta_1)+\gamma_2\phi(\xi_2,\eta_2)+\gamma_3\phi(\xi_3,\eta_3)+\gamma_4\phi(\xi_4,\eta_4)+\gamma_5\phi(\xi_5,\eta_5)\\ &+\gamma_6\phi(\xi_6,\eta_6)-C_{ij}. \end{aligned} \tag{H.19}$$

Expanding all terms $\phi(\xi_k,\eta_k)$ about $(0,0)$ yields

$$\phi(\xi_k,\eta_k)=\phi^\pm+\xi_k\phi^\pm_\xi+\eta_k\phi^\pm_\eta+\frac{1}{2}\xi_k^2\phi^\pm_{\xi\xi}+\xi_k\eta_k\phi^\pm_{\xi\eta}+\frac{1}{2}\eta_k^2\phi^\pm_{\eta\eta}+\mathcal{O}(h^3). \tag{H.20}$$

Substituting (H.20) into T_{ij} gives

$$\begin{aligned} T_{ij} =&a_1\phi^-+a_2\phi^+ +a_3\phi^-_\xi+a_4\phi^+_\xi+a_5\phi^-_\eta+a_6\phi^+_\eta+a_7\phi^-_{\xi\xi}+a_8\phi^+_{\xi\xi}\\ &+a_9\phi^-_{\eta\eta}+a_{10}\phi^+_{\eta\eta}+a_{11}\phi^-_{\xi\eta}+a_{12}\phi^+_{\xi\eta}, \end{aligned} \tag{H.21}$$

where

$$\begin{aligned} a_1&=\sum_{\vec{x}\in\Omega^-}\gamma_{ij}, \quad a_2=\sum_{\vec{x}\in\Omega^+}\gamma_{ij}\\ a_3&=\sum_{\vec{x}\in\Omega^-}\gamma_{ij}\xi_i, \quad a_4=\sum_{\vec{x}\in\Omega^+}\gamma_{ij}\xi_i\\ a_5&=\sum_{\vec{x}\in\Omega^-}\gamma_{ij}\eta_j, \quad a_6=\sum_{\vec{x}\in\Omega^+}\gamma_{ij}\eta_j\\ a_7&=\sum_{\vec{x}\in\Omega^-}\gamma_{ij}\frac{\xi_i^2}{2}, \quad a_8=\sum_{\vec{x}\in\Omega^+}\gamma_{ij}\frac{\xi_i^2}{2}\\ a_9&=\sum_{\vec{x}\in\Omega^-}\gamma_{ij}\frac{\eta_j^2}{2}, \quad a_{10}=\sum_{\vec{x}\in\Omega^+}\gamma_{ij}\frac{\eta_j^2}{2}\\ a_{11}&=\sum_{\vec{x}\in\Omega^-}\gamma_{ij}\xi_i\eta_j, \quad a_{12}=\sum_{\vec{x}\in\Omega^+}\gamma_{ij}\xi_i\eta_j. \end{aligned}$$

Substituting (H.12)-(H.17) into (H.21), then requiring that the coefficients of the terms $\phi^-,\ \phi^-_\xi,\ \phi^-_\eta,\ \phi^-_{\xi\xi},\ \phi^-_{\eta\eta},\ \phi^-_{\xi\eta}$, all vanish one obtains the system of linear equations for γ_k.

For the more general case, $w \neq 0$ $v \neq 0$, the interface conditions read

$$\begin{aligned}
\phi^+ &= \phi^- + w, && \text{(H.22)}\\
\phi^+_\xi &= \rho\phi^-_\xi + \frac{v}{\beta^+}, && \text{(H.23)}\\
\phi^+_\eta &= \phi^-_\eta + w', && \text{(H.24)}\\
\phi^+_{\xi\xi} &= \rho\phi^-_{\xi\xi} - (1-\rho)\chi''\phi^-_\xi + (\rho-1)\phi^-_{\eta\eta} + (1-\rho)\frac{\sin\theta}{x}\phi^-_\eta && \text{(H.25)}\\
&\quad + \frac{v\chi''}{\beta^+} - w'' - \frac{v\cos\theta}{x} + \frac{w'\sin\theta}{x}, && \text{(H.26)}\\
\phi^+_{\eta\eta} &= \phi^-_{\eta\eta} + (1-\rho)\chi''\phi^-_\xi + w'', && \text{(H.27)}\\
\phi^+_{\xi\eta} &= \rho\phi^-_{\xi\eta} + (1-\rho)\phi^-_\eta\chi'' + \frac{v'}{\beta^+}, && \text{(H.28)}
\end{aligned}$$

Substituting the interface conditions above into the truncation error (H.21), one obtains

$$\begin{aligned}
T =& (a_1+a_2)\phi^- + \left[a_3 + \rho a_4 + a_{10}(1-\rho)\chi'' - a_8(1-\rho)\chi''\right]\phi^-_\xi && \text{(H.29)}\\
&+ \left[a_5 + a_6 + a_{12}(1-\rho)\chi'' + a_8(1-\rho)\frac{\sin\theta}{x}\right]\phi^-_\eta && \text{(H.30)}\\
&+ \left[a_7 + \rho a_8\right]\phi^-_{\xi\xi} + \left[a_9 + a_{10} + a_8(\rho-1)\right]\phi^-_{\eta\eta} + \left[a_{11} + \rho a_{12}\right]\phi^-_{\xi\eta} && \text{(H.31)}\\
&- C_{ij} + \hat{T}_{ij}, && \text{(H.32)}
\end{aligned}$$

where the correction term $C_{ij} = \hat{T}_{ij}$ and

$$\begin{aligned}
\hat{T}_{ij} &= a_2 w + \left[a_6 + a_{12}\chi'' + a_8\frac{\sin\theta}{x}\right]w' + \left[a_{10} - a_8\right]w''\\
&\quad + \left[\frac{a_4}{\beta^+} + (a_8 - a_{10})\frac{\chi''}{\beta^+} - a_8\frac{\cos\theta}{\beta^+ x}\right]v + a_{12}\frac{v'}{\beta^+}, && \text{(H.33)}
\end{aligned}$$

The corresponding system of equations for the coefficients γ_k becomes is the same as in the case of natural interface conditions ($w = 0,\ v = 0$).

Note that it is not necessary to use local coordinates with directions normal and tangential to the interface. Alternatively, one could use Mayo's technique, where the jumps are found along the grid lines (see Figure H.1).

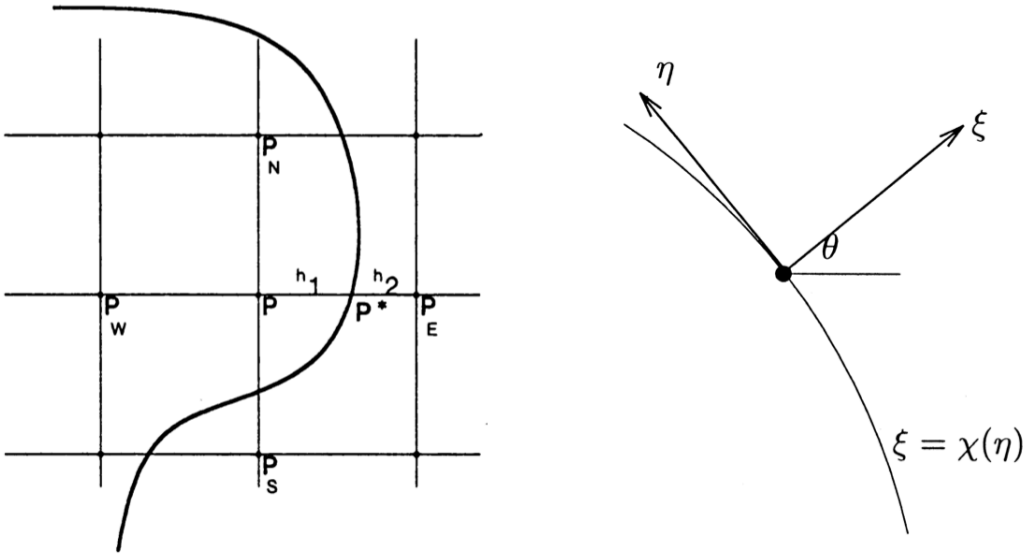

Figure H.1 Computation of the jumps using Mayo's technique [97] (left) or the local coordinates [82] (right).

APPENDIX I

DERIVATION OF THE GOVERNING EQUATION FOR THE PROLATE SHAPE FUNCTION WITH BILAYER STRUCTURE

Recall the stream function solutions,

$$\psi_e = \left[A_3^1 H_1(\xi) + A_3^3 H_3(\xi)\right] G_3(\eta), \tag{I.1}$$

$$\psi_i = \left[B_3^3 G_3(\xi) + B_3^5 G_5(\xi)\right] G_3(\eta), \tag{I.2}$$

where the coefficients $A_3^1 - B_3^5$ are determined from the interfacial boundary conditions at $\xi = \xi_0$. Additionally, the governing equation for the vesicle shape, $\frac{d\xi_0}{dt}$ must also be determined.

There are five unknowns to be determined. As a result, five equations are needed to close the system.

Eq. 7.2 yields

$$A_3^1 = A_3^3 H_3 - M\xi_0', \tag{I.3}$$

$$B_3^3 = \frac{M\xi_0' - B_3^5 G_5}{G_3}. \tag{I.4}$$

Substituting A_3^1 and B_3^3 into Eq. 7.3 gives

$$A_3^3 = \frac{-\varepsilon_e c \mathcal{Q}_T^{\Delta} f_{11} + \mu_i f_{15} B_3^5 - \mu_i \left[(\mu_r - 1) f_{12} - f_{13}\right] M\xi_0'}{\mu_i \mu_r f_{17}}, \tag{I.5}$$

where

$$f_{12} = \frac{1}{\xi_0^2 - 1} \int \left(\frac{2\eta G_3'(\eta) G_3(\eta)}{(\xi_0^2 - \eta^2)^2} + \frac{G_3''(\eta) G_3(\eta)}{\xi_0^2 - \eta^2} \right) d\eta, \tag{I.6}$$

$$f_{13} = \frac{\xi_0 G_3'}{G_3} \int \frac{\eta G_3(\eta)}{(\xi_0^2 - \eta^2)^2} d\eta - \frac{G_3''}{2G_3} f_{11}, \tag{I.7}$$

$$f_{15} = \frac{\xi_0 (G_3 G_5' - G_3' G_5)}{G_3} \int \frac{\eta G_3(\eta)}{(\xi_0^2 - \eta^2)^2} d\eta - \frac{G_3 G_5'' - G_3'' G_5}{2G_3} f_{11}, \tag{I.8}$$

$$f_{17} = \xi_0 H_3' \int \frac{\eta G_3(\eta)}{(\xi_0^2 - \eta^2)^2} d\eta - \frac{H_3''}{2} f_{11}, \tag{I.9}$$

and

$$\mathcal{Q}_T^{\Delta} = \left(-cE_0 + \alpha Q_1'\right)\left(-cE_0\xi_0 + \alpha Q_1\right) - \xi_0\beta^2/\varepsilon_r. \tag{I.10}$$

Substituting (I.3)-(I.5) into (7.4) gives

$$B_3^5 = \frac{T_2 M\xi_0' + T_3}{T_1}. \tag{I.11}$$

where

$$T_1 = \left(\frac{f_{15}f_{21}}{f_{17}} + f_{24}\right) - \frac{\tilde{b}c}{\mu_i}\left(f_{28} - \frac{f_{15}f_{26}}{\mu_r f_{17}}\right), \tag{I.12}$$

$$T_2 = \frac{\tilde{b}c}{\mu_i}\left(f_{27} + \frac{\left[(\mu_r - 1)f_{12} - f_{13}\right]f_{26}}{\mu_r f_{17}}\right) - \left((\mu_r + 1)f_{22} + f_{23} - \frac{\left[(\mu_r - 1)f_{12} - f_{13}\right]f_{21}}{f_{17}}\right), \tag{I.13}$$

$$T_3 = \frac{\varepsilon_e c}{\mu_i}\left(\frac{\tilde{b}c\mathcal{Q}_T^{\Delta} f_{11}f_{26}}{\mu_i\mu_r f_{17}} + \frac{\mathcal{Q}_T^{\Delta} f_{11}f_{21}}{f_{17}} - \mathcal{Q}_T^{\Sigma} f_{11}\right), \tag{I.14}$$

and

$$\mathcal{Q}_T^{\Sigma} = \left(-cE_0 + \alpha Q_1'\right)\left(-cE_0\xi_0 + \alpha Q_1\right) + \xi_0\beta^2/\varepsilon_r. \tag{I.15}$$

The functions $f_{21} - f_{28}$ are given by

$$f_{21} = \xi_0 H_3' \int \frac{\eta G_3(\eta)}{(\xi_0^2 - \eta^2)^2} d\eta - \frac{H_3''}{2} f_{11}, \tag{I.16}$$

$$f_{22} = f_{12}, \tag{I.17}$$

$$f_{23} = f_{13}, \tag{I.18}$$

$$f_{24} = f_{15}, \tag{I.19}$$

$$f_{25} = \int \frac{\eta G_3(\eta)}{\sqrt{\xi_0^2 - \eta^2}} d\eta, \tag{I.20}$$

$$f_{26} = \frac{H_3'}{\sqrt{\xi_0^2 - 1}} f_{25}, \tag{I.21}$$

$$f_{27} = \frac{G_3'}{G_3\sqrt{\xi_0^2 - 1}} f_{25}, \tag{I.22}$$

$$f_{28} = \frac{(G_3 G_5' - G_3' G_5)}{G_3\sqrt{\xi_0^2 - 1}} f_{25}. \tag{I.23}$$

Substituting (I.3)-(I.5), (I.11) into (7.5) gives the governing equation for the dynamics of vesicle electro-deformation with discontinuous tangential velocities (7.6).

The functions $f_{32} - f_{35}$ are

$$f_{32} = H_3' \int \frac{(2\eta^4 + \xi_0^2 - 3\xi_0^2\eta^2)(1 - 3\eta^2)}{(\xi_0^2 - \eta^2)^2} d\eta - 3\xi_0 H_3 \int \frac{1 - 3\eta^2}{\xi_0^2 - \eta^2} d\eta, \tag{I.24}$$

$$f_{33} = 3\xi_0 \int \frac{1 - 3\eta^2}{\xi_0^2 - \eta^2} d\eta - \frac{\xi_0}{\xi_0^2 - 1} \int \frac{(2\xi_0^2 - \eta^2 - 1)(1 - 3\eta^2) G_3'(\eta)}{(\xi_0^2 - \eta^2)^2} d\eta, \tag{I.25}$$

$$\begin{aligned} f_{34} = &-\frac{G_3'}{G_3} \int \frac{(2\eta^4 + \xi_0^2 - 3\xi_0^2\eta^2)(1 - 3\eta^2)}{(\xi_0^2 - \eta^2)^2} d\eta \\ &+ \frac{\xi_0}{\xi_0^2 - 1} \int \frac{(2\xi_0^2 - \eta^2 - 1)(1 - 3\eta^2) G_3'(\eta)}{(\xi_0^2 - \eta^2)^2} d\eta, \end{aligned} \tag{I.26}$$

$$f_{35} = \frac{49}{30}(1 - 3\xi_0^2) - \frac{(G_3 G_5' - G_3' G_5)}{G_3} \int \frac{(2\eta^4 + \xi_0^2 - 3\xi_0^2\eta^2)(1 - 3\eta^2)}{(\xi_0^2 - \eta^2)^2} d\eta. \tag{I.27}$$

BIBLIOGRAPHY

[1] O. O. Ajayi. A note on Taylor's electrohydrodynamic theory. *Proc. R. Soc. Lond. A*, 364:499–507, 1978.

[2] R. S. Allan and S. G. Mason. Particle behaviour in shear and electric fields. I. Deformation and burst of fluid drops. *Proc. R. Soc. Lond. A*, 267:45–61, 1962.

[3] B. Ambravaneswaran, E. D. Wilkes, and O. A. Basaran. Drop formation from a capillary tube: Comparison of one-dimensional and two-dimensional analyses and occurrence of satellite drops. *Phys. Fluids*, 14:2606, 2002.

[4] S. L. Anna and H. C. Mayer. Microscale tipstreaming in a microfluidic flow focusing device. *Phys. Fluids*, 18:121512, 2006.

[5] K. Antonova, V. Vitkova, and M. D. Mitov. Deformation of giant vesicles in ac electric fields –dependence of the prolate-to-oblate transition frequency on vesicle radius. *Europhys. Letters*, 89:38004, 2010.

[6] S. Aranda, K. A. Riske, R. Lipowsky, and R. Dimova. Morphological transitions of vesicles induced by alternating electric fields. *Biophys. J.: Biophys. Lett.*, page L19, 2008.

[7] O. A. Basaran. Small-scale free surface flows with beeakup: Drop formation and emerging applications. *AIChE Journal*, 48(9):1842, 2002.

[8] O. A. Basaran and L. E. Scriven. Axisymmetric shapes and stability of charged drops in an external electric field. *Phys. Fluids*, 1:799, 1989.

[9] T. Beale and A. T. Layton. A velocity decomposition approach for moving interfaces in viscous fluids. *J. Comput. Phys.*, 228:3358–3367, 2009.

[10] N. Bentenitis and S. Krause. Droplet deformation in DC electric fields: The extended leaky dielectric model. *Langmuir*, 21:6194–6209, 2005.

[11] J. D. Berry, M. R. Davidson, and D. J. E. Harvie. A multiphase electrokinetic flow model for electrolytes with liquid/liquid interfaces. *J. Comput. Phys.*, 251:209–222, 2013.

[12] R. P. Beyer. A computational model of the cochlea using the immersed boundary method. *J. Comput. Phys.*, 98:145–162, 1992.

[13] E. Bjorklund. The level set method applied to droplet dynamics in the presence of an electric field. *Comp. Fluids*, 38:358–369, 2009.

[14] J. Blawzdziewicz, V. Cristini, and M. Loewenberg. Near-contact motion of surfactant-covered spherical drops: Iodic surfactant. *J. Colloid Int. Sci.*, 211:355–366, 1999.

[15] M. R. Booty and M. Siegel. Steady deformation and tip-streaming of a slender bubble with surfactant in extensional flow. *J. Fluid Mech.*, 544:243–275, 2005.

[16] P. R. Brazier-Smith. Stability and shape of isolated and pairs of water drops in an electric field. *Phys. Fluids*, 14:1, 1971.

[17] P. R. Brazier-Smith, S. G. Jennings, and J. Latham. An investigation of the behaviour of drops and drop-pairs subjected to strong electric forces. *Proc. R. Soc. Lond. A*, 325:363–376, 1971.

[18] V. Brisson and R. D. Tilton. Self-assembly and two-dimensional patterning of cell arrays by electrophoretic deposition. *Biotech. Bioeng.*, 77:290–295, 2002.

[19] F. Brochard-Wyart, P. G. de Gennes, and O. Sandre. Transient pores in stretched vesicles: role of leak-out. *Physica A*, 278:32–51, 2000.

[20] G. Bryant and J. Wolfe. Electromechanical stresses produced in the plasma membranes of suspended cells by applied electric fields. *J. Membr. Biol.*, 96:129–139, 2008.

[21] A. Castellanos, editor. *Electrohydrodynamics*, volume 380 of *CISM International Center for Mechanical Sciences*. Springer, 1998.

[22] S. Chandrasekhar. *Hydrodynamic and hydromagnetic stability*. Dover, 1981.

[23] D. C. Chang, B. M. Chassey, J. A. Saunders, and A. E. Sowers. *Guide to electroporation and electrofusion*. Academic Press, 1992.

[24] R. T. Collins, J. J. Jones, M. T. Harris, and O. A. Basaran. Electrohydrodynamic tip streaming and emission of charged drops from liquid cones. *Nat. Phys.*, 4:149–154, 2008.

[25] R. T. Collins, K. Sambath, M. T. Harris, and O. A. Basaran. Scaling laws for the disintegration of electrified drops. *Proc. Natl. Acad. Sci. U.S.A.*, 110:4905–4910, 2013.

[26] Y. Cui and N. R. Gupta. Surfactant effects on drop formation in co-flowing fluid streams. *Colloids and Surfaces A: Physiochem. Eng. Aspects*, 393:111, 2012.

[27] G. Dassios, M. Hadjinicolaou, F. A. Coutelieris, and A. C. Payatakes. Stokes flow in spheroidal particle-in-cell models with Happel and Kuwabara boundary conditions. *Int. J. Eng. Sci.*, 33:1465–1490, 1995.

[28] G. Dassios, M. Hadjinicolaou, and A. C. Payatakes. Generalized eigenfunctions and complete semi separable solutions for stokes flow in spheroidal coordinates. *Quat. App. Math.*, 52:157–191, 1994.

[29] P. M. de Zeeuw. Matrix-dependent prolongations and restrictions in a blackbox multigrid solver. *J. Comput. App. Math.*, 33:1–27, 1990.

[30] R. A. DeBruijn. Tipstreaming of drops in simple shear flows. *Chem. Engng. Sci.*, 48:277–284, 1993.

[31] M. A. Delong. *SOR as a preconditioner*. PhD thesis, University of Virginia, 1997.

[32] M. A. Delong and J. M. Ortega. SOR as a preconditioner. *App. Numer. Math.*, 18:431–440, 1995.

[33] M. A. Delong and J. M. Ortega. SOR as a preconditioner II. *App. Numer. Math.*, 26:465–481, 1998.

[34] W. K. den Otter and S. A. Shkulipa. Intermonolayer friction and surface shear viscosity of lipid bilayer membranes. *Biophys. J.*, 93:423–433, 2007.

[35] R. Dimova, C. Dietrich, A. Hadjiisky, K. Danov, and B. Pouligny. Falling ball viscosimetry of giant vesicle membranes: finite-size effects. *Eur. Phys. J. B*, 12:589, 1999.

[36] R. Dimova, K. A. Riske, S. Aranda, N. Bezlyepkina, R. L. Knorr, and R. Lipowsky. Giant vesicles in electric fields. *Soft Matter*, 3:817–827, 2007.

[37] N. Dubash and A. J. Mestel. Behavior of a conducting drop in a highly viscous fluid less conducting than that of the ambient fluid. *J. Fluid Mech.*, 581:469–493, 2007.

[38] C. D. Eggleton, Y. P. Pawar, and K. J. Stebe. Insoluble surfactants on a drop in an extensional flow: a generalization of the stagnated surface limit to deforming interfaces. *J. Fluid Mech.*, 385:79–99, 1999.

[39] L. P. Eisenhart. *A treatise on the differential geometry of curves and surfaces*. Dover, 1960.

[40] L. J. Fauci. Interaction of oscillating filaments–a computational study. *J. Comput. Phys.*, 86:294–313, 1990.

[41] J. Q. Feng. Electrohydrodynamic behavior of a drop subjected to a steady uniform electric field at finite electric Reynolds number. *Proc. Math. Phys. Eng. Sci.*, 455:2245–2269, 1999.

[42] J. Q. Feng. Steady axisymmetric motion of a small bubble in a tube with flowing liquid. *Proc. R. Soc. A*, 466:549–562, 2010.

[43] J. Q. Feng and T. C. Scott. A computational analysis of electrohydrodynamics of a leaky dielectric drop in an electric field. *J. Fluid Mech.*, 311:289–326, 1996.

[44] O. Ghazian, K. Adamiak, and G. S. P. Castle. Numerical simulation of electrically deformed droplets less conductive than ambient fluid. *Colloids and Surfaces A: Physicochem. Eng. Aspects*, 423:27–34, 2013.

[45] J. Gimsa and D. Wachner. A polarization model overcoming the geometric restrictions of the laplace solution for spheroidal cells: obtaining new equations for field-induced forces and transmembrane potential. *Biophys. J.*, 77:1316, 1999.

[46] M. Golzio, M. P. Rols, and J. Teissié. In vitro and in vivo electric field-mediated permeabilization, gene transfer, and expression. *Methods*, 33:126–135, 2004.

[47] M. Golzio, J. Teissié, and M.-P. Rols. Direct visualization at the single-cell level of electrically mediated gene delivery. *Proc. Natl. Acad. Sci. U.S.A.*, 99:1292–1297, 2002.

[48] A. Gothelf, L. M. Mir, and J. Gehl. Electrochemotherapy: Results of cancer treatment using enhanced delivery of bleomycin by electroporation. *Cancer Treat. Rev.*, 29:371–387, 2003.

[49] C. Grosse and H. P. Schwan. Cellular membrane potentials induced by alternating fields. *Biophys. J.*, 63:1632, 1992.

[50] N. R. Gupta, A. Nadim, H. Haj-Hariri, and A. Bohan. A numerical study of the effect of insoluble surfactants on the stability of a viscous drop translating in a Hele-Shaw cell. *J. of Colloid Int. Sci.*, 252:236, 2002.

[51] J.-W. Ha and S.-M. Yang. Effects of surfactant on the deformation and stability of a drop in a viscous fluid in an electric field. *J. Colloid Int. Sci.*, 175:369–385, 1995.

[52] J.-W. Ha and S.-M. Yang. Effect of nonionic surfactant on the deformation and breakup of a drop in an electric field. *J. Colloid Int. Sci.*, 206:195–204, 1998.

[53] J.-W. Ha and S.-M. Yang. Deformation and beeakup of Newtonian and non-Newtonian conducting drops in an electric field. *J. Fluid Mech.*, 405:131–156, 2000.

[54] J.-W. Ha and S.-M. Yang. Deformation and breakup of Newtonian and non-Newtonian conducting drops in an electric field. *J. Fluid Mech.*, 405:131–156, 2000.

[55] J.-W. Ha and S.-M. Yang. Electrohydrodynamics and electrorotation of a drop with fluid less conducting than that of the ambient fluid. *Phys. Fluids*, 12:764, 2000.

[56] W. Helfrich. Deformation of lipid bilayer spheres by electric fields. *Z. Naturforsch*, 29c:182–183, 1974.

[57] R. Heller, R. Gilbert, and M. J. Jaroszeski. Clinical applications of electrochemotherapy. *Adv. Drug Deliv. Rev.*, 35:119–129, 1999.

[58] M. R. Hossan, R. Dillon, A. K. Roy, and P. Dutta. Modeling and simulation of dielectrophoretic particle-particle interactions and assembly. *J. Colloid Int. Sci.*, 394:619–629, 2013.

[59] J.-P. Hsu, C.-Y. Lin, L.-H. Yeh, and S.-H. Lin. Influence of the shape of a polyelectrolyte on its electrophoretic behavior. *Soft Matter*, 8:9469, 2012.

[60] W.-F. Hu, Y. Kim, and M.-C. Lai. An immersed boundary method for simulating the dynamics of three-dimensional axisymmetric vesicles in Navier-Stokes flows. *J. Comput. Phys.*, 257:670–686, 2014.

[61] W.-F. Hu, M.-C. Lai, and Y.-N. Young. A hybrid immersed boundary and immersed interface method for electrohydrodynamic simulations. In preparation.

[62] J. Hua, L. K. Lim, and C.-H. Wang. Numerical simulation of deformation/motion of a drop suspended in viscous liquids under the influence of steady electric fields. *Phys. Fluids*, 20:113302, 2008.

[63] Y. Huang, K. L. Ewalt, M. Tirados, R. Haigis, A. Forster, D. Ackley, M. J. Heller, J. P. O'Connel, and M. Krihak. Electric manipulation of bioparticles and macromolecules on micro fabricated electrodes. *Anal. Chem.*, 73(7):1549–1559, 2001.

[64] H. Hyuga, K. Kinosita Jr., and N. Wakabayashi. Deformation of vesicles under the influence of strong electric fields. *Jpn. J. App. Phys.*, 30:1141–1148, 1991.

[65] H. Hyuga, K. Kinosita Jr., and N. Wakabayashi. Transient and steady-state deformations of a vesicle with an insulating membrane in response to step-function or alternating electric fields. *Jpn. J. App. Phys.*, 30:2649–2656, 1991.

[66] R. A. Jerry, A. S. Popel, and W. E. Brownell. Potential distribution for a spheroidal cell having a conductive membrane in an electric field. *IEEE Trans. Biomed. Eng.*, 43:970, 1996.

[67] F. Jin, N. R. Gupta, and K. J. Stebe. The detachment of a viscous drop in a viscous solution in the presence of a soluble surfactant. *Phys. Fluids*, 18:022103, 2006.

[68] D. M. Young Jr. *Iterative methods for solving partial difference equations of elliptic type*. PhD thesis, Harvard University, 1950.

[69] M. Kaga and T. Ohta. Shrinkage dynamics of a vesicle in surfactant solutions. *Eur. Phys. J. E*, 21:91–98, 2006.

[70] S. Kanazawa, Y. Takahashi, and Y. Nomoto. Emulsification and emulsification processes in liquid-liquid system by electrostatic atomization technique. *IEEE Trans. Ind. App.*, 44:1084, 2008.

[71] E. Karatekin, O. Sandre, and F. Brochard-Wyart. Transient pores in vesicles. *Polymer Int.*, 52:486–493, 2003.

[72] E. Karatekin, O. Sandre, H. Guitouni, N. Borghi, P.-H. Puech, and F. Brochard-Wyart. Cascades of transient pores in giant vesicles: line tension and transport. *Biophys. J.*, 84:1734–1749, March 2003.

[73] M. Klee and R. Plonsey. Finite difference solution for biopotentials of axially symmetric cells. *Biophys. J.*, 12:1661–1675, 1972.

[74] T. Kotnik and D. Miklavčič. Analytical description of transmembrane voltage induced by electric fields on spheroidal cells. *Biophys. J.*, 79:670–679, 2000.

[75] W. Krassowska and P. D. Filev. Modeling electroporation in a single cell. *Biophys. J.*, 92:404–417, 2011.

[76] M. Kummrow and W. Helfrich. Deformation of giant lipid vesicles by electric fields. *Phys. Rev. E*, 44:8356–8360, 1991.

[77] E. Lac and G. M. Homsy. Axisymmetric deformation and stability of a viscous drop in a steady electric field. *J. Fluid Mech.*, 590:239–264, 2007.

[78] D. Lacoste, G. I. Menon, M. Z. Bazant, and J. F. Joanny. Electrostatic and electrokinetic contributions to the alastic moduli of a driven membrane. *Eur. Phys. J. E*, 28:243–264, 2009.

[79] M.-C. Lai, C.-Y. Huang, and Y.-M. Huang. Simulating the axisymmetric interfacial flows with insoluble surfactant by immersed boundary method. *Int. J. Num. Anal. Modeling*, 8:105–117, 2011.

[80] A. T. Layton and J. T. Beale. A partially implicit hybrid method for computing interface motion in Stokes flow. *Disc. Cont. Dyn. Sys. B*, 17:1139–1153, 2012.

[81] J.-F. Lemieux, B. Tremblay, S. Thomas, J. Sedlácek, and L. A. Mysak. Using the preconditioned Generalized Minimum RESidual (GMRES) method to solve the sea-ice momentum equation. *J. Geophys. Res.*, 113, 2008.

[82] R. J. Leveque and Z. Li. The immersed interface method for elliptic equations with discontinuous coefficients and singular sources. *SIAM J. Numer. Anal.*, 31:1019–1044, 1994.

[83] R. J. Leveque and Z. Li. Immersed interface methods for Stokes flow with elastic boundaries or surface tension. *SIAM J. Sci. Comput.*, 18:709–735, 1997.

[84] J. Li and H. Lin. Numerical simulation of molecular uptake via electroporation. *Bioelectrochemistry*, 82:10–21, 2011.

[85] Y. Li. *Numerical methods for simulating fluid motion driven by immersed interfaces.* PhD thesis, Duke University, 2012.

[86] Y. Li, I Sgouralis, and A. T. Layton. Computing viscous flow in an elastic tube. To appear in *Numer. Math. Theor. Meth. Appl.*

[87] Z. Li. Fast iterative algorithm for elliptic interface problems. *SIAM J. Numer. Anal.*, 35:230–254, 1998.

[88] Z. Li and K. Ito. Maximum principle preserving schemes for interface problems with discontinuous coefficients. *SIAM J. Sci. Comput.*, 23:339–361, 2001.

[89] Z. Li and K. Ito. *The immersed interface method: Numerical solutions of PDEs involving interfaces and irregular domains*. SIAM, 2006.

[90] H. Lin, B. D. Storey, M. H. Oddy, C.-H. Chen, and J. G. Santiago. Instability of electrokinetic micro channel flows with conductivity gradients. *Phys. Fluids*, 16:1922, 2004.

[91] Y. Lin, P. Skjetne, and A. Carlson. A phase field model for multiphase electro-hydrodynamics flow. *J. Multiphase Flow*, 45:1–11, 2012.

[92] J. M. López-Herrera, S. Popinet, and M. A. Herrada. A charge-conservative approach for simulating electrohydrodynamic two-phase flows using volume-of-fluid. *Comput. Phys.*, 230:1939–1955, 2011.

[93] P. Marmottant, T. Biben, and S. Hilgenfeldt. Deformation and rupture of lipid vesicles in the strong shear flow generated by ultrasound-driven micro bubbles. *Proc. R. Soc. A*, 464:1781–1800, 2008.

[94] P. Marszalek, D.-S. Liu, and T. Y. Tsong. Schwan equaltion and transmembrane potential induced by alternating electric field. *Biophys. J.*, 58:1053–1058, 1990.

[95] K. Maswiwat, D. Wachner, and J. Gimsa. Effects of cell orientation and electric field frequency on the transmembrane potential induced in ellipsoidal cells. *Bioelectrochemistry*, 74:130–141, 2008.

[96] K. Maswiwat, D. Wachner, R. Warnke, and J. Gimsa. Simplified equations for the transmembrane potential induced in ellipsoidal cells of rotational symmetry. *J. Phys. D: Appl. Phys.*, 40:914–923, 2007.

[97] A. Mayo. The fast solution of Poisson's and the biharmonic equations on irregular regions. *SIAM J. Numer. Anal.*, 21:285–299, 1984.

[98] A. A. Mayo and C. S. Peskin. An implicit numerical method for fluid dynamics problems with immersed elastic boundaries. *Contemp. Math.*, 141:261, 1993.

[99] L. C. McConnell, M. J. Miksis, and P. M. Vlahovska. Vesicle electrohydrodynamics in DC electric fields. *IMA J. Appl. Math.*, pages 1–21, 2013.

[100] J. R. Melcher and M. S. Firebaugh. Traveling wave bulk electroconvection induced across a temperature gradient. *Phys. Fluids*, 10:1178, 1967.

[101] J. R. Melcher and G. I. Taylor. Electrohydrodynamics: A review of the role of interfacial shear stresses. *Annu. Rev. Fluid Mech.*, 1:111–146, 1969.

[102] M. Miksis. Shape of a drop in an electric field. *Phys. Fluids*, 24:1967, 1981.

[103] W. J. Milliken, H. A. Stone, and L. G. Leal. The effect of surfactant on the transient motion of Newtonian drops. *Phys. Fluids*, 5 (1):69–79, 1993.

[104] M. D. Mitov, P. Méléard, M. Winterhalter, M. I. Angelova, and P. Bothorel. Electric-field-dependent thermal fluctuations of giant vesicles. *Phys. Rev. E*, 48:628–631, 1993.

[105] H. Morgan and N. G. Green. Dielectrophoretic manipulation of rod-shaped viral particles. *J. Electrostatics*, 42:279–293, 1997.

[106] J. C. Neu and W. Krassowska. Asymptotic model of electroporation. *Phys. Rev. E*, 59:3471–3482, 1999.

[107] E. Neumann, A. E. Sowers, and C. A. Jordan. *Electroporation and electrofusion in cell biology*. Springer, 1989.

[108] E. P. Newren, A. L. Fogelson, R. D. Guy, and R. M. Kirby. Unconditionally stable discretizations of the immersed boundary equations. *J. Comput. Phys.*, 222:702–719, 2007.

[109] H. Nganguia, Y.-N. Young, P. M. Vlahovska, J. Bławzdziewcz, J. Zhang, and H. Lin. Equilibrium electro-deformation of a surfactant-laden viscous drop. *Phys. Fluids*, 25:092106, 2013.

[110] P. K. Notz, A. U. Chen, and O. A. Basaran. Satellite drops: unexpected dynamics and change of scaling during pinch-off. *Phys. Fluids*, 13:549–552, 2001.

[111] M. Ohno, T. Hamada, K. Takiguchi, and M. Homma. Dynamic behavior of giant liposomes at desired osmotic pressures. *Langmuir*, 25(19):11680–11685, September 2009.

[112] H. Paknemat, A. R. Pishevar, and P. Pournaderi. Numerical simulation of drop deformations and breakup modes caused by direct current electric fields. *Phys. Fluids*, 24:102101, 2012.

[113] Y. Pawar and K. J. Stebe. Marangoni effects on drop deformation in an extensional flow: The role of surfactant physical chemistry. I Insoluble surfactants. *Phys. Fluids*, 8 (7):1738–1751, 1996.

[114] C. S. Peskin. Numerical analysis of blood flow in the heart. *J. Comput. Phys.*, 25:220–252, 1977.

[115] C. S. Peskin and D. M. McQueen. Modeling prosthetic heart valves for numerical analysis of blood flow in the heart. *J. Comput. Phys.*, 37:113–132, 1980.

[116] P. Peterlin. Frequency-dependent electrodeformation of giant phospholipid vesicles in ac electric field. *J. Biol. Phys.*, 36:339–354, 2010.

[117] P. Peterlin, S. Svetina, and B. Zeks. The prolate-to-oblate shape transition of phospholipid vesicles in response to frequency variation of an ac electric field can be explained by the dielectric anisotropy of a phospholipid bilayer. *J. Phys. Condens. Matter*, 19:136220, 2007.

[118] G. Popescu, T. Ikeda, K. Goda, C. A. Best-Popescu, M. Laposata, S. Manley, R. R. Dasari, K. Badizadegan, and M. S. Feld. Optical measurement of cell membrane tension. *Phys. Rev. Lett.*, 97:218101, 2006.

[119] B. P. Van Poppel, O. Desjardins, and J. W. Daily. A ghost fluid, level set methodology for simulating multiphase electrohydrodynamic flows with application to liquid fuel injection. *J. Comput. Phys.*, 229:7977–7996, 2010.

[120] T. Portet, C. Mauroy, V. Démery, T. Houles, J.-M. Escoffre, D. S. Dean, and M.-P. Rols. Destabilizing giant vesicles with electric fields: An overview of current applications. *J. Membrane Biol.*, 245:555–564, 2012.

[121] A. Ramos, editor. *Electrokinetics and electrohydrodynamics in microsystems*, volume 530 of *CISM International Center for Mechanical Sciences*. Springer, 2011.

[122] W. Rawicz, K. C. Olbrich, T. McIntosh, D. Needham, and E. Evans. Effect of chain length and unsaturation on elasticity of lipid bilayers. *Biophys. J.*, 79:328–339, 2000.

[123] K. A. Riske and R. Dimova. Electro-deformation and poration of giant vesicles viewed with high temporal resolution. *Biophys. J.*, 88:1143–1155, 2005.

[124] K. A. Riske and R. Dimova. Electric pulses induce cylindrical deformations on giant vesicles in salt solutions. *Biophys. J.*, 91:1778–1786, 2006.

[125] Y. Saad. A flexible inner-outer preconditioned GMRES algorithm. *SIAM J. Sci. Comput.*, 14:461–469, 1993.

[126] Y. Saad and M. H. Schultz. GMRES: A generalized minimal residual algorithm for solving nonsymmetric linear systems. *SIAM J. Sci. Stat. Comput.*, 7:856–869, 1986.

[127] M. M. Sadik, J. Li, J. W. Shan, D. I. Shreiber, and H. Lin. Vesicle deformation and poration under strong dc electric fields. *Phys. Rev. E*, 83:066316, 2011.

[128] M. M. Sadik, J. Li, J. W. Shan, D. I. Shreiber, and H. Lin. Vesicle deformation and poration under strong dc electric fields. *Phys. Rev. E*, 83:066316, 2011.

[129] Y. Sakuma, T. Taniguchi, and M. Imai. Pore formation in a binary giant vesicle induced by cone-shaped lipids. *Biophys. J.*, 99(2):472–479, July 2010.

[130] P. F. Salipante, R. Knorr, R. Dimova, and P. M. Vlahovska. Electrodeformation method for measuring the capacitance of bilayer membranes. *Soft Matter*, 8:3810–3816, 2012.

[131] O. Sandre, L. Moreaux, and F. Brochard-Wyart. Dynamics of transient pores in stretched vesicles. *Proc. Nat. Acad. Sci. USA*, 96:10591–10596, September 1999.

[132] D. A. Saville. Electrohydrodynamics: The Taylor-Melcher leaky dielectric model. *Annu. Rev. Fluid Mech.*, 29:27–64, 1997.

[133] J. Schwalbe, P. M. Vlahovska, and M. Miksis. Vesicle electrohydrodynamics. *Phys. Rev. E*, 83:046309, 2011.

[134] J. T. Schwalbe. *Dynamics and stability of lipid bilayer membranes in viscous flow and electric fields*. PhD thesis, Northwestern University, 2010.

[135] J. Seiwert and P. M. Vlahovska. Instability of a fluctuating membrane driven by an ac electric field. *Phys. Rev. E*, 87:022713, 2013.

[136] R. M. Servuss, V. Harbich, and W. Helfrich. Measurements of the curvature-elastic modulus of egg lecithin bilayers. *Biochem. Biophys. Acta*, 436:900–903, 1976.

[137] J. D. Sherwood. Breakup of fluid droplets in electric and magnetic fields. *J. Fluid Mech.*, 188:133–146, 1998.

[138] K. C. Smith, J. C. Neu, and W. Krassowska. Model of creation and evolution of stable electrophorus for DNA delivery. *Biophys. J.*, 86:2813–2826, 2004.

[139] J. M. Stockie and B. R. Wetton. Analysis of stiffness in the immersed boundary method and implications for time-stepping schemes. *J. Comput. Phys.*, 154:41–64, 1999.

[140] H. A. Stone and L. G. Leal. The effects of surfactants on drop deformation and breakup. *J. Fluid Mech.*, 220:161–186, 1990.

[141] W. Sung and P. J. Park. Dynamics of pore growth in membranes and membrane stability. *Biophys. J.*, 73:1797–1804, 1997.

[142] G. Supeene, C. R. Koch, and S. Bhattacharjee. Deformation of a droplet in an electric field: Nonlinear transient response in perfect and leaky dielectric mdeia. *J. Colloid Int. Sci.*, 318:463–376, 2008.

[143] R. Suryo, P. Doshi, and O. A. Basaran. *Phys. Fluids*, 16:4177, 2004.

[144] S. Takagi and Y. Matsumoto. Surfactant effects on bubble motion and bubbly flows. *Ann. Rev. Fluid Mech.*, 43:615–636, 2011.

[145] C. Taupin, M. Dvolaitzky, and C. Sauterey. Osmotic pressures induced pores in phospholipid vesicles. *Biochemistry*, 14(21):4771–4775, 1975.

[146] G. I. Taylor. Conical free surfaces and fluid interfaces. In *Proc. 11th Intl. Cong. App. Mech. Munich (Germany) 1964*, pages 790–796. 1964.

[147] Geoffrey Taylor. Studies in electrohydrodynamics. I. The circulation produced in a drop by electric field. *Proc. R. Soc. Lond. A*, 291:159–166, 1966.

[148] K. E. Teigen and S. T. Munkejord. Influence of surfactant on drop deformation in an electric field. *Phys. Fluids*, 22:112104, 2010.

[149] J. Teissié, J. M. Escoffre, M. P. Rols, and M. Golzio. Time dependence of electric field effects on cell membranes. a review for a critical selection of pulse duration for therapeutical applications. *Radiol. Oncol.*, 42:196–206, 2008.

[150] I. Turcu and C. M. Lucaciu. Dielectrophoresis: a spherical shell model. *J. Phys. A: Math. Gen.*, 22:985–993, 1989.

[151] S. O. Unverdi and G. Tryggvason. A front-tracking method for viscous, incompressible, multi-fluid flows. *J. Comput. Phys.*, 100:25–37, 1992.

[152] S. Veerapaneni, D. Gueyffier, G. Biros, and D. Zorin. A numerical method for simulating the dynamics of 3D axisymmetric vesicles suspended in viscous flows. *J. Comput. Phys.*, 228:7233–7249, 2009.

[153] S. Veerapaneni, D. Gueyffier, D. Zorin, and G. Biros. A boundary integral method for simulating the dynamics of inextensible vesicles suspended in a viscous fluid in 2D. *J. Comput. Phys.*, 228:2334–2353, 2009.

[154] O. Vizika and D. A. Saville. The electrohydrodynamic deformation of drops suspended in liquids in steady and oscillatory electric fields. *J. Fluid Mech.*, 239:1–21, 1992.

[155] P. M. Vlahovska. On the rheology of a dilute emulsion in a uniform electric field. *J. Fluid Mech.*, 670:481–503, 2010.

[156] P. M. Vlahovska, J. Blawzdziewicz, and M. Loewenberg. Small-deformation theory for a surfactant-covered drop in linear flows. *J. Fluid Mech.*, 624:293–337, 2009.

[157] P. M. Vlahovska, R. S. Graciá, S. Aranda-Espinoza, and R. Dimova. Electrohydrodynamic model of vesicle deformation in alternating electric fields. *Biophys. J.*, 96:4789, 2009.

[158] C. Wang, J. Wang, Q. Cai, Z. Li, H.-K. Zhao, and R. Luo. Exploring accurate Poisson-Boltzman methods for biomolecular simulations. *Comput. Theor. Chem.*, 1024:34–44, 2013.

[159] X. Wang, X.-B. Wang, and P. R. C. Gascoyne. General expressions for dielectrophoretic force and electrorotational torque derived using the maxwell stress tensor method. *J. Electrostatics*, 39:277, 1997.

[160] M. Washizu, O. Kurosawa, I. Arai, S. Suzuki, and N. Shimamoto. Applications of electrostatic stretch-and-positioning of DNA. *IEEE Trans. Ind. Appl.*, 31:447–456, 1995.

[161] M. Washizu, Y. Nikaido, O. Kurosawa, and H. Kabata. Stretching yeast chromosomes using electroosmotic flow. *J. Electrostatics*, 57:395–405, 2003.

[162] E. D. Wilkes, S. D. Phillips, and O. A. Basaran. Computational and experimental analysis of dynamics of drop formation. *Phys. Fluids*, 11:3577–3598, 1999.

[163] M. Winterhalter and W. Helfrich. Deformation of spherical vesicles by electric fields. *J. Coll. Int. Sci.*, 122:583–586, 1988.

[164] T. Yamamoto, S. Aranda-Espinoza, R. Dimova, and R. Lipowsky. Stability of spherical vesicles in electric fields. *Langmuir*, 26:12390–12407, 2010.

[165] Q. Yang, B. Q. Li, and Y. Ding. 3D phase field modeling of electrohydrodynamic multiphase flows. *Inter. J. Multiphase Flow*, 57:1–9, 2013.

[166] M. Yazdani and J. Seyed-Yagoobi. Heat transfer augmentation of parallel flows by means of electric conduction phenomenon in macro- and microscales. *J. Heat Trans.*, 132:062402, 2010.

[167] J. D. Zahn and V. Reddy. Two phase micromixing and analysis using electrohydrodynamic instabilities. *Microfluid Nanofluid*, 2:399–415, 2006.

[168] J. Zhang and D. Y. Kwok. A 2D lattice Boltzmann study on electrohydrodynamic drop deformation with the leaky dielectric theory. *J. Comput. Phys.*, 206:150–161, 2005.

[169] J. Zhang, J. Zahn, and H. Lin. Transient solution for droplet deformation under electric fields. *Phys. Rev. E*, 87:043008, 2013.

[170] J. Zhang, J. D. Zahn, W. Tan, and H. Lin. A transient solution for vesicle electrodeformation and relaxation. *Phys. Fluids*, 25:071903, 2013.

[171] E. K. Zholkovskij, J. H. Masliyah, and J. Czarnecki. An electrokinetic model of drop deformation in an electric field. *J. Fluid Mech.*, 472:1–27, 2002.

[172] C. Zhou, P. Yue, and J. J. Feng. Formation of simple and compound drops in microfluidic devices. *Phys. Fluids*, 18:092105, 2006.

[173] U. Zimmermann, U. Friedrich, H. Mussauer, P. Gessner, K. Hamel, and V. Sukhoruhov. Electromanipulation of mammalian cells: fundamentals and application. *IEEE Trans. Plasma Sci.*, 28:72–82, 2000.

[174] U. Zimmermann and G. A. Neil. *Electromanipulation of cells.* CRC Press, Boca Raton, FL, 1996.